Nanoelectrochemistry at Liquid/liquid Interfaces and Biomembranes

By

Francois Laforge

A dissertation submitted to the Graduate Faculty of Chemistry in partial fulfillment of the requirements for the degree of Doctor of Philosophy, The City University of New York

2008

UMI Number: 3296956

UMI Microform 3296956

ProQuest Information and Learning Company
300 North Zeeb Road
P.O. Box 1346
Ann Arbor, MI 48106-1346

This manuscript has been read and accepted for the
Graduate Faculty in Chemistry in satisfaction of the
dissertation requirement for the degree of Doctor of Philosophy.

Michael V. Mirkin

_____ _____
Date Chair of Examining Committee

Gerald W. Koeppl

_____ _____
Date Executive Officer

Ronald L. Birke_____

Susan A. Rotenberg_____

Supervisory Committee

THE CITY UNIVERSITY OF NEW YORK

Abstract

Nanoelectrochemistry at Liquid/liquid interfaces and biomembranes

By

Francois Laforge

Adviser: Prof Michael V. Mirkin

The electrical and chemical properties of liquid/liquid interfaces (e.g. water/oil) and biomembranes control the behavior of a variety of biological and technical systems. Electrochemistry is a powerful technique for the study of charge transfer at the liquid/liquid interface. Several experimental problems are inherent to large liquid/liquid interfaces (e.g., resistive drop, charging current). Reducing the size of the liquid/liquid interface has been one way to overcome these limitations. In the present work Micropipette and SECM techniques were used to investigate various liquid/liquid micro- to nanointerfaces and biomembranes.

Electron transfer at the water/ionic liquid interface has been studied for the first time using the scanning electrochemical microscope. The heterogeneous rate constant of electron transfer between aqueous ferricyanide and ionic liquid-dissolved ferrocene was found to be k_f = 0.33 cm/M/s. The partition coefficient of redox species between ionic liquid and water can be determined from short-range SECM current-distance curves under quasi-steady-state conditions.

Our investigations on the electrically driven ion transfer between water to neat organic solvent using nanopipettes showed that there are essentially two types of ion transfer behaviors: the transfer of hydrophobic ions which is a one-step process, and the

transfers of hydrophilic ions which must be facilitated by hydrophobic organic counterions. Also by studying the role of water dissolved in the organic phase, we conclude that strongly hydrophilic ions are transferred from the aqueous phase to water clusters dispersed in the organic phase.

A new device useful for living cell microinjection and more has been developed and tested. The device, called electrochemical attosyringe, can be used to inject precise doses of liquids- from attoliters to nanoliters.

Nanoelectrodes are capable of probing regions of space with volumes several microns-cube. This quality renders them useful for spacially resolved studies of intracellular redox reactions. Nanoelectrodes were prepared, characterized and used to probe redox reaction inside living cells, to study molecular transport across the membrane and to image cells.

Acknowledgements

I am grateful to my mentor, Prof. Michael Mirkin, for his guidance and care. Michael has been extremely supportive and has constantly encouraged me to challenge myself during the past five years. With his financial support I have been able to focus all my attention on my research work.

I would like to thank Prof. Susan Rotenberg, Prof. Ronald Birke and Prof. Gerald Koeppl for their guidance and interest in my education.

The assistance in electronics and computer programming from my coworker and friend, James Carpino, not only helped me solve technical problems and build useful devices for my research but it has also been an immense source of learning. James' confidence and assertiveness are exemplary.

I would like to express my thanks to Dr. Peng Sun whose work and dedication for his research are uncommon.

The financial support from the City University of New York and the Electrochemical Society is deeply appreciated.

Finally I would like to express my gratitude to Prof. Rose Kfar Rose for her generosity.

Table of content

List of Tables

List of Charts

Chapter I

Liquid/Liquid Interfaces, SECM and Nanopipettes

1.1 Introduction

Electron transfer (ET) and simple and facilitated ion transfer (IT) reactions at the interface between two immiscible electrolyte solutions (ITIES) are processes occurring in nature (e.g., photosynthesis, metabolism) and useful for industrial applications such as heterogeneous liquid/liquid catalysis or solvent extraction. These charge transfer (CT) reactions are amenable to experimental studies because they can be initiated and/or controlled by applying a voltage to the two phases of an ITIES. Therefore electrochemical techniques such as voltammetry and galvanometry are well suited for uncovering the nature and mechanisms of CT at the ITIES.

1.2 Structure of the Electrified Liquid/liquid Interface (ITIES)

The structure of the electrified metal/liquid interface was first modeled by Gouy and Chapman [1,2] in 1910. Later Verwey and Niessen [3] applied the Gouy-Chapman model to the ITIES. In their simple model two ionic diffuse layers are separated by a sharp planar interface. The assumptions in the Gouy-Chapman theory (e.g., ions are considered inert point charges and solvent is a continuum) are too coarse to give an acceptable model of the ITIES. The real size of ions (especially bulky organic ions) must be taken into consideration if one wants to have a better account of the ITIES structure. Verwey and Niessen's simple model was subsequently improved by Gavach *et al.* [4,5] According to the modified Verwey-Niessen (MVN) model the interface is not infinitely sharp but made of an ion-free inner layer where solvent molecules are oriented. This

inner layer is delimited by two outer Helmholtz planes (OHP), one in the aqueous phase the other in the organic phase (Fig. 1.1).

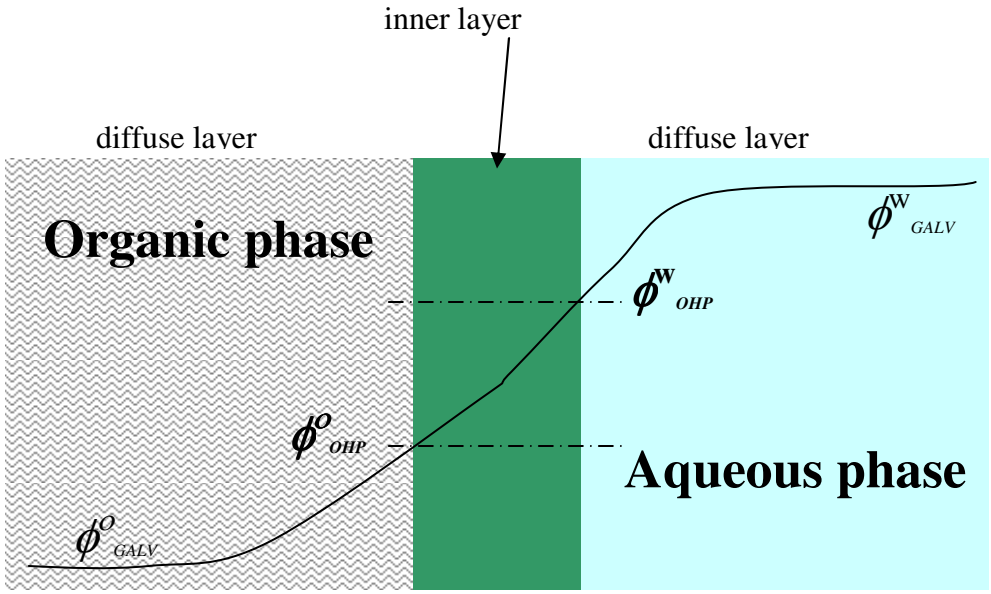

Figure 1.1. Scheme of the interfacial structure of the electrified liquid/liquid interface according to the modified Verwey-Niessen (MVN) model.

Each OHP defines the distance of closest approach to the interface for the ions. The distribution of the potential drop across the interface when the later is electrified can be separated into three major contributions:

$$\Delta^{o}_{w}\Phi = \Phi^{w}_{GALV} - \Phi^{o}_{GALV} = \Delta^{o}\Phi_{DL} + \Delta\Phi_{OHP} + \Delta^{w}\Phi_{DL} \qquad (1.1)$$

where $\Delta^{o}\Phi_{DL} = \Phi^{o}_{OHP} - \Phi^{o}_{GALV}$ is the potential difference between the bulk organic phase and the potential right at the OHP of the organic phase (i.e., the potential drop across the organic diffuse layer) and $\Delta^{w}\Phi_{DL} = \Phi^{w}_{GALV} - \Phi^{w}_{OHP}$ is the potential difference between the aqueous OHP and bulk water (i.e., the potential drop across the aqueous diffuse layer). $\Delta^{o}_{w}\Phi_{OHP}$ is the potential drop across the inner layer.

There are two major problems with the MVN model. (1) the model does not take into account the possibility of ion pairing and/or adsorptions at the interface. These effects explain the origin of enhanced capacitances of some ITIES [6,7]. (2) the inner layer in the MVN model is rigid and static. This picture contradicts the results of numerous molecular dynamics and Monte Carlo simulations [8] in which the interface is subject to spatial fluctuations. This discrepancy in the MVN model was experimentally confirmed by Girault and Schiffrin in the 80s [9].

Girault and Schiffrin performed a series of studies involving the measurement of the surface excess of water at the oil/water interface [9,10]. They showed that, in the case of polar solvents (e.g., 1,2-dichloroethane or nitrobenzene), the surface excess of water was equivalent to less than one monolayer. On the basis of these observations they concluded that the interface is a mixed solvent layer of thickness no more than two to three molecular diameters (Fig. 1.2).

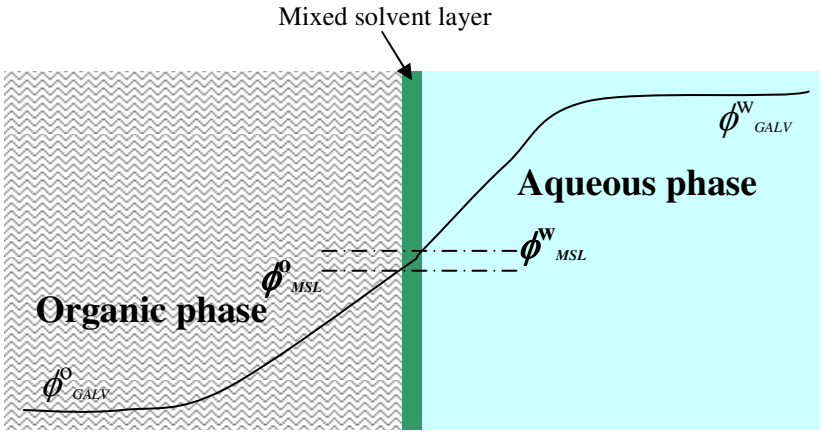

Figure 1.2. Scheme of the electrified water/organic interface according to the mixed solvent layer model. The interfacial potential drop $\Delta^{o}_{w}\Phi_{MSL}$ is negligible compared to the galvanic potential difference $\Delta^{w}_{o}\Phi$.

The distributions of ions far from the interface are similar to that predicted by the Gouy-Chapman theory but hydrophobic as well as hydrophilic ions can penetrate the mixed solvent layer and form ion pairs and other coupled species [11]. The potential

distribution across the interface is smooth and only a small potential drop ($\Delta^{o}_{w}\Phi_{MSL}$) exists across the mixed solvent layer (see Fig. 1.2).

Computer simulations of the water/organic solvent interface [12-16] generally give a picture of the interface where the boundary between the two solvents is molecularly sharp but subject to fluctuations. These fluctuations also called capillary waves render the interface apparently wider (~ 1nm). An interesting feature of these surface fluctuations is that they give rise to what Benjamin has called "fingers" or "cones", which are major protrusions of one liquid into the other. These fingers are the basis to a model of IT mechanism (see Ion transfer kinetics § 1.3.2).

1.3 Electron Transfer and Ion Transfer at the ITIES

1.3.1 Nernst Equation for an Ion Transfer at the ITIES

The electrochemical potential $\tilde{\mu}^{\alpha}_{i}$ of a charged species (i) in phase (α) is given by the following equation:

$$\tilde{\mu}^{\alpha}_{i} = \mu^{0,\alpha}_{i} + RT\, ln a^{\alpha}_{i} + z_i F \phi^{\alpha} \qquad (1.2)$$

where $\mu^{0,\alpha}_{i}$ is the standard chemical potential, a^{α}_{i} is the activity of the ion in phase α, z_i is the charge of the ion, R, T and F are the gas constant, the temperature and the faraday constant respectively, and ϕ^{α} is the bulk electrical potential (Galvani potential) of phase α.

If two different immiscible liquids are in contact, each ionic species will partition between the two phases (water: w and organic: o) by transferring across the interface (Fig. 1.3).

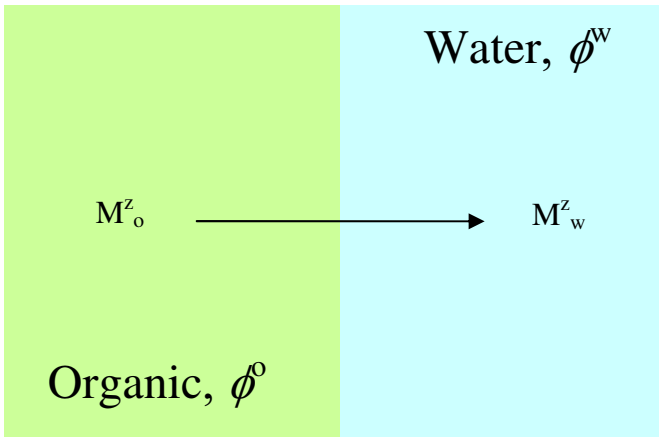

Figure 1.3. transfer of M^z ion from the organic to the aqueous phases. The ionic charge is transferred from the organic phase at potential Φ^o to the aqueous phase at potential Φ^w.

Equilibrium will be reached when the electrochemical potential of each ionic species are equal in both phases:

$$\tilde{\mu}^w_i = \tilde{\mu}^o_i \tag{1.3}$$

hence the Galvani potential difference will be expressed by the formula:

$$\Delta^o_w\Phi = \Phi^w - \Phi^o = (\mu^{0,w}_i - \mu^{0,o}_i) / (z_iF) + (RT/z_iF)\, ln(a^w_i / a^o_i) \tag{1.4}$$

The difference of standard chemical potentials $(\mu^{0,w}_i - \mu^{0,o}_i)$ is equal to the standard Gibbs energy of transfer $(\Delta G^{0,o\rightarrow w}_{tr,i})$ defined as the difference between the standard Gibbs energy of solvation of the ion in each phase:

$$\Delta G^{0,o\rightarrow w}_{tr,i} = \Delta G^{0,w}_{solv,i} - \Delta G^{0,o}_{solv,i} = \mu^{0,w}_i - \mu^{0,o}_i \tag{1.5}$$

Defining the standard ion transfer potential by:

$$\Delta^{o}_{w}\Phi^{0}_{i} = \Delta G^{0,o\rightarrow w}_{tr,i} / (z_i F) \quad (1.6)$$

one can express relation (1.4) in the form of the Nernst equation:

$$\Delta^{o}_{w}\Phi = \Delta^{o}_{w}\Phi^{0}_{i} + (RT/z_i F)\, ln(a^{w}_{i} / a^{o}_{i}) \quad (1.7)$$

The Nernst equation governs the ions distribution at equilibrium between two electrified liquid phases.

1.3.2 Nernst Equation for an Interfacial Electron Transfer

At the liquid/liquid interface electrons can only transfer from one chemical species located in one phase to a chemical species located in the other phase (Fig. 1.4). The ET is symbolized by reaction (1.8):

$$O_1^{w} + R_2^{o} = R_1^{w} + O_2^{o} \quad (1.8)$$

The Gibbs energy for reaction (1.8), when the later is electrically driven, can be expressed using the electrochemical potentials of all the species:

$$\Delta G^{o\rightarrow w}_{tr,e-} = \tilde{\mu}^{w}_{R1} + \tilde{\mu}^{o}_{O2} - \tilde{\mu}^{w}_{O1} - \tilde{\mu}^{o}_{R2} \quad (1.9)$$

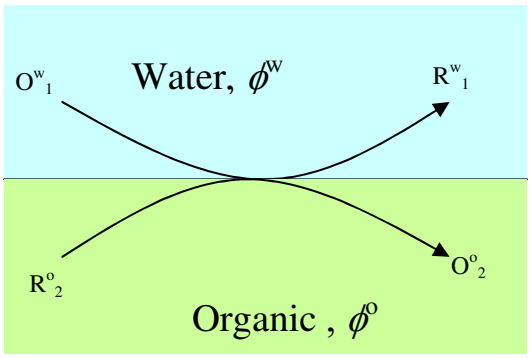

Figure 1. 4. Electron transfer at the interface. The electronic charge is transferred from the organic phase at potential Φ^{o} to the aqueous phase at potential Φ^{w}.

When the reaction is at equilibrium $\Delta G^{o\rightarrow w}_{tr,e-} = 0$. Using Eq. (1.2) to express the electrochemical potentials of all chemical species, the following equation can be derived:

$$0 = \mu^{0,w}_{R1} + \mu^{0,o}_{O2} - \mu^{0,w}_{O1} - \mu^{0,o}_{R2} - \Delta z_1 F\Phi^{w} + \Delta z_2 F\Phi^{o} + RTln(a^{w}_{R1}\, a^{o}_{O2} / a^{w}_{O1} a^{o}_{R2}) \quad (1.10)$$

where Δz_1 and Δz_2 are the charge differences between the oxidized species and reduced species in each phase. Δz_1 and Δz_2 correspond to the same number n of electrons transferred during reaction (1.8) (Δz_1 and Δz_2 would still equal to n if stoichiometric coefficients other than one where chosen in reaction (1.8)). Eq. (1.10) can be rewritten to express the Galvani potential difference:

$$\Delta^{o}_{w}\Phi = \Phi^{w} - \Phi^{o} = (\mu^{0,w}_{R1} + \mu^{0,o}_{O2} - \mu^{0,w}_{O1} - \mu^{0,o}_{R2})/nF + (RT/nF)ln(a^{w}_{R1}\, a^{o}_{O2} / a^{w}_{O1} a^{o}_{R2}) \quad (1.11)$$

The standard Gibbs energy of reaction (i.e., standard conditions and $\Delta^{o}_{w}\Phi = 0$) is defined by:

$$\Delta G^{0} = \mu^{0,w}_{R1} - \mu^{0,o}_{O2} + \mu^{0,w}_{O1} - \mu^{0,o}_{R2} \quad (1.12)$$

and can be expressed in terms of standard redox potentials of O_1/R_1 couple in the aqueous phase and O_2/R_2 couple in the organic phase respectively when both are measured versus the same reference electrode [17,18]:

$$\Delta G^{0} = nF(E^{0,o}{}_{O2/R2} - E^{0,w}{}_{O1/R1}) \tag{1.13}$$

Finally the Nernst equation for the electron transfer across a liquid/liquid interface takes the following form:

$$\Delta^{o}{}_{w}\Phi = (E^{0,o}{}_{O2/R2} - E^{0,w}{}_{O1/R1}) + (RT/nF)ln(a^{w}{}_{R1}\, a^{o}{}_{O2} / a^{w}{}_{O1} a^{o}{}_{R2}) \tag{1.14}$$

This equation governs the equilibrium concentrations of chemical species involved in an interfacial ET.

1.3.3 Kinetics of Electron Transfer

To evaluate the rate of ET at the ITIES Marcus [19] used a formalism similar to the one used for homogeneous ET process. Reaction (1.8) can be described using elementary steps:

$$O_1{}^{w} + R_2{}^{o} = O_1{}^{w}|R_2{}^{o} \qquad \text{Precursor complex formation} \tag{1.15a}$$

$$O_1{}^{w}|R_2{}^{o} = (O_1{}^{w}|R_2{}^{o})^{*} \qquad \text{Precursor reorganization} \tag{1.15b}$$

$$(O_1{}^{w}|R_2{}^{o})^{*} = (R_1{}^{w}|O_2{}^{o})^{*} \qquad \text{Electron transfer} \tag{1.15c}$$

$$(R_1{}^{w}|O_2{}^{o})^{*} = R_1{}^{w}|O_2{}^{o} \qquad \text{Successor reorganization} \tag{1.15d}$$

$$R_1{}^w|O_2{}^o = R_1{}^w + O_2{}^o \qquad \text{Successor dissociation} \qquad (1.15d)$$

In the first equation the symbol "|" represents the "plane of reaction" whose definition depends on the model of the liquid/liquid interface used. If we denote λ as the reorganization energy associated with the electron transfer (i.e., solvation shell reorganization and reactant-product conformational changes), w_r and w_p the work terms associated with precursor association and successor dissociation and ΔG^0 the standard free energy of reaction (1.8) then the free energy barrier can be expressed by the following formula:

$$\Delta G^{\ddagger} = w_r + (\lambda + \Delta G^0 + w_p - w_r)^2/4\lambda \qquad (1.16)$$

The reaction rate constant, k_{obs}, is given by the following formula:

$$k_{obs} = 2\pi(a_1 + a_2)(\Delta R)^3 \, \kappa\nu \exp(-\Delta G^{\ddagger}/RT) \qquad (1.17)$$

in which a_1 and a_2 are the molecular radii of the reactants in the aqueous and organic phase respectively, ΔR is the distance at which electron tunneling probability becomes appreciable, κ is the transmission coefficient and ν is the effective electron hopping frequency.

Chapter II reports our investigation of ET at a new type of liquid/liquid interface, namely Ionic-Liquid/water interface. It is shown that ET follows a classic Butler-Volmer relationship and that higher value of the ET rate constant at IL/water interface compared to 1,2-dichloroethane/water interface were obtained, a result that is difficult to reconcile with existing ET theory.

1.3.4 Kinetics of Ion Transfer

IT at the liquid/liquid interface can be induced by applying a potential difference between the two liquids. Electrochemists distinguish between two classes of IT: assisted and non-assisted ITs. For the non-assisted transfer the ion is merely forced into the opposite phase by the potential difference applied to the system. In the case of assisted IT, a molecule soluble in the organic phase (e.g., dibenzo-18-crown-6-ether, valinomycin, etc.) diffuses toward the interface and forms a complex with a hydrophilic ion located in the aqueous phase. The chelation transforms the hydrophilic ion into a hydrophobic one thus facilitating its subsequent dissolution into the organic phase. Overall the chelating agent reduces the energy barrier for the dissolution of the ion in the organic solvent.

There have been several theories developed for the kinetics of ion transfer at the liquid/liquid interface. Whereas ET is an activated process (i.e., the reaction mechanism involves an activated complex whose energy is above the products and reactants) there is no clear experimental evidence that the IT mechanism at the ITIES involves an energy barrier. Kakiuchi [20] derived a theory in which the rate of ion transport across the interface is reduced by the enhanced viscosity of the inner layer (i.e., the region of thickness Δx across the interface). In his model the diffusion coefficient D_i of the ion inside the inner layer is smaller than both bulk values. Kakiuchi showed that the current-voltage curves were not following a Tafel relationship properly speaking but that still, values of the transfer coefficient, $\alpha = 0.5$ and of the standard rate constant, $k_o = D_i/\Delta x$ could be given physical meanings.

Schmickler [21] used a lattice-gas model to calculate the rate of IT. In the lattice-gas picture the solvent molecules occupy the sites of an infinite, three-dimensional lattice. To create a liquid/liquid interface, molecules of organic solvent and molecules of water are given complementary probabilities of residing at a lattice site. The probability function depends only on the z coordinate (i.e., the interface lies in the x,y plane), follows a sigmoid profile, and its value is 0.5 at the center of the interface. An ion is inserted in

the lattice and calculations are done to extract the potential of mean force (pmf) for the ion as a function of z. The pmf depends on the standard Gibbs energies of transfer of the ion, $\Delta G^{0,o\rightarrow w}{}_{tr,i}$ and on the galvanic potential difference of the two phases, $\Delta^{o}{}_{w}\Phi$. Its profile is described in Fig. (1.5).

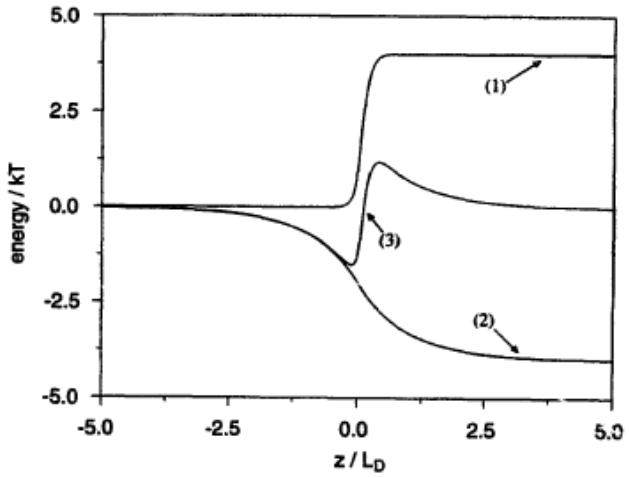

Figure 1.5. The potential of mean force at equilibrium. (1) chemical term; (2) electrostatic term; (3) total potential.

Fig. (1.5) shows that the ion needs to overcome an energy barrier (curve 3) in order to transfer form one phase to the other. Hence the transition state theory, which implies an activated process, can be used in conjunction with this model. According to the transition state theory the rate constant of ion transfer, k_f can be derived from the pmf. Its value is given by $k_f = (kT/2\pi m)^{1/2}\exp(-u_{max}/kT)$ where k is the Boltzmann constant, T the temperature, m is the mass of the ion and u_{max} is the maxima of the pmf along the z coordinate. To a first approximation u_{max} varies linearly with $\Delta^{o}{}_{w}\Phi$ conferring to the IT current a Butler-Volmer type relationship with respect to the voltage difference applied to the system. Later on, Schmickler [22] incorporated ion pairing in his model to take into account its effect on interfacial capacity. Monte Carlo simulations did agree with the

significant enhancement of the capacity at the liquid/liquid interface observed by Cheng *et al.* [6].

Computer simulations [8,11-16] so far have converged toward a picture of the liquid/liquid interface in which the boundary is molecularly sharp but subject to fluctuations. Some of these fluctuations give rise to major protrusions ("fingers") of one liquid into the other. Marcus [23] developed an IT theory based on solvation/desolvation of ions induced by these interfacial protrusions. Later Komyshev *et al.* [24], following Marcus' idea, introduced a model based on coupled ion-interface dynamics in which the ion itself is capable of inducing surface protrusions.

To date there is no accepted universal theory of IT at the liquid/liquid interface. It is clear that much experimental and theoretical work is needed. Chapters III and IV deal with experimental IT investigations at micro interfaces. The main conclusion of Chapter III main conclusion is that IT of very hydrophilic ions (e.g., alkali ions) can occur at the water/1,2-dichloroethane interface only in the presence of traces (or more) of hydrophobic conterions in the organic phase. This result challenges earlier interpretations of non-assisted IT at liquid/liquid interfaces. In Chapter IV the effect of water dissolved in the organic phase is investigated and found to be critical to the transfer of very hydrophilic ions. This effect has never been observed before since in all previous IT investigations the liquid/liquid interfaces were equilibrated to allow solvents to partition into one another until saturation. Our discovery suggests a new mechanism for IT at the interface.

1.4 Principle of SECM Technique

1.4.1 SECM Principle of Operation

Figure 1.6 shows the basic setup of an SECM instrument employing an amperometric microprobe or ultramicroelectrode (UME). An UME, the tip, is attached to

a 3D piezo positioner, controlled by a computer, which is also used for data acquisition. A bipotentiostat (i.e., a four-electrode potentiostat) controls the potentials of the tip and/or the substrate versus the reference electrode and measures the tip and substrate currents. The SECM instrument is often mounted on a vibration-free optical table inside a Faraday cage to isolate it from environmental electromagnetic noise. The tip current varies depending on the environment of the tip. When the tip is positioned within a few radii of the substrate one can obtain information about the substrate.

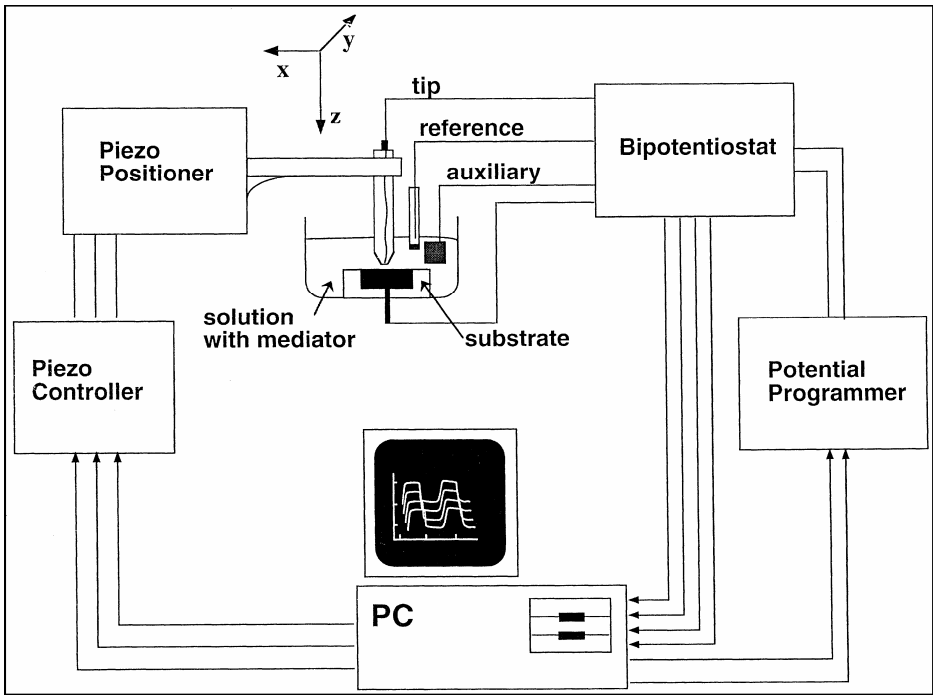

Figure 1.6. schematics of an SECM setup. (From Ref. 25).

In a feedback mode experiment, the tip is immersed in a solution containing redox mediator (e.g., an oxidizable species, R). When a sufficiently positive potential is applied to the tip, the oxidation of R occurs via the reaction

$$R - ne^- \rightarrow O \qquad (1.18)$$

at a rate governed by the diffusion of R to the UME.

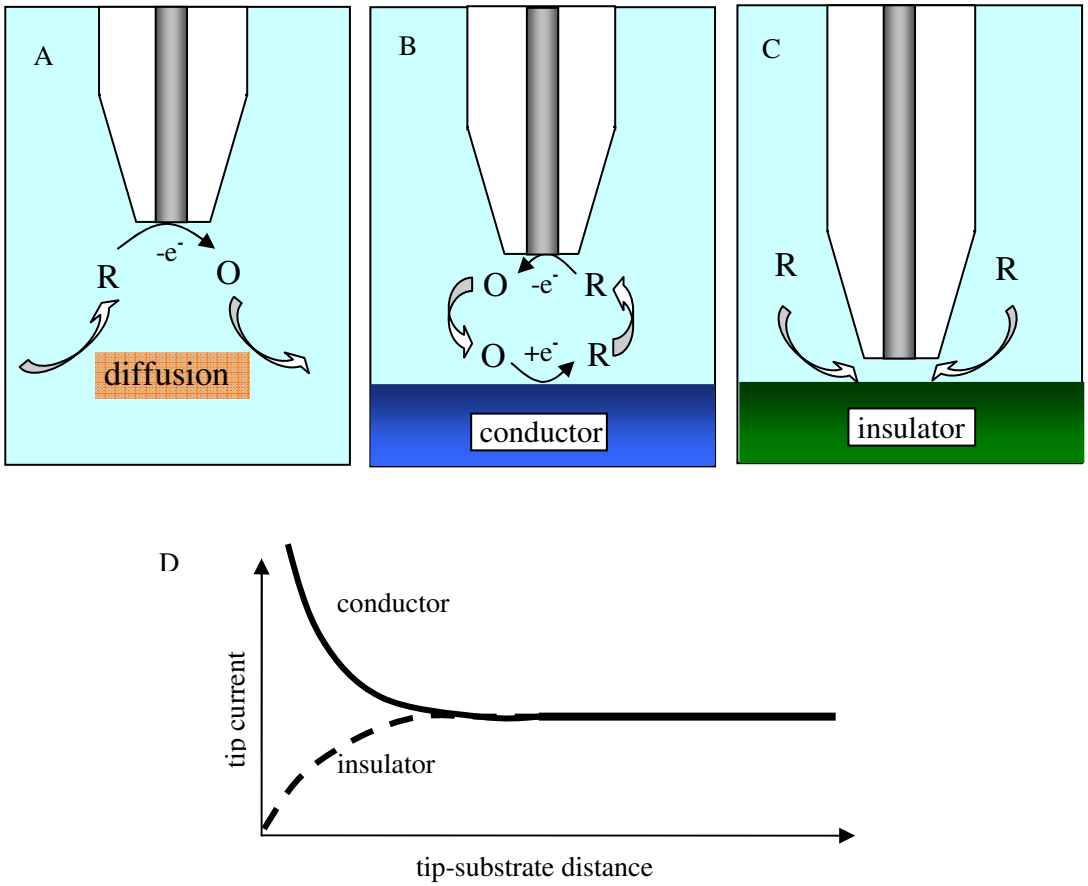

Figure 1.7. Feedback mode. A- Bulk oxidation – no feedback. B- oxidation near a perfect conductor – positive feedback. C- oxidation near a perfect insulator – negative feedback. D- Approach curves corresponding to B and C.

If the tip is far (i.e., greater than several tip diameters) from the substrate (Fig. 1.7A) the steady-state current, $i_{T,\infty}$, is given by

$$i_{T,\infty} = 4nFDca \tag{1.19}$$

where F is the Faraday constant, n is the number of electrons transferred in the tip reaction, D is the diffusion coefficient of R, c is the bulk concentration of R, and a is the tip radius.

When the tip is brought to within a few tip radii of a conductive substrate surface (Fig. 1.7B), the O species formed in the reaction (1.18) diffuses to the substrate where it may be reduced back to R

$$O + ne^- \rightarrow R \qquad (1.20)$$

This process produces an additional flux of R to the tip and hence "positive feedback", i.e., an increase in tip current ($i_T > i_{T,\infty}$). The smaller the tip-substrate distance (d), the larger is i_T. In fact, when reaction (1.20) is rapid, $i_T \rightarrow \infty$ as $d \rightarrow 0$.

If the substrate is an inert electrical insulator the tip-generated species, O, cannot react at its surface. At small d, $i_T < i_{T,\infty}$ because the insulator blocks diffusion of species R to the tip ("negative feedback"; Fig. 1.7C). The closer the tip is to the insulator substrate, the smaller i_T will be, with $i_T \rightarrow 0$ as $d \rightarrow 0$. Overall, the rate of mediator regeneration at the substrate determines the magnitude of the tip current, and conversely the measured i_T vs. d dependence ("approach curve") provides information on the kinetics of the process at the substrate.

The rate of reaction (1.20) can be controlled by applying a suitable potential to the substrate by a potentiostat. Alternatively, the potential of a conductive substrate (E_s) may be determined by concentrations of redox species in solution without an external bias. For example, if the solution contains only the reduced form of the redox species, most of the substrate, which is usually much larger than the tip, is in contact with a solution of R. According to the Nernst equation

$$E_S = E^\circ + (RT/nF)\ln(c_O/c_R) \qquad (1.21)$$

in this case $E_S - E^\circ << 0$, where E° is the standard potential of the mediator.

1.4.2 Fabrication of SECM Tips

The ultimate resolution of the SECM is limited by the size and geometry of the probe. The fabrication and characterization of the SECM probe are therefore two important steps for the acquisition of reliable data.

The SECM probe is typically an ultramicroelectrode sharpened to allow closer approach to the substrate surface [26] (Fig. 1.8). Several approaches to fabrication of SECM tips are available in the literature [27-32]. An established procedure involves heat sealing a microwire or a carbon fiber in a glass capillary under vacuum and contacting it with silver epoxy to a larger copper wire on the back side. The sealed side of the probe is polished down to 50 nm alumina and then sharpened to form a tip using coarse sandpaper. The important parameters for the tip geometry are (1) the radius, a of the conductive core; and (2) the total tip radius (insulating sheath thickness plus the radius of the electroactive area), r_g. The dimensionless parameter $RG = r_g/a$ is normally ≤ 10. This fabrication method does not require any expensive equipment, and it is widely used for the production of micron-sized tips.

A strong interest exists for the fabrication of small probes but difficulties arise when the size of the probe is such that polishing cannot be performed in a straightforward manner. Nanometer- and submicrometer-sized tips have been fabricated using different strategies. A simple way to produce nanometer-sized conical electrodes consists in etching a metal wire and then coating the etched part with an insulator while leaving the apex exposed. For example, at 125 μm diameter Pt-Ir rod was etched in a solution of saturated $CaCl_2$ and HCl at about 20 V rms ac, then insulated by dipping the metal tip into molten Apiezon wax and finally uncoated at the very end using a STM [33,34].

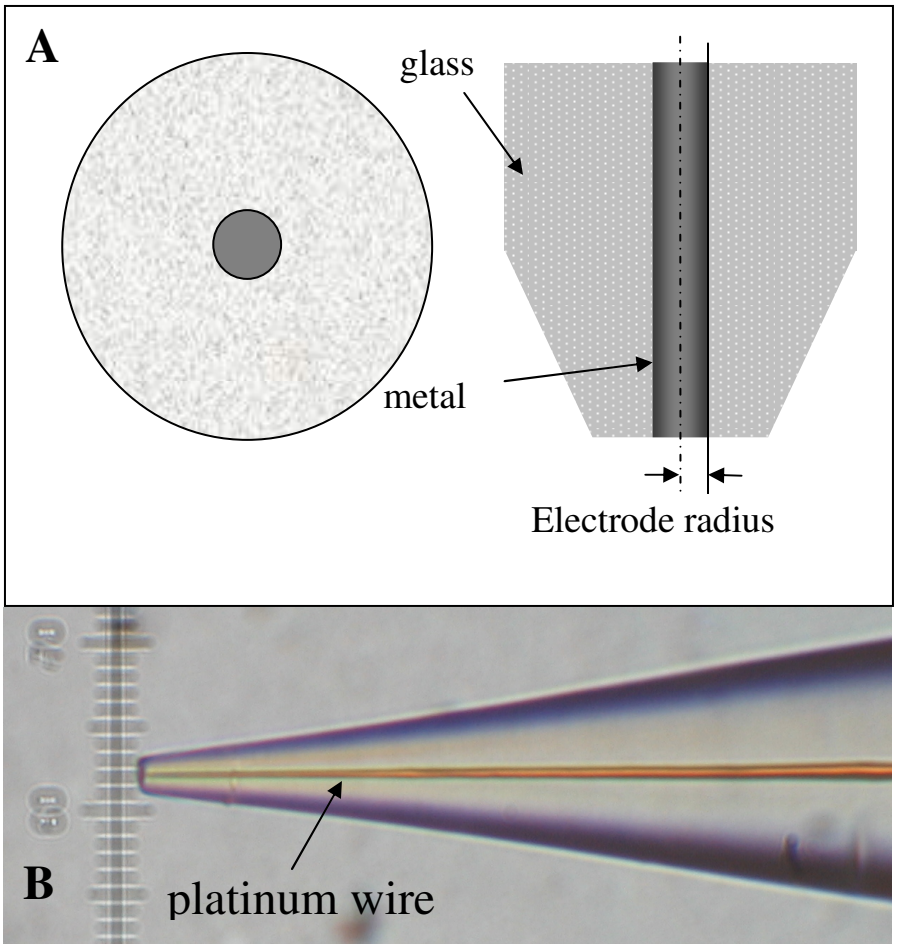

Figure 1.8. A - Schematics of a tip microelectrode. The exposed metal is the active part of the electrode. B- Optical micrograph of a UME tip. The platinum wire is sealed inside a glass sheath.

Many types of coating have been tried such as Apiezon wax [35], varnish [34,36], molten paraffin [37], silica coating [38], poly(α-methylstyrene) [39], polyimide [40], electropolymerized phenol [41] and electrophoretic paint [42].

Another fabrication method employs a micropipette puller [27-29]. Shao *et al.* [27] used a laser puller to prepare glass-sealed Pt nanodes with radii ranging from 2 to 500 nm. They attempted to polish large (>100 nm) electrodes and to characterize the tip geometry by combination of SEM, steady-state voltammetry and SECM; but the quality of the obtained approach curves was not high. A somewhat different approach to

polishing of pulled submicrometer electrodes was proposed in reference 28. Recently, it was shown that a tip as small as ~15-nm-radius can be polished on lapping tape under the video-microscopic control [29]. The polished flat nano-tips yield more reliable and reproducible data, and can be used for fast kinetic measurements.

1.4.3 SECM Steady-State Responses Theory

The quantitative SECM theory has been developed for various heterogeneous and homogeneous processes and different tip and substrate geometries. In general, theoretical SECM dependencies can be generated by numerically solving partial differential equations. In some cases, analytical approximations allow for easier generation of theoretical dependencies and analysis of experimental data. Several recent reviews focused on various aspects of the SECM theory [43]. Theoretical results presented below concern the SECM with a disk-shaped tip.

The solution of diffusion problem for two quasi-reversible ET processes occurring at the tip and substrate electrodes were first obtained in the form of two-dimensional integral equations [44]. This solution applies to both transient and steady-state feedback experiments. Since transient SECM measurements are somewhat less accurate and harder to perform, most quantitative studies were carried out under steady-state conditions. The non-steady-state SECM response depends on too many parameters to allow presentation of a complete set of working curves, which would cover all experimental possibilities. The steady-state theory is simpler and often can be expressed in the form of dimensionless working curves or analytical approximations.

a. Diffusion-Controlled Heterogeneous Reactions

The dimensionless steady-state current-distance curves were obtained numerically by Kwak and Bard [45] for both insulating and conductive substrates assuming a diffusion-controlled mediator turnover, equal diffusion coefficients, and an infinitely large substrate (The current-distance curves for microscopic substrates can be found in reference 44b).

More recently [46,47] analytical expressions were derived for several values of RG (Eqs. (1.22) – (1.24)). Equation (1.22) with the parameter values listed in Table (1.1) fits within 1% the simulated I_T – L data for a conductive substrate over the L interval from 0.04 to 10 (Fig. 1.9A, upper curve) and for RG values between 1.1 and 10

$$I_T^C(L) = \frac{i_T}{i_{T,\infty}} = A + B/L + C\exp(D/L) \tag{1.22}$$

where $L = d/a$ is the normalized tip/substrate distance. For an insulating substrate Eq. (1.23) with the parameter values listed in Table (1.2) is similarly accurate (Fig. 1.9A, lower curve) over the same ranges of L and RG values

$$I_T^{ins}(L) = \frac{i_T}{i_{T,\infty}} = \frac{1}{A + B/L + C\exp(D/L)} + \frac{EL}{F + L} \tag{1.23}$$

Another expression for the negative feedback is [47b]

$$I_T(L) = 1/\left[k_1 + k_2/L + k_3\exp(k_4/L)\right] \tag{1.24}$$

with the parameter values listed in Table (1.3). Although Eq. (1.24) is not valid for small tip/substrate distances ($L \geq 0.2$ for all RG values, and $L \geq 2$ for RG = 1.11) it can be useful for $2 < RG < 10$, and for larger RG values unavailable in Table (1.2). By fitting an experimental current-distance curve to the theory (Eqs. (1.22) – (1.23)), one can determine the zero tip-substrate separation point ($L = 0$), which in turn allows the determination of L values essential for any quantitative SECM measurement.

If a small (submicrometer) tip is to be used in quantitative measurements, it is important to show that the metal surface is not recessed into the insulator. On the other hand, a recessed tip may be produced intentionally, e.g., for single molecule detection [48]. Fan *et al.* [48b] simulated the approach curves for a recessed tip with the radius of the circular hole in the insulator equal to the disk radius. An analytical approximation for recessed tips with the hole in the insulator sheath different from the disk radius is also available [27]. The SECM feedback transients (i.e., tip current vs. time dependencies for tip/substrate distances comparable with the tip radius) for a diffusion-controlled process were simulated and analyzed in reference 49.

b. Finite Kinetics at the Substrate

The rate of an irreversible heterogeneous reaction occurring at a substrate can be extracted by fitting an experimental current-distance curve to Eq. (1.25) [50]:

$$I_T(L) = I_S\left(1 - \frac{I_T^{ins}}{I_T^c}\right) + I_T^{ins} \tag{1.25a}$$

$$I_S = \frac{0.78377}{L(1 + 1/\Lambda)} + \frac{0.68 + 0.78377/L + 0.3315\exp(-1.0672/L)}{1 + F(L,\Lambda)} \tag{1.25b}$$

where I_T^C and I_T^{ins} are given by Eqs. (1.22) and (1.23), respectively, and I_S is the kinetically controlled substrate current; $\Lambda = k_f d/D$, k_f is the heterogeneous rate constant (cm/s), and $F(L, \Lambda) = (11/\Lambda + 7.3)/(110 - 40L)$.

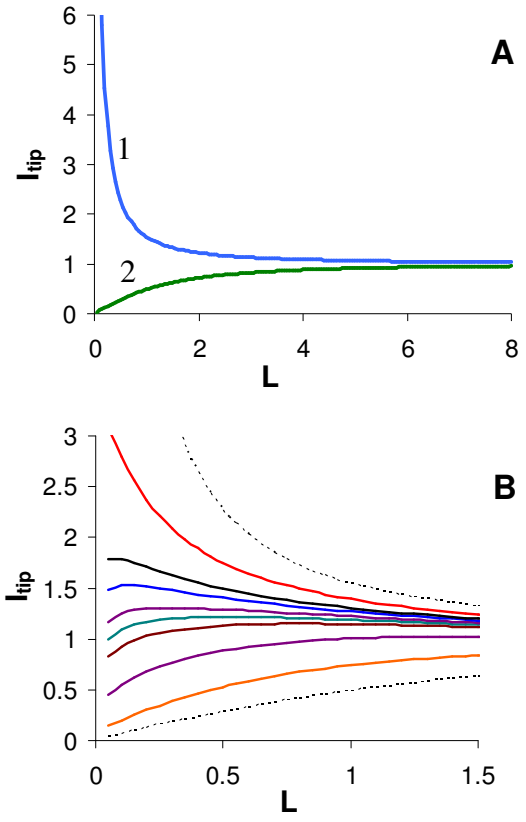

Figure 1.9. Simulated SECM current vs. distance curves. (A) totally conductive (curve 1), Eq.(1.22) and insulator (curve 2), Eq.(1.23) and (B) finite kinetics Eq. (1.25), *K* values are, from bottom to top, 0.1, 0.4, 0.8, 1, 1.2, 1.6, 2 and 4. Dashed curves are the insulator and conductors limits.

Figure (1.9B) shows the family of working curves I_T versus L calculated from Eqs. (1.25a) and (1.25b) for different values of $\kappa = k_f a/D$. The numerical results fit Eqs. (1.25a,b) over an L interval from 0.1 to 1.5 and $-2 \leq \log\kappa \leq 3$ within ~1-2%.

The radius of the portion of the substrate surface participating in the SECM feedback loop can be evaluated as $r \cong a + 1.5d$ [25b]. Thus, at small tip-substrate separations (e.g., $L \leq 2$), a large substrate behaves as a virtual UME of a size comparable with that of the tip electrode. The SECM allows probing local kinetics at a small portion of the macroscopic substrate with all of the advantages of microelectrode measurements.

Although Eq. (1.25) was developed for one-step heterogeneous ET reactions, it was shown to be applicable to more complicated substrate kinetics (e.g., liquid/liquid interfacial charge transfer [50,51], ET through self assembled monolayers [52], and mediated ET in living cells [53]). The effective heterogeneous rate constant obtained by fitting experimental approach curves to Eq. (1.25) can be related to various parameters, which determine the rates of those processes, as discussed in the referred publications.

Table 1.1. Parameter values for Eq. (1.22).

RG	A	B	C	D
1.1	0.5882629	0.6007009	0.3872741	-0.869822
1.5	0.6368360	0.6677381	0.3581836	-1.496865
2.0	0.6686604	0.6973984	0.3218171	-1.744691
10	0.7449932	0.7582943	0.2353042	-1.683087
5.1	0.72035	0.75128	0.26651	-1.6209

Table 1.2. Parameter values for Eq. (1.23).

RG	A	B	C	D	E	F
1.1	1.1675164	1.0309985	0.3800855	-1.701797	0.3463761	0.0367416
1.5	1.0035959	0.9294275	0.4022603	-1.788572	0.2832628	0.1401598
2.0	0.7838573	0.877792	0.4248416	-1.743799	0.1638432	0.1993907
10	0.4571825	1.4604238	0.4312735	-2.350667	-0.145437	5.5768952

Table 1.3. Parameter values for Eq. (1.24).

RG	k1	k2	k3	k4	% error	validity range
1002	0.13219	3.37167	0.8218	-2.34719	<1%	0.3-20
100	0.27997	3.05419	0.68612	-2.7596	<1%	0.4-20
50.9	0.30512	2.6208	0.66724	-2.6698	<1%	0.4-20
20.1	0.35541	2.0259	0.62832	-2.55622	<1%	0.4-20
15.2	0.37377	1.85113	0.61385	-2.49554	<1%	0.4-20
10.2	0.40472	1.60185	0.58819	-2.37294	<1%	0.4-20
8.13	0.42676	1.46081	0.56874	-2.28548	<1%	0.4-20
5.09	0.48678	1.17706	0.51241	-2.07873	<1%	0.2-20
3.04	0.60478	0.86083	0.39569	-1.89455	<0.2%	0.2-20
2.03	0.76179	0.60983	0.23866	-2.03267	<0.15%	0.2-20
1.51	0.90404	0.42761	0.09743	-3.23064	<0.7%	0.2-20
1.11	-1.46539	0.27293	2.45648	8.995E-7	<1%	2-20

1.5 Nanopipette Voltammetry

The advantages of studying charge transfer at micro-ITIES are similar to the ones when electrochemists use microelectrodes for voltammetric measurements; namely the reduced size leads to negligible resistive drop (to the point of being able to use neat solvents, i.e. without added electrolyte; see reference 54 chapter III and IV) and extremely small charging current. Also the increased mass transfer at micro-interfaces allows more straightforward fast kinetics measurements.

The diffusion geometry for the mass transfer at nanopipette is similar to the metal UME (Fig. 1.10). In principle Eq (1.19) can be used to estimate the diffusion-limited current from the ion transfer.

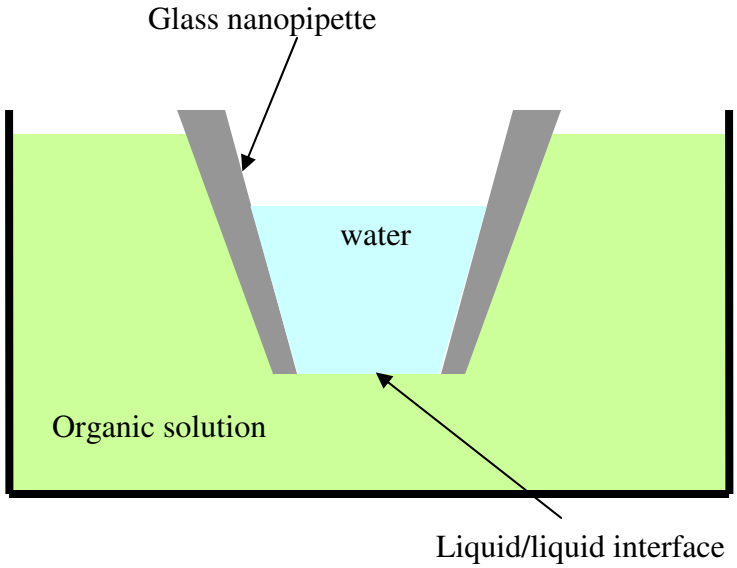

Figure 1.10. micropipette-supported ITIES setup.

In practice, Eq. (1.19) gives current values that are systematically underestimated [55-57]. One reason for this discrepancy is the seeping of water from the inside of the pipette onto the outer wall thus increasing the effective area of the interface. This effect has been empirically taken into account by modifying Eq. (1.19) to:

$$i = 3.35\pi zFDca \tag{1.26}$$

where z is the amount of charge transferred (i.e., electrons and/or ions), F is the faraday constant, D is the diffusion coefficient of the chemical species involved in the CT, c is its concentration and a is the radius of the pipette aperture. The formation of a thin aqueous layer on the outer walls of the pipette can be avoided by silanizing the exterior of the pipette [58]. Another reason for the underestimation of the current by Eq. (1.19) is the

contribution by diffusion from the back of the pipette. Eq. (1.19) is correct for an inlaid disk electrode with RG > 10 but micropipettes made of thin-walled glass capillaries can have RG values as small as 1.1. Eq. (1.27) along with Table (1.4) gives the current for silanized pipettes of different RG values:

$$i = AzFDca \tag{1.27}$$

Table 1.4. Factor *A* from Eq. (1.27) for different RG values.

RG	A
1.1	5.14
1.5	4.64
2.0	4.43
3.0	4.27
5.1	4.15
10.0	4.06

The kinetically controlled steady-state ion transfer current for micropipettes-supported ITIES is governed by a Butler-Volmer equation if the IT is effectively a one-step first-order heterogeneous reaction [59]. The current-voltage response is given by Eq. (1.28):

$$i = i_d / (\theta + 1/\kappa) \tag{1.28}$$

where $\theta = 1 + \exp\,[(\Delta^o_w\Phi - \Delta^o_w\Phi^{\prime})zF/RT]D_o/D_w$, and $\kappa = \exp\,[-\alpha(\Delta^o_w\Phi - \Delta^o_w\Phi^{\prime})F/RT]k^0/m$. k^0 and α are the standard rate constant and the transfer coefficient respectively.

1.6. SECM Experiments with Living Cells

Several SECM-based approaches have been developed to study charge transfer reactions in biological systems, including immobilized enzymes and whole cells. The SECM can also be used to image topography and reactivity of biological specimen.

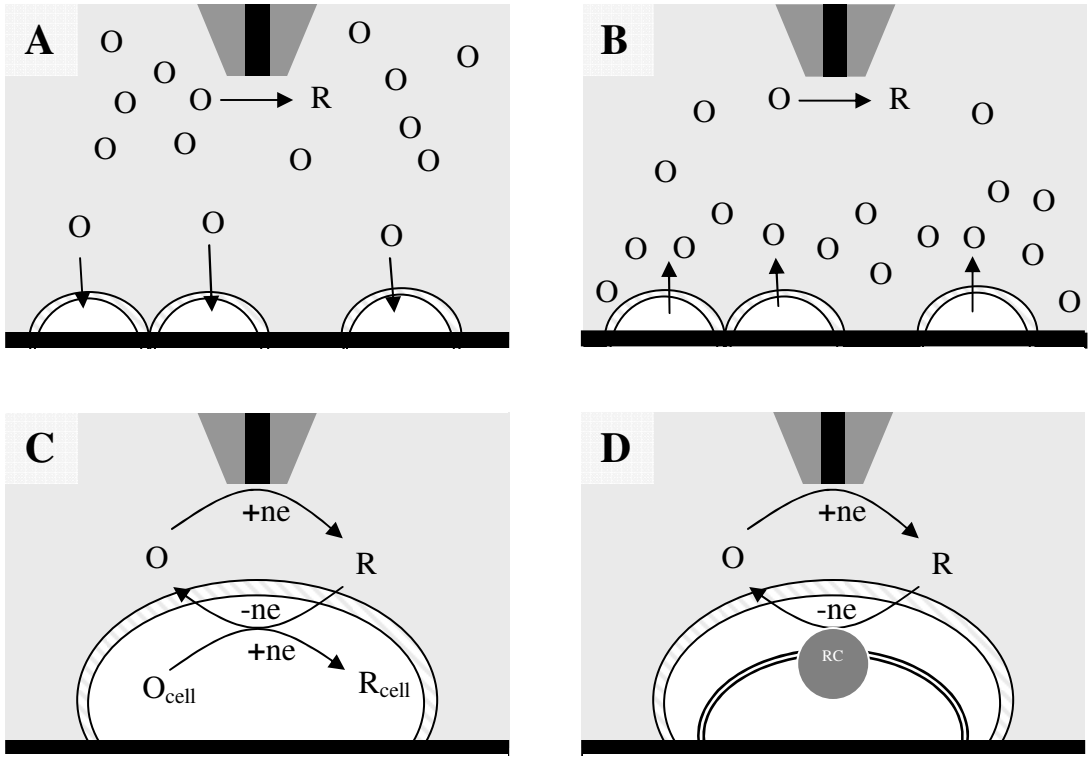

Figure 1.11. Schematic diagrams of the SECM experiments with cellular organisms. (A, B) I the SG/TC mode, the tip is used to measure the cellular activity that results either in consumption (A) or production (B) of redox species, O. (*C*) Bimolecular ET between hydrophobic redox mediator (O/R) and intracellular redox species (O_{cell}/R_{cell}). (*D*) ET between redox mediator (O/R) and redox center (RC) inside a prokaryotic cell (e.g., of *Rb. Sphaeroides*).

Two main types of SECM experiments on living cells are generation/collection measurements (Figs. 1.11A and 1.11B) and feedback-mode amperometric experiments

(Figs. 1.11C and 1.11D). The former approach involves positioning the tip in the proximity of a field of immobilized cells (or a relatively large individual cell), with a separation distance sufficiently long for the SECM feedback to be negligible. The tip in this case is used as a passive probe to monitor the concentrations and/or fluxes of redox species generated (or consumed) by the cells. In contrast, the tip/cell separation distance in a feedback mode experiment is sufficiently small to observe either positive or negative feedback from a single immobilized cell. The tip is used to oxidize (or reduce) a redox mediator, and a cell acts as a substrate whose topography and redox reactivity can be probed, as discussed in the previous sections.

1.6.1 Monitoring Respiration and Other Cellular Functions

Tip collection mode of SECM has been extensively used to study respiration and photosynthetic activities of individual biological cells. Bard and coworkers focused on plant cells [60]. They studied the bottom surface of a *Ligustrum sinensis* leaf and found several stomata structures, which are involved in photosynthesis. Tsionsky *et al*. [145] used the SECM to study the leaves of a plant, *T. fluminensis*. They imaged the topography and probed the photoelectrochemistry of single guard cells. In the dark, the stomatal pores surrounded by guard cells were opened by applying KCl solution so that high resolution topographic images could be obtained in the negative feedback mode with O_2 mediator. Ding group [61] studied oxygen evolution above single stomata in *Brassica juncea* in vivo. After the plant was treated with 0.2 mM $CdCl_2$, they found the stomatal density to be lower, and the stomata size to increase. They also found that oxygen evolution above individual stomatal complexes in Cd^{2+} treated plants was slower than that from control plants. Holt and Bard [62] studied the antimicrobial effect of micromolar concentration of $AgNO_3$ on *E. coli.* by SECM. They found the rate of

respiration increased initially on the addition of $AgNO_3$, followed by cessation of respiration.

Matsue and co-workers used the SECM to monitor respiration activities in a wide variety of living individual cells. They mapped oxygen fluxes at the cell surface associated with respiration and photosynthesis [63]. By measuring the rate of oxygen consumption, the authors addressed a number of biomedical problems ranging from drug sensitivity of cancer cells [64], to viability of a bovine embryo [65], to mitochondrial respiration in neuronal cells [66].

1.6.2 Cellular Redox Processes

Liu *et al*. applied the SECM feedback mode to non-invasively probe the redox activity of individual mammalian cells [53a,b]. In order to probe the redox activity of a mammalian cell, both oxidized and reduced forms of the redox mediator must be capable of crossing the cell membrane and shuttling the charge between the tip electrode and the intracellular redox centers (Fig. 1.11C). Only hydrophobic redox mediators (e.g., menadione and 1,2-naphthoquinone) could be used in SECM experiments with mammalian cells [53b]. The tip and intracellular redox reactions can be presented as follows:

$$O + ne = R \qquad \text{(at the tip electrode)} \qquad (1.29a)$$

$$R + O_{cell} \xrightarrow{k} O + R_{cell} \qquad \text{(inside the cell)} \qquad (1.29b)$$

The i_T vs. d curves were obtained by moving the tip (negatively biased, so that reaction 1.29a is diffusion controlled) toward the cell membrane and fitted to the theory

to extract the value of the effective heterogeneous rate constant (k). Reaction 1.29b is a complicated process involving at least three steps: (i) generation of redox centers (O_{cell}) inside the cell, (ii) transport of mediator species across the cell membrane, and (iii) bimolecular ET between the mediator species and intracellular redox centers. Mechanistic analysis showed that, depending on the properties of the mediator (e.g., formal potential, ionic charge, and hydrophobicity), the main factor limiting the overall charge transfer rate can be either the membrane transport, or the availability of intracellular redox agents, or the driving force for the ET reaction, i.e., the difference between the intracellular redox potential and the formal potential of the mediator [53b]. Kinetic parameters were determined for different steps of the charge-transfer process.

Using this approach, significant differences were detected in the redox responses given by three types of human breast cells with different levels of protein kinase C_α (PKC_α) an enzyme that has been linked with motility and metastasis of various cell types. These cell samples included: non-metastatic MCF-10A cell (a human breast epithelial cell), 11α cell (a breast cell with engineered overexpression of PKC_α), and MDA-MB-231 (a highly metastatic breast cancel cell expressing a high level of endogenous PKC_α). Approach curves obtained with these cells and several redox mediators demonstrated that their cellular redox activities are in the order of MCF-10A > 11α > MDA-MB-231. This result indicated that metastatic human breast cells can be electrochemically distinguished from non-transformed breast cells. The obtained kinetic data were used to identify the experimental conditions, such as the nature and concentration of the redox mediator, which would maximize the detection of metastatic cells in a field of normal breast cells and in tissue samples [67].

Purple bacteria (*Rb. sphaeroides*) were also investigated by SECM [68,69]. Unlike mammalian cells, *Rb. Spheroides* have two membranes (outer and cytoplasmic) and no nucleus (Fig. 1.11D). The outer membrane is permeable to both hydrophilic and hydrophobic redox species while the cytoplasmic membrane is impermeable to

hydrophilic redox species and contains redox centers. Because of this difference, ET processes in *Rb. sphaeroides* were probed using both hydrophobic and hydrophilic (e.g., $Fe(CN)_6^{3-/4-}$) redox couples. Cai *et al.* [68] found that the effective rate constant of the redox reaction of hydrophilic mediators (e.g. different quinones) with intracellular redox centers correlates with the mediator formal potential and estimated cytoplasmic and periplasmic redox potentials. Longobardi *et al*. [69] used chromatophores (specialized pigment-bearing structure obtained from the mechanical rupture of the *Rb. Sphaeroides*) and liposomes (reconstituted membrane systems) in order to investigate solely the role played by the cytoplasmic membrane of the bacterium. They found that the SECM feedback process is mediated by membrane-bound redox species (Fig. 1.11D) and that the oxidant species inside *Rb. Sphaeroides* is most probably the ubiquinone that resides in the cytoplasmic membrane pool.

The above methods for cell investigation are essentially non-invasive. However, to localize the redox activity in different cell compartments (e.g., mitochondria) the tip must penetrate the cell. The most recent effort focused on using nanometer-sized tips and nanopipette-based probes for high-resolution studies of mammalian cells [70]. It was shown that amperometric nanoprobes allow quantitative and spatially resolved SECM measurements inside living cells. The use of a tip ~1000 smaller than the cell greatly minimizes the damage to the cell membrane and may facilitate sub-cellular level studies of biologically relevant charge-transfer processes.

1.6.3 Imaging Living Cells

Most SECM images of living cells were obtained in a constant-height mode, where the tip is rastered in a horizontal (x-y) plane above the substrate surface. Using this approach, one can map the fluxes of oxygen and other redox species [63], image the cell topography under either positive or negative feedback conditions [60,71], and also

map its redox reactivity [53a]. Baur and co-workers imaged topography of single PC12 neuron cells using a constant-height mode based on the negative SECM feedback [72]. In this study, PC12 cells before and after exposure to nerve growth factor (NGF) were imaged using $Ru(NH_3)_6^{3+/2+}$ mediator. Because the cell membrane was not permeable to the redox species, it acted as an insulating substrate in topographic imaging experiments. The constant height mode was also used in combination with fluorescence microscopy to image fields of different types of human breast cells in monolayer culture [67].

A serious problem with constant-height imaging of living cells arises from significant variations in height between different parts of such a cell [72]. This problem is even more important in multi-cell imaging because different cells (and especially cells of different types) are non-uniform with respect to their size and shape [67]. Since some cells are taller than others, it is not easy to image a heterogeneous field of cells without scratching any of them with the probe. If the tip radius is smaller than the difference between the heights of two cells in the field (or the heights of different parts of the same cell), either the taller cells are scratched in the process of constant-height imaging, or the lower cells are not imaged clearly. One way to obviate this difficulty is to use a relatively large tip and to scan it within 1-2 tip radii above the cell surface. However, the use of a larger tip decreases spatial resolution.

The above problems could be largely eliminated by using a constant-distance mode of SECM imaging. This approach requires a distance-dependent signal and a feedback circuit, so that the tip could move up and down to remain at a constant distance from the imaged object. Different ways of doing it have been proposed including constant current mode [73], tip position modulation [74], the use of shear force-based feedback [75,76], the AFM-SECM combination and tuning forks [77,78]. Schuhmann and co-workers applied constant-distance control based on an optical detection of shear forces to study vesicular release at single PC12 cell using SECM [79]. A carbon fiber microelectrode insulated by electrodeposition and dip-coating methods exhibited good

stiffness and vibration characteristics for shear-force-based imaging. Topographic images of individual PC12 cells were obtained by recording the *z*-displacement during the scans, while the shear-force (and consequently the tip/cell distance) was set constant.

An alternative approach—to use the impedance of the SECM tip as the distance-dependent signal—was introduced by Horrocks *et al.* [80] and further developed by others [81,82]. The tip impedance is monitored by application of a high-frequency ac voltage bias between the tip and the auxiliary electrode, so that it can be separated from the lower frequency voltammetric signals. By employing a piezo-based feedback controller, one can keep the impedance at a constant value and, thus, maintain a constant tip/substrate separation distance [81].

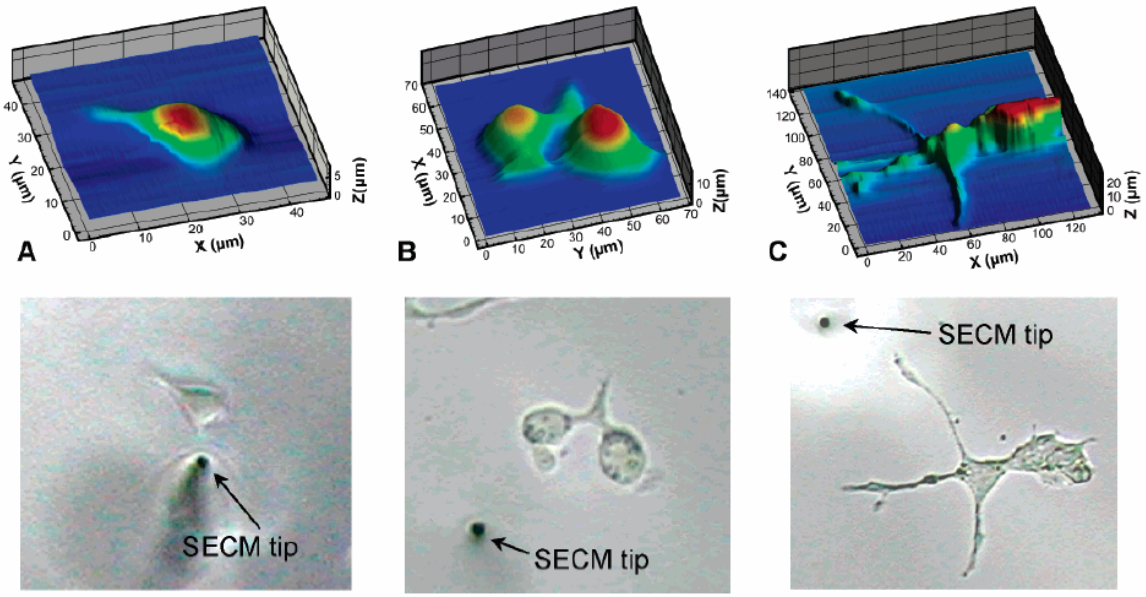

Figure 1.12 Topographic images acquired using constant-impedance mode with a 1-μm carbon ring tip. (A) Undifferentiated PC12 cell; (B) PC12 cells in the early stage of neurite development following exposure to NGF; (C) differentiated PC12 cell.

The imaging can take place directly in the cell growth media, and no redox mediator is required. Using this technique, Kurulugama *et al.* [83] obtained high quality constant-distance images of model neurons. The highest resolution was achieved using an ~1-μm-diameter carbon ring electrode (Fig. 1.12). The use of nanometer-sized tips, which should become available for cellular SECM imaging within the next one or two years, may increase the lateral resolution from submicrometer range to about 10–20 nm.

1.6.4 Membrane Transport

The transport of molecules across biological cell membranes, including planar bilayer lipid membranes (BLMs) and giant liposomes has been studied by SECM. The approaches used in those studies are similar to generation/collection and feedback SECM experiments. In the former mode, an amperometric tip is used to measure concentration profiles and monitor fluxes of molecules across the membrane. In a feedback-type experiment, the tip process depletes the concentration of the transferred species on one side of the membrane and in this way induces its transfer across the membrane.

Tsionsky *et al.* studied charge transport through the horizontally oriented BLM that separated the upper and lower compartments containing the same solution [84]. The bilayer was impermeable to hydrophilic ions like $Ru(NH_3)_6^{3+}$ and $Fe(CN)_6^{4-}$ and completely blocked ET between such species. However, the transmembrane ET current was observed when the BLM was doped by iodine. Using a similar experimental arrangement, Amemiya and Bard probed the transport of K^+ through gramicidin channels formed in horizontal BLMs [85]. The amperometric ion-selective micropipette electrodes used in those experiments were filled with a 10 mM valinomycin solution in 1,2-dichloroethane or 10 mM ETH 500. Both feedback and generation-collection modes were employed to investigate the transfer of K^+. In a somewhat similar manner,

hydrophilic ion transfer through the voltage-gated channel formed in BLM by alamethicin was studied by Wilburn *et al*. [86] The pore formed by several alamethicin molecules was sufficiently large and hydrophilic to transport redox species such as $Ru(NH_3)_6^{3+}$ and $Fe(CN)_6^{3-}$, which could be detected by the Pt tip.

Two interesting examples of SECM studies of molecular transport across biological membranes were reported by Mauzeroll *et al.* [87,88] They measured the uptake of menadione by yeast cells and monitored its intracellular reaction with glutathione [87]. The export of the product of that reaction (thiodione) by ATP-dependent GS-X pumps is the way for a yeast cell to get rid of toxic menadione (Fig. 18). Because yeast cells are much smaller than either mammalian cells or purple bacteria used in other SECM studies, it was not possible to probe them individually.

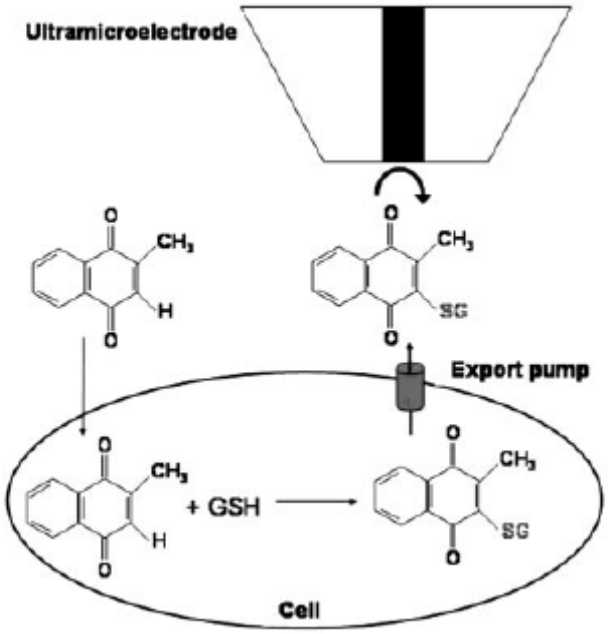

Figure1.13 Menadione-imposed oxidative stress on cells leads to the formation and excretion of thiodione into the extracellular media, where it can be detected by using SECM.

The average flux of about 30,000 thiodione molecules per second per cell was measured by a 1-μm-diameter tip, and numerical simulations were used to show that the overall process rate is limited by the uptake of menadione. The efflux through the GS-X pump was found to be at least an order of magnitude faster. In the second article [88], the thiodione efflux from individual cells and groups of highly confluent hepatoblastoma (Hep G2) cells was determined by monitoring the evolution of concentration profiles above the cells. A flux of 6.0×10^6 molecules per second per cell was calculated.

A novel application of SECM was to study transport processes across the nuclear envelope. Guo and Amemiya investigated the molecular transport facilitated by nuclear pore complexes (NPCs) in a large intact nucleus of *Xenopus laevis* oocytes [89]. The NPC is a 60-120 MDa complex made of 30 or more distinct proteins. Small molecules can passively diffuse through it. The partitioning of redox species X across the nuclear envelope

$$\text{X (outer solution)} \rightleftarrows \text{X (nucleus)} \tag{1.30}$$

was characterized by obtaining approach curves and chronoamperograms. From such experiments performed with different mediators, the authors concluded that the nuclear envelope permeability is very high, and most NPCs on the nucleus are open. Estimates were obtained for the single-channel flux and the NPC diameter.

Most recently, Zhan and Bard used submicrometer-sized conical carbon fiber tips to approach, image, and puncture individual giant liposomes containing $Ru(bpy)_3^{2+}$ [90]. The leakage of $Ru(bpy)_3^{2+}$ through the lipid membrane was observed. A higher stability of liposomes as compared to lipid bilayers allows one to perform measurements over a more extended period of time. Such “artificial cells” can be useful for studies of molecular transport and redox regulation of cellular processes.

Chapter II

Electron transfer at the water/IL interface studied by SECM

2.1 Introduction

Ionic liquids (IL) have attracted significant attention during the last several years because of their applications in liquid-liquid extraction, solar energy conversion, and synthetic chemistry [1-3]. ILs offer advantages over conventional organic solvents for various applications. For example in solvent extraction, ILs could potentially replace conventional solvents because they are environmentally friendly, non-volatile, and recyclable [4]. Highly conductive and chemically stable ILs can be employed in solar cell technology to enhance the conversion efficiency and widen the potential window [5]. These and other potential applications require better understanding and control of the interfacial phenomena occurring at the IL/water and IL/metal interfaces.

In a previous communication [6] the electron transfer (ET) reaction between ferrocene (Fc) dissolved in IL and aqueous ferricyanide was studied by scanning electrochemical microscopy (SECM). Ferrocyanide was oxidized at the tip electrode

$$Fe(CN)_6^{4-} - 1e \rightarrow Fe(CN)_6^{3-} \qquad (2.1)$$

and regenerated at the IL/water interface

$$Fc(IL) + Fe(CN)_6^{3-}(w) \rightarrow Fc^{+}(IL) + Fe(CN)_6^{4-}(w) \qquad (2.2)$$

ET reactions at the interface between two immiscible electrolyte solutions (ITIES) have been actively studied by various electrochemical techniques including SECM [7,8].

In all previous studies, the two phases were water and an organic solvent immiscible with it. Some interesting new features of the ET dynamics at the water/IL interface can be expected because of the major differences between ILs and conventional organic solvents, i.e., significantly higher viscosity of and very high ionic concentrations in ILs. In ref. 6, the rate of reaction (2.2) was evaluated from the tip current vs. distance ($i_T - d$) curves [8]. The driving force dependence of the effective bimolecular rate constant (k_f) measured for reaction (2.2) was in agreement with the Butler-Volmer model. In contrast, the finding that the standard rate constant of ET at the water/IL interface was significantly higher than that of the same reaction at the water/DCE interface was hard to reconcile with the existing ET theory. Here, we explore the possibility of using various combinations of aqueous and IL-soluble redox couples to obtain information on the driving force dependence and other factors affecting the ET dynamics at the water/IL interface.

The IL used in our studies, 1-octyl-3-methylimidazolium bis(trifluoromethylsulfonyl)imide ($C_8mimC_1C_1N$) is immiscible with water and forms a nonpolarizable interface when in contact with it. We also probed the ET reaction at the interface between aqueous solution and the mixture of the IL and 1,2-dichloroethane (DCE) [6]. By varying systematically the mole fractions in this mixture, we investigated the transition from the water/organic to the water/IL interface. It was noticed that Fc partitions from $C_8mimC_1C_1N$ to water more readily than from a typical organic solvent, e.g., DCE. Unlike water/organic solvent interface, the contribution of the direct oxidation of Fc at the tip in the aqueous phase is not negligible. This difference is illustrated in Figure (2.1). At the water/organic interface (Fig. 2.1A) the tip current is produced solely by oxidation of ferrocyanide, and the regeneration of this mediator species via the interfacial reaction with Fc results in the positive feedback. In contrast, at the water/IL interface

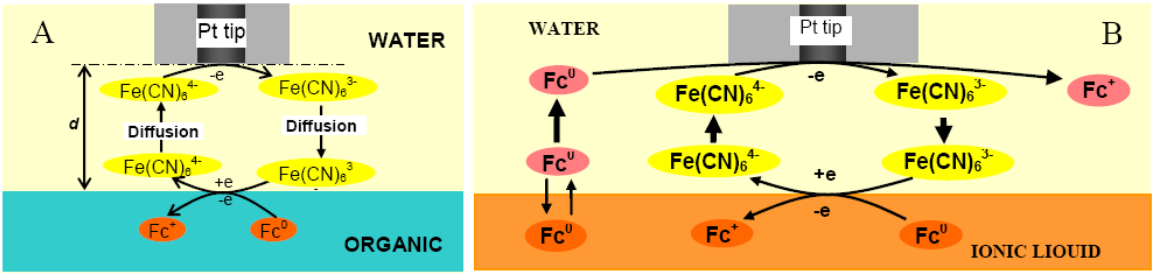

Figure 2.1. Scheme of SECM feedback experiment at the water/organic interface (A), and SECMIT/feedback experiment at the water/IL interface (B).

(Fig. 2.1B), two reactions occur simultaneously at the tip surface, i.e., oxidations of ferrocyanide and Fc. The latter process results in the depletion of Fc concentration near the liquid/liquid interface and induces its transfer from IL to water. This phenomenon was called SECM induced transfer (SECMIT) [8,9]. In order to study the kinetics of the interfacial ET, the i_T component due to reaction (2.2) has to be separated from the current component produced by direct oxidation of Fc in water. Below, we show how the contributions of these processes to the tip current can be separated by analysis of the SECM current vs. distance curves.

The determination of the partition coefficient (K) of neutral species at the water/IL interface is essential for application of ILs as solvents in chemical separations (e.g., solvent extraction), The determination of K is complicated by slow molecular diffusion in IL and consequently slow solute equilibration between two liquid phases. For example, the diffusion coefficient of 1,1'-diethylferrocene in $C_8mimC_1C_1N$ is 45 times smaller than in DCE [6]. Here, we show that by using SECM, one can evaluate K under quasi-steady-state conditions without waiting for the complete solute equilibration to occur.

2.2 Experimental Section

Chemicals.

Lithium bis(trifluoromethylsulfonyl)imide (LiC_1C_1N), NaCl, KCl, $K_4Fe(CN)_6$, 1-methyl-3-octylimidazolium chloride (C_8mimCl), ferrocene (Fc), N-methylphenothiazine (MPTZ), decamethylferrocene (DcMFc), and ruthenocene (Rc), were purchased from Aldrich; tetrathiafulvalene (TTF), K_3IrCl_6, 1,1'-diethylferrocene (DEFc), decamethylruthenocene (DcMRc) and N-butylferrocene (BuFc) were from Strem Chemicals. $Na_4Ru(CN)_6$ and 1-methyl-3-octylimidazolium-bis(tetrafluoromethylsulfonyl)imide ($C_8mimC_1C_1N$) were synthesized as described previously [10b,11]. DEFc and BuFc were purified by column chromatography; Fc and MPTZ were purified by double sublimation. Other chemicals were used as received. All aqueous solutions were prepared from deionized water (Milli-Q, Millipore Corp).

Electrodes and Electrochemical Cells.

The working electrode (radius, a = 5.3 μm) was prepared as follows. A capillary tube of borosilicate glass (10 cm long, OD = 2mm, ID = 1mm) was pulled into a short, patch-type pipette using a model P-2000 laser puller (Sutter Instrument Co., USA). The pulled end of the capillary was then gently heat sealed. A 2 cm long Pt wire (5.3 μm radius, Goodfellow, Cambridge, U.K.) was inserted up to the sealed end of the capillary. The tip was heat sealed again under vacuum. A lager wire was connected to the Pt wire using silver epoxy and fixed outside of the capillary with Torr-Seal epoxy. The tip was coarsely polished until the platinum wire was exposed, and then further polished using a micropipette beveller with the pipette-holder in a strictly perpendicular position with respect to the grinding plates (15, 1, and 0.05 micron alumina; Sutter). Finally, the tip was sharpened by hand to reduce its RG (i.e., the ratio of the glass radius to a) to 10 without touching the platinum disk. The advantage of this method is that by reducing the capillary diameter before sealing the wire one could sharpen the tip more easily and

accurately. The RG could be reduced by hand to values less than 2 for a 10-micron-diameter electrode. An RG of 10 was chosen to facilitate the fitting of the experimental curves to the theory for the finite kinetics at the substrate, which is only available for RG = 10 [10a]. The tip used to probe Fc partitioning had an RG of ~3.

The counter electrode was a 2-cm long, 2-mm-diameter platinum wire, and a Ag/AgCl (filled with 3 M KCl) electrode was used as a reference. In all experiments, the three electrodes were placed in the aqueous phase, except for the measurements of the formal potential of ferrocene in IL where the working electrode was immersed in the IL. The electrolyte used in the aqueous phase was a mixture of KCl and either C8mimCl or LiC1C1N with the constant ionic strength of 250 mM. Fc (or other redox species) was dissolved in IL with no electrolyte added. The electrochemical cell was a 2-cm-diameter, 1-cm high glass cylinder. The denser ionic liquid formed a ~2-mm-diameter drop at the bottom of the electrochemical cell when the latter was filled with an aqueous solution. All experiments were performed after 30 min rest period once the two liquids were put into the cell.

SECM Apparatus and Procedure.

The basic apparatus used for the SECM experiments has been described previously [6,10]. To obtain a current vs. distance curve, the tip was positioned above the center of the IL drop by scanning it laterally in the x-y plane until the maximum feedback current was reached. The tip was biased at a potential where the oxidation (or reduction) of the aqueous redox mediator occurred at a diffusion-controlled rate. The approach curves were obtained by moving the tip toward the interface at a rate of 0.2 μm/s and recording the tip current as a function of the tip/ITIES separation distance.

With all 3 electrodes placed in the top, aqueous phase, electron transfer across the ITIES must be accompanied by the transfer of ions between the two phases to maintain the IL electroneutrality. In experiments involving organic solvents with added electrolyte, the

charge compensatory ion transfer may become the rate limiting step [10]. Because the ionic constituents of the IL can partition into the aqueous phase, ion transfer does not limit the overall charge-transfer rate at the water/IL interface. In all SECM experiments one of those ions was also dissolved in water and served as a common ion. Since both concentrations of C_8mim^+ and $C_1C_1N^-$ in the IL phase are constant, the potential drop across the nonpolarizable ITIES ($\Delta^{IL}_{w}\varphi$) was determined by the common ion concentration in aqueous solution [6]:

$$\Delta^{IL}_{w}\varphi = \text{const} + 0.059\log [C_8mim^+]_w \quad (2.3a)$$

or

$$\Delta^{IL}_{w}\varphi = \text{const} + 0.059\log [C_1\ C_1N^-]_w \quad (2.3b)$$

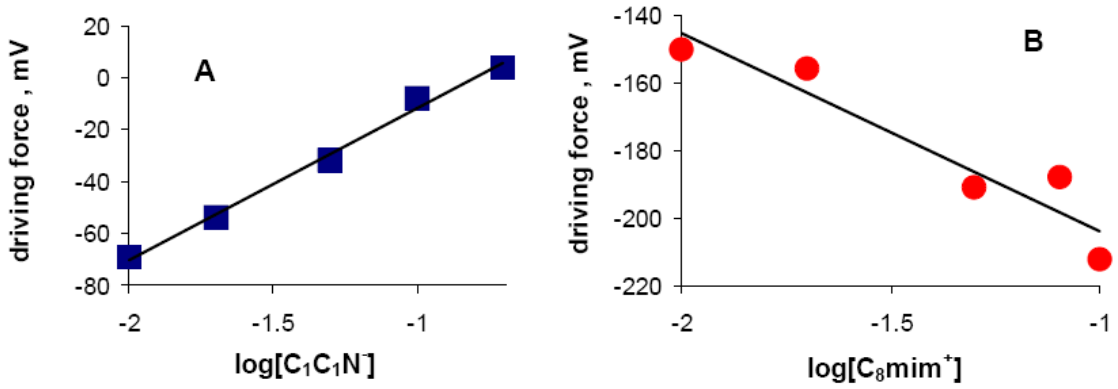

Figure 2.2. Dependence of the driving force on concentration of the common ion in the aqueous phase. The driving force for reaction (2.2) was evaluated as the difference of the half-wave potentials of ferrocyanide in water and Fc in IL measured with respect to the same aqueous Ag/AgCl reference electrode.

In this way, $\Delta^{IL}_{w}\varphi$ and the driving force for the interfacial ET (i.e., the difference of the half-wave potentials of the aqueous redox couple and that dissolved in IL, $\Delta E_{1/2} \cong E°(w)$

– $E°$(IL) [6,10b]) can be varied over the range of ~220 mV. The slopes of experimental dependences of the half-wave potential of Fc ($E_{1/2}$) dissolved in IL vs. $[C_8mim^+]_w$ and $[C_1C_1N^-]_w$ in water were found to be 58.6 mV/decade and 58.2 mV/decade in agreement with Eqs. (2.3a) and (2.3b) [6]. The experimental dependences of the driving force for the interfacial ET vs. $[C_8mim^+]_w$ and $[C_1C_1N^-]_w$ are shown in Figure (2.2).

To avoid the diffusion limitations in the bottom (IL) phase, the steady-state diffusion limiting current of the redox species in the IL must be at least 15 times higher than the current to the same electrode in the aqueous phase [10b]. This requirement leads to the following relationship between the bulk concentrations and diffusion coefficients of the redox species in water and IL phases:

$$c_{IL}^{*} / c_{w}^{*} \geq 15\, D_w / D_{IL} \qquad (2.4)$$

Because of high viscosity of ILs, this condition is much more stringent for the water/IL interface than for the water/organic interface. In all our experiments at the water/IL interface, the concentration ratio was maintained at 500 (e.g., 100 mM Fc in IL and 200 μm $Fe(CN)_6^{4-}$ in water) so that condition (2.4) was satisfied despite the large difference in diffusion coefficient values of ferrocyanide in water and ferrocene in IL (6.4 x 10^{-6} cm^2/s and 2.6 x 10^{-7} cm^2/s, respectively). Because of the low concentration of the aqueous mediator and a high concentration of redox species in IL, the partitioning of the latter species into water made a significant contribution to the tip current.

2.3 Results and Discussion

Determination of the Partition Coefficient.

To study Fc partitioning from IL to water, a series of experiments were conducted in which the concentration of ferrocene in IL was varied while no redox species were

dissolved in the aqueous phase. Two current vs. distance curves shown in Figure (2.3) were obtained in 15 minutes (curve 1) and one hour after the two liquids were placed into the SECM cell. The current in Fig. (2.3) is produced by Fc oxidation at the tip:

$$Fc_w \rightarrow Fc_w^+ + e \qquad (2.5)$$

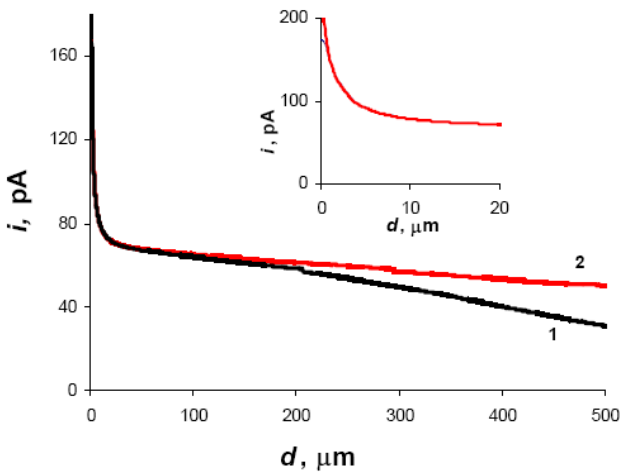

Figure 2.3. SECM long-range current vs. distance curves for a 5.3 μm-radius Pt tip UME in water approaching the IL/water interface. The tip was biased to +500 mV vs. Ag/AgCl. C8mimC1C1N phase contained 130 mM Fc; aqueous solution was 210 mM in KCl and 40 mM in LiC_1C_1N. The approach curves were obtained after 15 min (1) and 1 hour (2) since the ITIES formation. Inset: superimposed short-distance portions of the two current-distance curves.

The distance scale in Fig. (2.3) is much longer than that in a conventional feedback-mode approach curve, where i_T reaches the bulk value ($i_{T,\infty}$) at $d \sim 10a$ [8]. In contrast, in Fig. (2.3), the tip current continues to decrease at much longer separation distances, e.g., $d \sim 90a$. This distance scale corresponds not to the tip radius, but to that of a much larger substrate (i.e., a quasi-hemisphere with a radius, r_0 ~1 mm). The thickness

of the Fc diffusion layer in the aqueous phase corresponding to the 15 min diffusion time is ~1 mm (the diffusion coefficient of Fc, $D_{Fc,w}$ = 4.4 x 10^{-6} cm^2/s was obtained from the steady-state diffusion limiting current at a 5.3-μm disk measured in a 20 μM aqueous solution of Fc; Figure (2.4)).

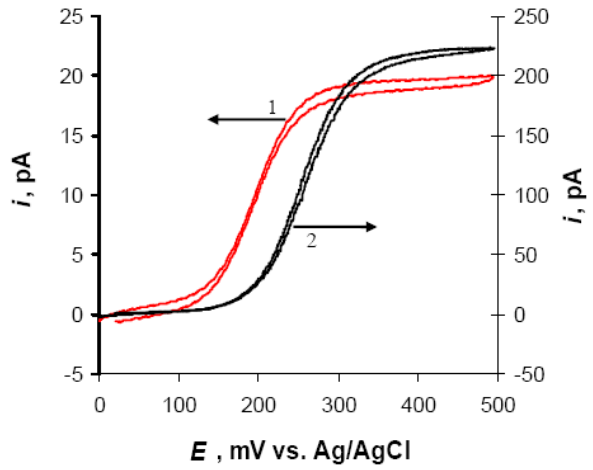

Figure 2.4. Cyclic voltammograms of 20 μM ferrocene (1) and 200 μM ferrocyanide (2) at a 5.3-μm Pt electrode in aqueous solution containing 100 mM LiC_1C_1N and 100 mM KCl.

One should notice that the curves 1 and 2 in Fig. (2.3) are essentially identical at shorter distances from the interface (e.g., $d \leq 50$ μm). This can be explained by considering the concentration profile of Fc in the aqueous phase. Assuming that the IL drop was a hemisphere with a radius, r_0 = 1 mm, the concentration profile of Fc within the diffusion layer can be approximately calculated from Eq. (2.6) [12]

$$\frac{c_{Fc,w}(d,t)}{c_{Fc,w}(0,t)} = \frac{r_0}{r_0 + d} erfc\left(\frac{d}{2\sqrt{D_{Fc,w}t}}\right) \tag{2.6}$$

where $c_{Fc,w}(0,t)$ is the concentration of Fc in water near the phase boundary at the time t and $c_{Fc,w}(d,t)$ is the concentration value at the vertical distance d from the interface (Figure 2.5).

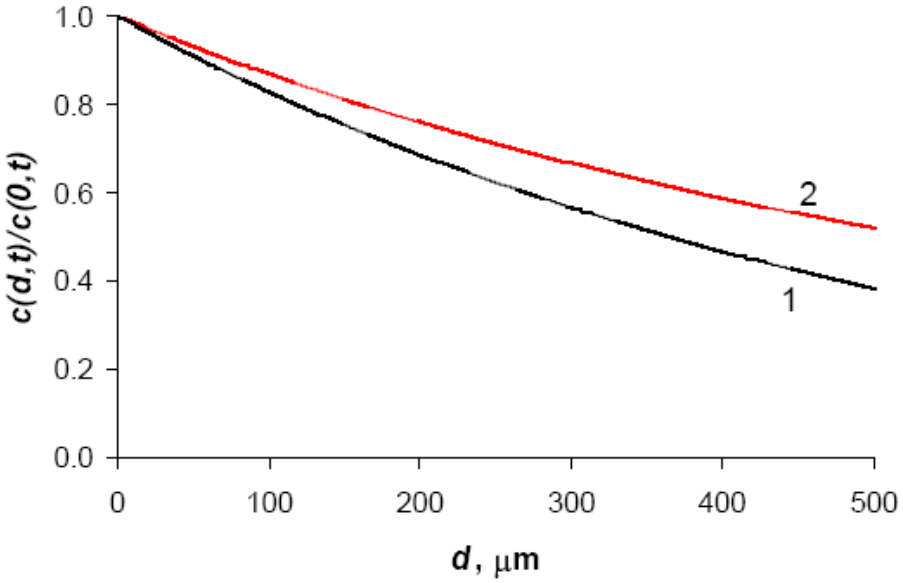

Figure 2.5. Normalized concentration profiles of Fc in water calculated from Eqs. (2.6) and (2.8) for 15 min (1) and 1 hour (2) of diffusion time.

Because the partitioning of neutral Fc species is a diffusion-controlled, equilibrium process [9],

$$c_{Fc,w}(0,t) = c_{Fc,IL}(0,t)/K \tag{2.7}$$

where K is the water/IL partition coefficient of Fc. Since K is a large (see below), the depletion of Fc in IL is negligible, and therefore $c_{Fc,IL}(0,t) = c^*_{Fc,IL}$, and

$$c_{Fc,w}(0,t) = c^*_{IL,Fc}/K = \text{const} \tag{2.8}$$

From Fig. (2.5), one can see that close to the interface (e.g., within 50-μm distance) the differences between Fc concentrations at t = 15 min and t = 1 hr are small. The diffusion of Fc in a thin layer of solution adjacent to the interface reaches a quasi-steady-state. Accordingly, two SECM $i_T - d$ curves (inset in Fig. (2.3)) obtained at t = 15 min and t = 1 hr after the formation of the water/IL ITIES with the maximum d = 20 μm, which corresponds to ~4 tip radii, are practically indistinguishable.

Since the concentration of Fc within the 20-μm distance range varies only by ~2% (Fig. (2.5)), a short-range approach curve can be fit to the conventional theory for the diffusion-controlled positive feedback assuming uniform concentration of Fc in solution, Eq. (2.9)

$$I^c_T = 0.78377/L + 0.3315 \exp(-1.0672/L) + 0.68 \qquad (2.9)$$

where $I^c_T = i_T/i_{T,\infty}$ is the normalized tip current under pure positive feedback conditions for the given normalized distance, $L = d/a$, and $i_{T,\infty} = 4FaD_{Fc,w}c^*_{Fc,IL}/K$. An excellent fit was obtained between the experimental current-distance curve and the theory (Figure (2.6A)). A very high maximum value of the normalized feedback current (~12) agrees with the earlier finding that the interfacial transfer of a neutral Fc species is diffusion controlled [8a,9].

The water/IL partition coefficient of Fc, K = 2400, was obtained from the $i_{T,\infty}$ value, which was used as a single fitting parameter in Fig. (2.6A). Essentially the same value of K was obtained for various concentrations of Fc in $C_8mimC_1C_1N$, from 5 mM to 100 mM. A strictly linear $i_{T,\infty}$ vs. $c^*_{Fc,IL}$ dependence in Fig. (2.6B) confirms the validity of this procedure. The determined K is lower than that for water/nitrobenzene (7000 [13])

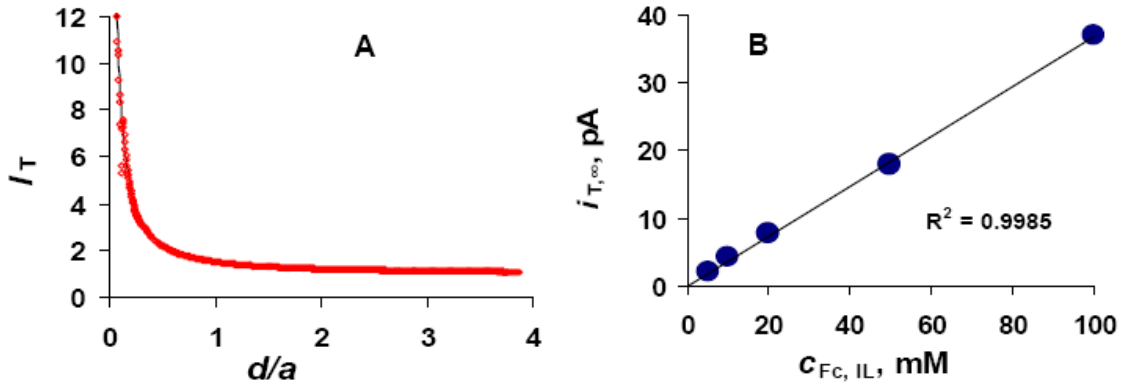

Figure 2.6. Experimental (symbols) and theoretical (solid line) short-range current-distance curves for Fc partitioning between IL and water (A) and correspondent dependence of the tip current on concentration of ferrocene in the IL (B). t = 1 hr. For other parameters, see Fig. (2.3).

and somewhat higher than the value found for the same system but with 0.1 M tetraethylammonium perchlorate dissolved in nitrobenzene (1200 [10a]).

An advantage of our SECMIT approach is that one can determine the partition coefficient without waiting for the complete equilibration of the solute between two liquid phases. In case of viscous ILs, the equilibration may require a considerable time. High positive feedback (Fig. (2.6A)) provides an amplification of the signal, which is advantageous when the concentration of the partitioning species and $i_{T,\infty}$ are low.

Separation of Heterogeneous ET and Solute Partitioning at the Water/IL Interface. Since the transfer of Fc into the aqueous phase is not negligible, the contribution of direct oxidation of Fc at the tip to I_T (Fig. (2.1B)) has to be taken into account:

$$I_T = I_{ET} + I_{part} \tag{2.10}$$

where I_{ET} and I_{part} the current components produced by reactions (2.1) and (2.5), respectively. All variables in Eq. (2.10) are normalized by the tip current of the oxidation of aqueous redox mediator in the bulk solution

$$i_{T,\infty} = 4FaD_{Fe(CN)_6^{4-}} c^*_{Fe(CN)_6^{4-}} \tag{2.11}$$

In addition to reactions (2.1), (2.2) and (2.5), homogeneous ET reaction (2.11) in the aqueous phase

$$Fc(w) + Fe(CN)_6^{3-}(w) \xrightarrow{k} Fc^+(w) + Fe(CN)_6^{4-}(w) \tag{2.11}$$

may also influence the tip current. To check if this effect is significant, one can evaluate the forward rate constant of reaction (2.12) using the Marcus formula

$$k = \sqrt{k_{11}k_{22}K_{12}f} = 1.3 \text{ x } 10^6 \text{ M}^{-1}\text{s}^{-1} \tag{2.12}$$

where the self-exchange rate constants for ferrocene and ferrocyanide are $k_{11} = 6$ x 10^6 $M^{-1}s^{-1}$ and $k_{22} = 2.4$ x 10^2 $M^{-1}s^{-1}$, respectively [14], $f \sim 1$, and $K_{12} = \exp(-nF\Delta E°/RT) \cong 11$ for $\Delta E° = 61$ mV (Fig. (2.4)). The dimensionless kinetic parameter that can be used to assess the effect of the bimolecular reaction (2.11) under SECM conditions [15] is $\kappa = a^2 k c_{Fc,w}/D_{Fe(CN)_6^{4-}} < 10^{-3}$. This estimate shows that the rate of reaction (2.11) in the forward direction is immeasurably slow under our experimental conditions [15]. The rate constant of the reverse reaction is even slower because of the smaller K_{12} value.

Since the effect of the cross-reaction between $Fc^{+/0}$ and $Fe(CN)_6^{3/4-}$ is negligible, the I_{ET} and I_{part} contributions to the tip current are mutually independent, and I_{ET} can be evaluated by subtracting the I_{part} component from the measured I_T. An example of such subtraction is shown in Figure (2.7). The experimental approach curve (1) was obtained with $[C_8mim^+]_w$ = 100 mM, which corresponds to the driving force for reaction (2.2), $\Delta E_{1/2}$ = -217 mV (Fig. 2B).

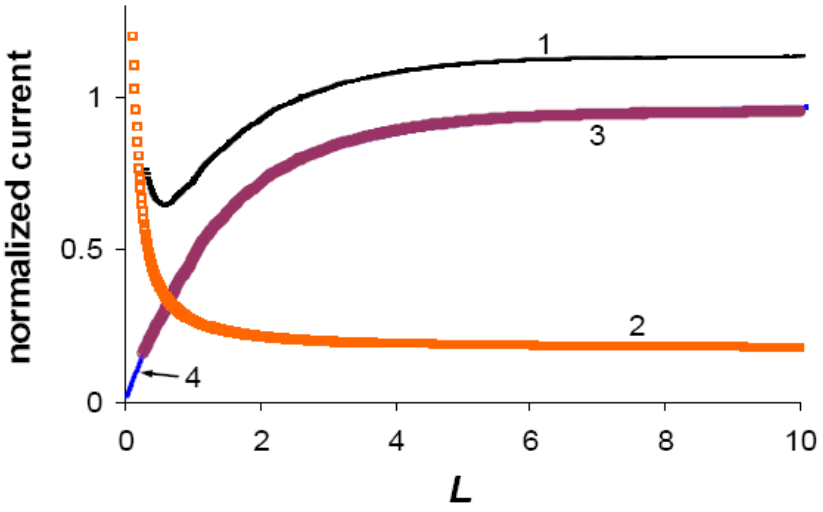

Figure 2.7. Separation of solute partitioning and ET. (1) Experimental current–distance curve for a 5.3-μm Pt tip approaching 100 mM solution of Fc in IL. Aqueous solution contained 200 μM and 100 mM C_8mim^+. (2) I_{part} vs. L curve for Fc partitioning between IL and water. (3) I_{ET} vs. L curve obtained by subtracting curve (2) from curve (1). (4) Theory for pure negative SECM feedback [16].

At such a large negative driving force, the SECM feedback in Fig. (2.7) must be negative. After the subtraction of the I_{part} component (curve 2) from curve 1, the resulting curve 3 corresponds to the I_{ET} the vs. L dependence. An excellent fit between this curve and the theory for pure negative feedback [16] (curve 4) confirms the validity of Eq.

(2.10) and the subtraction procedure. Since ferrocene is a neutral molecule, its partitioning between IL and water is independent of the interfacial potential drop. The current-distance curves similar to that in Fig. (2.6A) and showing pure positive feedback were obtained for various $\Delta^{IL}_{w}\varphi$ and $c^{*}_{Fc,IL}$ (data not shown). Thus one does not have to repeat measurements of I_{part} to evaluate I_{ET}, and can instead subtract the normalized theoretical

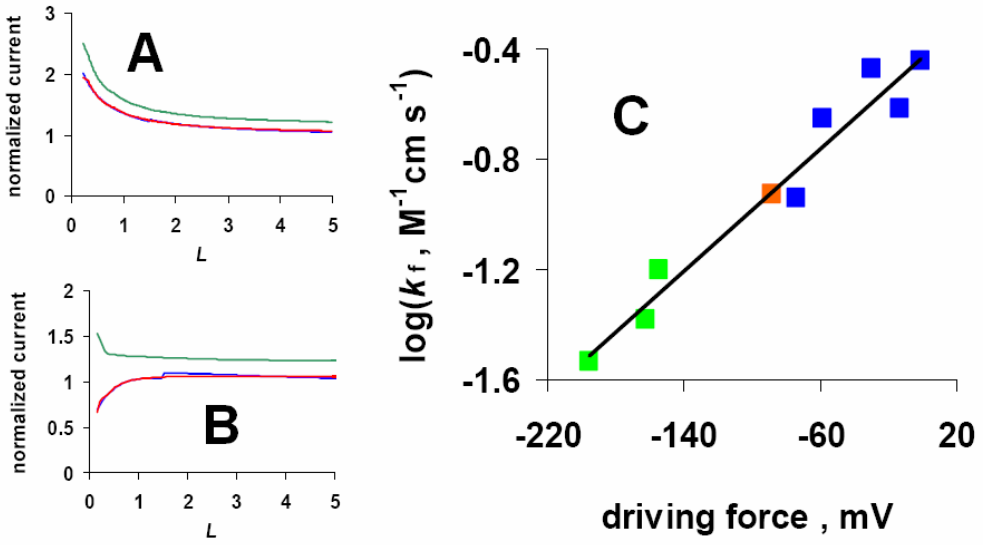

Figure 2.8. (A) and (B) current-distance dependences: I_T (green) and $I_{ET} = I_T - I_{part}$ (blue). Theoretical curves (red) [10a] were calculated for $k_f = 0.33$ $M^{-1}cm\ s^{-1}$ (A) and 0.048 M^{-1} cm s^{-1} (B). (C) Driving force dependence of the interfacial ET rate constant [6]. Green points were obtained with C_8mim^+, and blue points with $C_1C_1N^-$ common ion. The orange point was obtained without adding any common ion the aqueous phase, so that $[C_8mim^+] = [C_1C_1N^-]$. For other parameters, see Fig. 2.7.

approach curve (solid line in Fig.(2.6A)) from the experimental I_T vs. L dependence. In this way, the rate constant of reaction (2.2) was extracted from approach curves obtained at different $\Delta^{IL}_{w}\varphi$ (Fig. (2.8)). The subtraction yielded the I_{ET} vs. L curves, which fit very

well the SECM theory for finite heterogeneous kinetics at the substrate [10a] at any driving force value, from $\Delta E_{1/2}$ = -200 mV (the lower limit for the measurable rate constant) to $\Delta E_{1/2}$ = 20 mV (the highest value obtained using $C_1C_1N^-$ as a common ion). The driving force dependence of the bimolecular rate constant, $k_f = k$/ [Fc] (Fig. (2.8C)) is linear over the entire potential range (~220 mV). The slope of this dependence yields the transfer coefficient, α = 0.34. This number is consistent with the sharp interfacial boundary model [17], as one can expect because of the high intrinsic ionic strength and short Debye length in the IL phase.

Other ET Reactions at the IL/Water Interface.

To further investigate the kinetic behaviors discussed above and in ref. 6, we attempted to find other combinations of water- and IL-soluble redox couples that would not involve significant interfacial partitioning. A typical problem here is a relatively low solubility of many substances in ILs. Redox mediators like zinc porphyrin and tetracyanoquinodimethane, which have been successfully employed in ET studies at the water/DCE interface, are only sparingly soluble in $C_8mimC_1C_1N$.

We tried various combinations between three aqueous anionic mediators, $Fe(CN)_6^{3/4-}$, $Ru(CN)_6^{3/4-}$, and $IrCl_6^{3/2-}$which have previously been used in ET experiments at the water/organic interface [8], and several non-aqueous redox species. The latter included MPTZ, TTF, Rc, DcMRc, and three ferrocene derivatives, i.e., DEFc, BuFc, and DcMFc. MPTZ, TTF, Rc and DcMRc did not significantly partition to water, but showed only negative feedback in combination with all aqueous mediators. A translucent interfacial film could often be seen in several minutes after the beginning of the experiment. Apparently, a blocking film was formed by precipitation of the aqueous species with the products of the interfacial reaction and C_8mim^+.

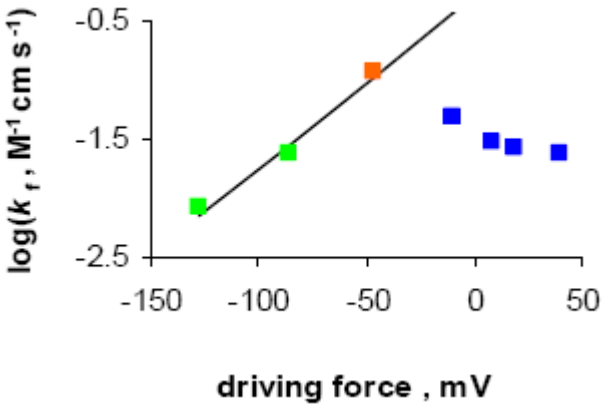

Figure 2.9. k_f vs. $\Delta E_{1/2}$ dependence for the ET between BuFc and ferricyanide at the IL/water interface. For parameters, see Fig. (2.7)

The electrochemical responses obtained using DEFc, BuFc, and DcMFc in combination with $Fe(CN)_6^{3/4-}$ were similar. The partitioning of these molecules to water is less significant than that of Fc (in case of DcMFc the partitioning is negligible). A portion of the driving force dependence obtained by changing of $[C_8mim^+]_w$ was linear, in agreement with conventional ET theory (green and orange dots in Figure (2.9)). However, when the increasing concentrations of $C_1C_1N^-$ were added to water, the feedback decreased non-linearly despite the increase in $\Delta E_{1/2}$ (blue dots in Fig. (2.9)). Although the surface film formation was not apparent in this case, some interfacial adsorption/precipitation reaction is a probable cause of these irregular responses.

2.4 Conclusions

High viscosities of ILs such as $C_8mimC_1C_1N$ necessitate the use of high concentrations of redox species in SECM studies of ET reactions at the IL/water interface. This, in turn, results in a more significant effect of the partitioning of redox species from IL to the aqueous phase on the tip current. It is surprisingly difficult to find a suitable combination of aqueous and non-aqueous redox mediators for ET studies.

Typical problems include low solubility of many redox species in IL, interfacial precipitation, and inexplicable electrochemical behavior. In this paper, we demonstrated that the contribution of partitioning can be quantitatively separated from the SECM feedback current produced by interfacial ET. This approach should be applicable to other two-phase systems providing that the homogeneous reaction between the aqueous redox mediator and non-aqueous redox species partitioning to water is negligibly slow.

The partition coefficient of redox species between IL and water can be determined from short-range SECM current-distance curves under quasi-steady-state conditions. The developed approach makes use of a big difference between the thicknesses of the diffusion layer of partitioning molecules formed at the macroscopic liquid/liquid interface and a much thinner diffusion layer at the SECM tip. The advantage of this method is that one does not have to wait for the complete solute equilibration. This is useful in the case of viscous ILs, where the complete equilibration may take a long time.

Chapter III

Shuttling Mechanism of Ion Transfer at the Water/Oil Interface

3.1 Introduction

The transfer of ions from water to organic phases is in most cases energetically unfavorable. This property is essential for many biological and technological systems. For example, living cell membranes, whose interior can be compared to hexadecane, [1] inhibit ion crossing [2] thus enabling selective transport through pores and ion channels [3]. In separation systems, the differences in energetics and kinetics of transfer across the liquid/liquid interface determine the efficiency of the extraction of a particular ionic species [4,5].

Ion transfer (IT) reactions at the water/organic solvent interface have been a subject for numerous experimental and theoretical studies [6-10]. Two substantially different classes of IT reactions are distinguished in the current literature: facilitated (or assisted) and simple (or unassisted) IT [6]. In the former case, organic solution contains a ligand (L) that can react with ion X to form a complex, XL (the stoichiometry of complexation can be different). Such a reaction can assist the transfer of an ion:

$$X^{n+}\,(aq) + L^{m-}\,(org) \rightleftarrows XL^{n-m}\,(org) \qquad (1)$$

Although facilitated IT of cations is more common, assisted transfers of anions have also been reported [11].

Simple IT processes are one-step reactions not involving any facilitating agent:

$$X^{n+}\,(aq) \rightleftarrows X^{n+}\,(org) \qquad (2)$$

This large group includes practically important transfers of metal cations, tetraalkylammonium ions, and various inorganic and organic anions. Among several contentious points in the theory of simple IT is the nature of its rate-limiting step. One model attributes the finite IT rate to slow diffusion of the transferred species through the interfacial layer [12,13], while another treatment considers activation-controlled change in ion solvation [9,10].

In most previous studies of IT at the liquid/liquid interface, the organic solution contained supporting electrolyte, i.e., a hydrophobic salt whose role was to increase the organic phase conductivity without directly participating in the interfacial reaction. A few experiments with no (or very little) electrolyte added either to aqueous or organic phase have been reported by us [14] and by other groups [15]. Recently, electrochemical measurements were carried out at the interface between an aqueous solution and a neat organic solvent formed at the tip of a nanopipette [14]. The transfer of an ion between the aqueous filling solution and the external organic phase was induced by applying voltage between the internal and external reference electrodes. In those experiments, alkali metal cations could not be transferred from water to less polar organic solvents containing no supporting electrolyte even at very high interfacial voltages (e.g., up to 9 V). This observation could not be explained either by low conductivity of the neat organic solvent or by slow charge transfer at the organic reference electrode because

relatively hydrophobic cations (e.g., tetraalkylammonium ions) were readily transferred from water to neat 1,2-dichlotoethane (DCE). Moreover, the addition of a very low concentration of organic supporting electrolyte induced the transfer of alkali metal cations to DCE. These findings are inconsistent with the generally accepted mechanism of simple IT reactions. Here we report IT experiments at the water/neat DCE interface for a wide class of hydrophilic ions including metal cations, protons and some anions. The transfer behavior of these species turned out to be similar to that of alkali metal cations. A model is proposed that can explain how these IT reactions are facilitated by hydrophobic counterions added to the organic phase.

The main technique employed in our experiments—nanopipette voltammetry—offers a powerful combination of the high mass-transfer rate and very straightforward data analysis with the negligibly small effects of the resistive potential drop and double layer charging current, which is essential for investigations of simple and facilitated IT reactions at the ITIES. The resistance of the pipettes filled with 0.1 M KCl solution was shown to be sufficiently low for the maximum *iR*-drop of <1 mV [16a]. The orifice radius, *a*, and the ratio of the glass wall radius to the orifice radius, RG, were verified by scanning electrochemical microscopy (SECM) and shown to be consistent with the values obtained from steady-state voltammetry [16b].

To obtain further information about the nature of ions transferred across the water/neat DCE interface, we carried out generation/collection experiments with θ–pipettes. A θ–pipette is a device, in which two closely spaced coplanar pipette orifices are separated by a thin line of glass [17,18]. One of two pipettes (generator) can be filled with an aqueous solution containing an ion of interest (e.g., a cation) and immersed in

DCE. When the generator pipette is biased at a sufficiently positive potential with respect to an external reference electrode, cations are expected to transfer from it to DCE. Some fraction of these ions will then diffuse to the orifice of the water-filled collector pipette (biased at a more negative potential) and transfer into it. The previously developed theory [17] allows one to verify that the generator current is produced by cation transfer from water to DCE rather than the transfer of some anionic species from DCE to the aqueous phase.

3.2 Experimental

Chemicals.

$MgCl_2$ from Fisher (Fair Lawn, NJ), HCl and $CaCl_2$ from J.T. Baker (Phillipsburg, NJ), tetrabutylammonium chloride, tetrahexylammonium chloride, potassium tetrakis [4-chlorophenyl]borate (KTPBCl), trimethylchlorosilane, LiCl, NaCl, NaOH, $Fe_2(SO_4)_3$, and KCl from Aldrich (Milwaukee, WI) were used as received. Tetrahexylammonium tetrakis [4-chlorophenyl]borate (THATPBCl) and tetrahexylammonium perchlorate were prepared as described previously [19]. All aqueous solutions were prepared from deionized water (Milli-Q, Millipore Corp.).

The high solvent purity was essential for IT experiments in the absence of organic supporting electrolyte. HPLC grade (99.8%) 1,2-dichloroethane was purchased from Sigma-Aldrich and distilled at least thrice before use. The distillation apparatus was washed by starting a distillation and discarding the first few mL of distillate. The distillation was performed until ~5% of DCE remained in the boiling flask. The

remainder was discarded each time prior to a new distillation. The triply distilled DCE was kept in a sealed container.

Preparation of Single-barrel Nanopipettes and θ-pipettes.

A Model P-2000 laser puller (Sutter Instrument Co.) was used to prepare the pipettes from capillaries, as described previously [16]. 1 mm outer diameter, 0.58 mm inner diameter quartz capillaries were used for regular pipette preparation, and borosilicate θ-tubing, OD = 1.5 mm (Sutter) was used to produce θ-pipettes. The aqueous solution was filled from the back using a 10-μL syringe, then, a 0.125-mm-radius Ag/AgCl wire was inserted in each pipette. The pipettes were checked using an Olympus BX-60 optical microscope prior to each measurement. The outer glass wall of the θ-pipette was silanized to prevent the formation of an aqueous film between the two orifices. This was done by dipping the pipette tip into trimethylchlorosilane for 1 - 2 min while the flow of argon (sufficiently fast to produce small bubbles) was passed through the pipette from the back to avoid silanization of the inner pipette wall. This was crucial because the outer organic solvent gets drawn inside a pipette if its inner surface is hydrophobic.

Instrumentation and Electrochemical Cells.

Nanopipette voltammograms were obtained using a BAS 100B electrochemical workstation (Bioanalytical Systems, West Lafayette, IN). Using an EI-400 bipotentiostat (Ensman Instruments, Bloomington, IN), the voltage was applied between the reference electrode inside each barrel of the θ-pipette and the reference electrode in the outer

solution. Voltammetric experiments were carried out in a 5-mL vial inside a Faraday cage.

Conductivity measurements were carried out in a Beckman conductivity cell with two Pt black parallel disk electrodes (5 cm^2, geometric area; 0.4 cm separation distance). Before measurements, the cell was washed with Milli-Q (Millipore) water and dried, then washed with HPLC grade DCE, and then rinsed with triple-distilled DCE. The resistance measurements over the range of frequencies from 10 Hz to 100 kHz were made using a home-built trans-impedance amplifier (R_{ampl} = 20 kΩ, 20 MHz bandwidth) and a SR-850 lock-in amplifier. An AC signal (100 mV_{rms}) was applied to the conductimetric cell, and the current returned via ground through the trans-impedance amplifier whose output was fed to the lock-in amplifier and filtered (time constant 1s).

3.3 Results and Discussion

Ion Transfer Voltammetry at the Water/neat DCE Interface.

Figure 1 shows steady-state voltammograms of various IT processes at the water/DCE interface formed at the tip of a nanopipette (a ~ 150 nm). As discussed earlier, Li^+ cannot be transferred to neat DCE at any experimentally achievable voltage (curve 1 in Fig. 3.1A). The addition of just 1 nM of tetrahexylammonium tetrakis(4-chlorophenyl)borate (THATPBCl) in Fig. 3.1A, curve 2 was sufficient to produce a well-defined IT wave of Li^+. On the other hand, the addition of a much higher concentration of a less hydrophobic counterion (e.g., 100 nM ClO_4^- in Fig. 3.1A, curve 3) did not result in any noticeable cation transfer. This indicates that the transfer of a hydrophilic cation is

made possible by interaction with a hydrophobic organic anion ($TPBCl^-$) rather than by the increase in concentration of ionic species in organic phase.

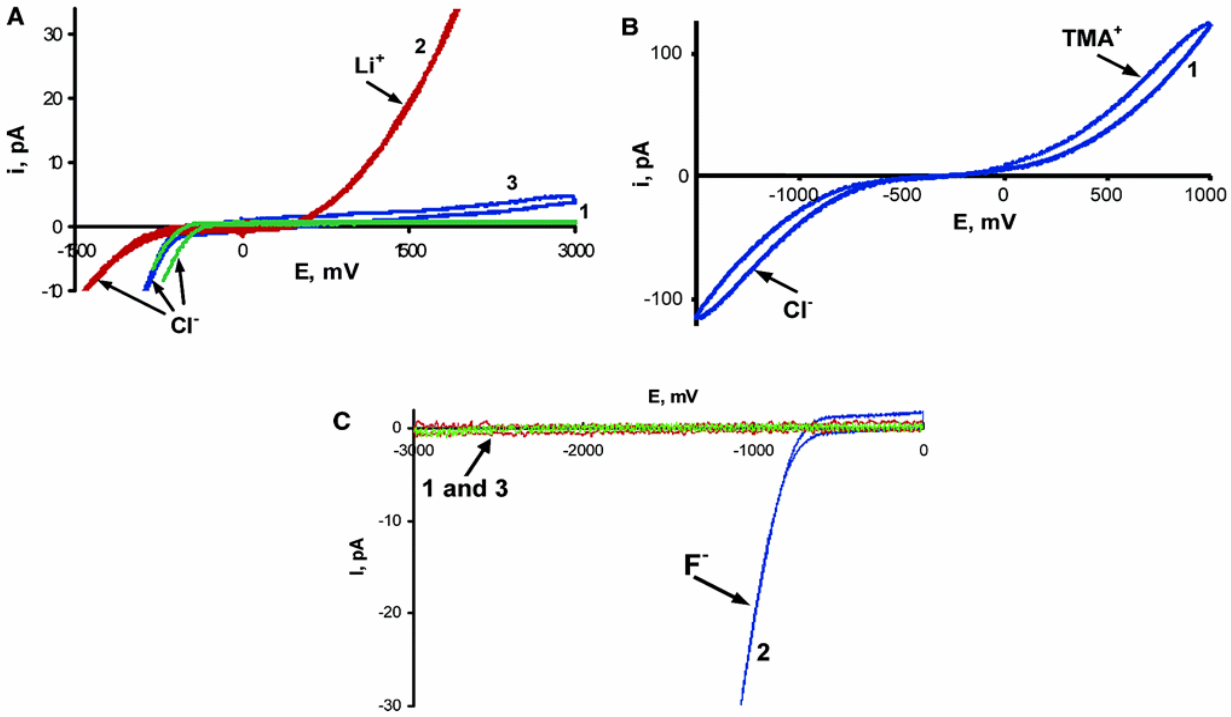

Figure. 3.1. Transfers of cations and anions from aqueous solution inside an ~150 nm nanopipette to external DCE solution. Filling solution was: (A) 0.1 M LiCl, (B) 0.1 M TMACl, and (C) 0.01 M LiF. DCE solution contained: (1) neat DCE; (2) 1 nM THATPBCl in A, or 100 nM THATPBCl in C; (3) 100 nM $TBAClO_4$ in A, or 100 nM KTPBCl in C.

The described phenomenon is quite general: all metal cations we have tested as well as protons could not be transferred to neat DCE (Figure 3.2A). Fluoride anion exhibits a very similar behavior: it cannot be transferred to neat DCE (curve 1 in Fig. 3.1C), and the transfer occurs in the presence of a very low concentration of a hydrophobic cation in DCE (e.g., THA^+, curve 2 in Fig. 3.1C). However, the same concentration of a hydrophilic cation (e.g., K^+, curve 3 in Fig. 3.1C) added to the organic

phase does not induce the transfer of F^-. The addition of tetrabutylammonium (TBA^+) cation, which is less hydrophobic than THA^+, to DCE resulted in a much lower current of F^- transfer (not shown).

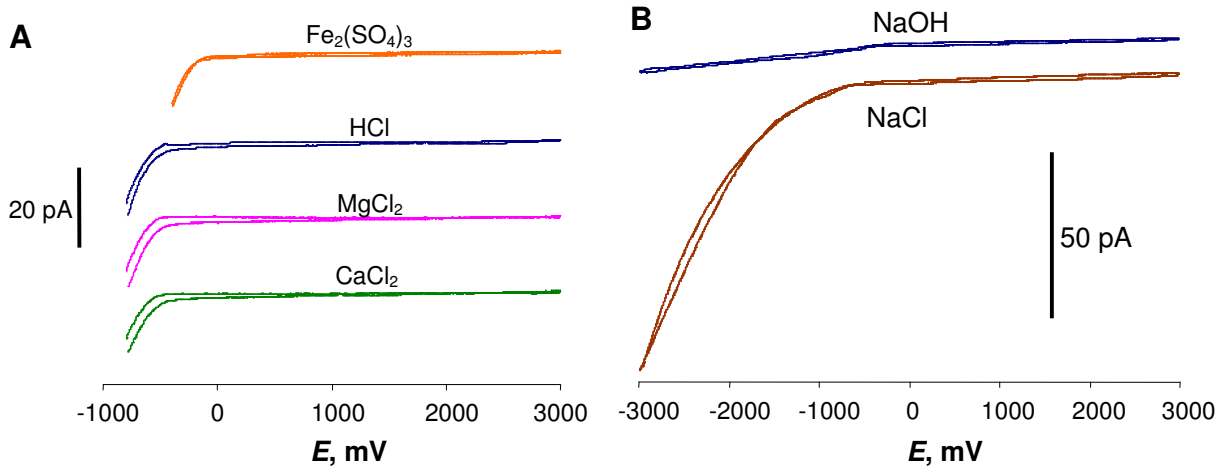

Figure. 3.2. IT voltammograms at the water/neat DCE interface. The transfers of Cl^- and SO_4^{2-} can be seen at negative potentials. The electrolyte concentrations in aqueous filling solutions were 100 mM (A) and 10 mM (B). The pipette radii were ~150 nm. The scan rate was 50 mV/s (A) and 20 mV/s (B). The voltammograms are shifted vertically for better clarity.

OH^- also does not transfer to neat DCE (Fig. 3.2B), but this reaction is harder to study because the products of glass dissolution in concentrated NaOH get transferred producing a small but measurable current. One should notice that other anions, e.g., Cl^- (Figs. 3.1A and 3.1B) and SO_4^{2-} (Figs. 3.2A), and relatively hydrophobic cations, e.g., tetraalkylammonium ions (Fig. 3.1B), readily transfer from water to neat DCE. Thus, the hindrance of transfers of more hydrophilic ions is not related either to low conductivity of neat DCE or to slow charge transfer at the organic reference electrode.

The transfer of a hydrophilic cation can be induced by adding an extremely low concentration of a hydrophobic anion to the organic phase. For example, only 50 pM of

THATPBCl was required to induce the IT of Ca^{2+} to DCE (Figure 3.3). From conductivity measurements (see Supporting Information), the effective concentration of ionic species in neat (triply distilled) DCE was found to be ~80 nM. Therefore, the addition of ≤1 nM THATPBCl to DCE could not appreciably change its conductivity.

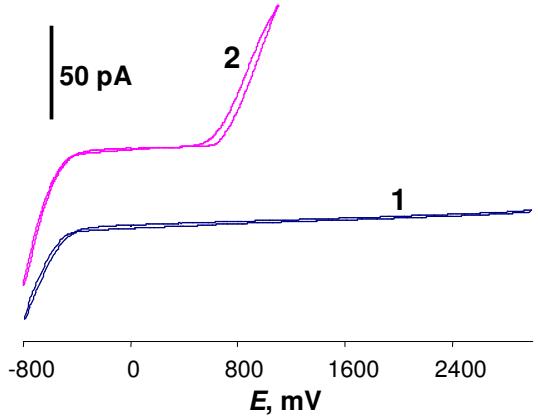

Figure. 3.3. Voltammograms of Ca^{2+} transfer. No transfer of Ca^{2+} occurs without supporting electrolyte in organic phase (curve 1). Ca^{2+} is transferred by adding 50 pM THATPBCl to neat DCE (curve 2). c_{CaCl_2} = 100 mM. $a \cong 150$ nm. The voltammograms are shifted vertically for better clarity.

Even with no electrolyte added, a diffuse double layer certainly exists on the organic side of the interface. Moreover, the effective ionic concentration in DCE near the liquid/liquid interface is probably higher than in the bulk due to the extraction of aqueous electrolyte [14]. The observed transfers of TMA^+, Cl^- across the water/neat DCE interface also indicate that the interfacial voltage can be established in the absence of added organic electrolyte.

Generation-Collection Experiments with θ–pipettes.

We used θ–pipettes to further investigate the effect of very low concentrations of organic supporting electrolyte on interfacial IT. Both capillaries of the θ–pipette (Fig. 3.4A) were filled with the same aqueous solution (e.g., 0.1 M LiCl), and it was immersed in DCE containing either no added electrolyte (Figs. 3.4B and 3.4C) or 1 μM THATPBCl (Figs. 3.4D – 3.4F).

When a sufficiently negative voltage was applied between the reference electrode inside the generator pipette and the external reference, Cl^- was transferred from the aqueous filling solution to neat DCE (curve 1 in Fig. 3.4B). Some fraction of chloride ions diffused to the orifice of the second (collector) pipette, which was biased at a more positive potential, and transferred into it. This processes produced the collector current (curve 2 in Fig.3.4B). In agreement with the previously developed theory [17], Fig. 3.4C shows that the collection efficiency (i_c/i_g) of Cl^- was essentially independent of the generator potential (E_g) and increased with the increasingly positive value of collector potential (E_c). The results obtained in the presence of 1 μM THATPBCl (Figs. 3.4D and 3.4E) are very similar, except that the IT of Cl^- occurred at slightly less negative voltages. In contrast, the curves obtained for the transfer of Li^+ with and without organic supporting electrolyte are strikingly different. In the former case, the generator and collector voltammograms (curves 1 and 2 in Fig. 3.4D at positive E_g) as well as the i_c/i_g dependences vs. E_g and E_c (Figs 4F) are in agreement with conventional theory [17]. Essentially flat generator and collector voltammograms (curves 1 and 2 at positive E_g) in Fig. 3.4B confirm that no Li^+ transfer occurs in the absence of $TPBCl^-$.

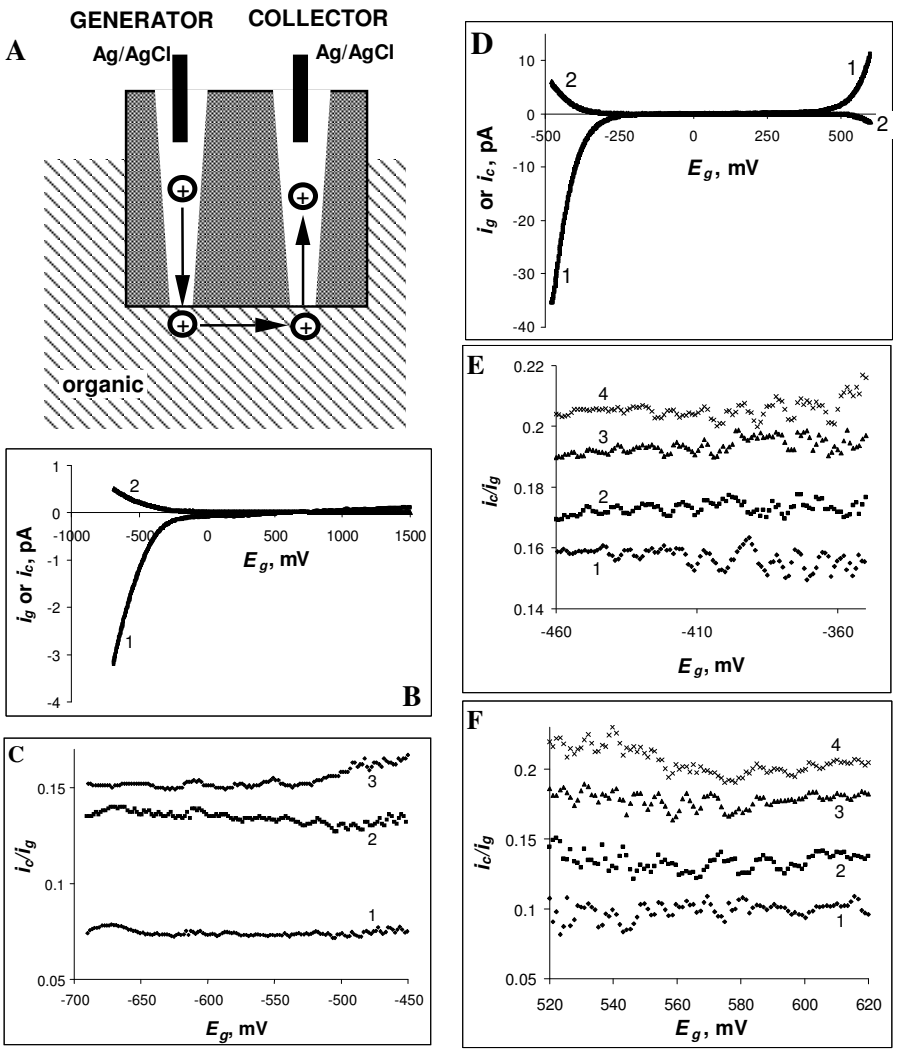

Figure. 3.4. Probing IT with a θ-pipette. (A) Schematic representation of cation transfer from the generator pipette to the external solution and then to the collector pipette. (B) and (D) Dependencies of the generator (i_g; curve 1) and collector (i_c; curve 2) currents on generator potential (E_g). (C), (E), and (F) Dependencies of collection efficiency (i_c/i_g) on E_g for the transfers of Li^+ (F) and Cl^- (C and E) between water and DCE. Collector potential (E_c, mV) was (B) 500; (C) from curve 1 to curve 3: 0, 500, and 1000; (D) -200; (E) from curve 1 to curve 4: -200, 0, 200, and 400; and (F) from curve 1 to curve 4: 400, 200, 0, and -200. DCE contained no added electrolyte (B, C) or 1 μm THATPBCl (D – F). The generator and collector radii were 420 nm each (B, C) or 680 nm each (D – F).

Shuttling Model of IT.

The above data suggest that the transfers of hydrophilic cations and anions to organic solvents have to be facilitated by hydrophobic organic counterions. The mechanism of these reactions is, however, completely different from that of conventional facilitated IT (Eq. 1). Unlike transition metals [20] alkali metal ions and protons do not form stable complexes with organic anions. Moreover, nanomolar counterion concentrations are too low to produce measurable facilitated IT current. In case of conventional facilitated IT (reaction 1), the diffusion limiting current (i_d) must be proportional to the concentration of the facilitating agent (c_L) as long as it is smaller than the concentration of the ion of interest in water (c_{X+}) [21]

$$i_d = 3.35\pi nFaD_Lc_L \quad (3)$$

where F is the Faraday constant, D_L is the diffusion coefficient of L in DCE, a is the pipette radius, and n is the charge of the transferred ion. According to Eq. (3), the diffusion limiting current corresponding to a = 150 nm and c_L = 1 nM would be ~10^{-15} A, i.e., four orders of magnitude lower than the current in curve 2 (Fig. 3.1A). To further prove this point, we carried out constant-potential electrolysis of Li^+ transfer from a ~150-nm-radius pipette into 1.5 mL of DCE containing 10 nM THATPBCl. The current was almost constant during 120 min of electrolysis, and the amount of Li^+ transferred (36 pmol) was more than twice the amount of $TPBCl^-$ dissolved in DCE (15 pmol). Therefore, the observed effect cannot be explained by a conventional facilitation mechanism (Eq. (1)) that involves the formation of a stable XL species.

Figure 5 shows the scheme of the shuttling mechanism that explains how a miniscule amount of a hydrophobic counterion can produce measurable IT current. (The process in Fig. 3.5 is cation transfer, but the extension of this model to anion transfer is straightforward.)

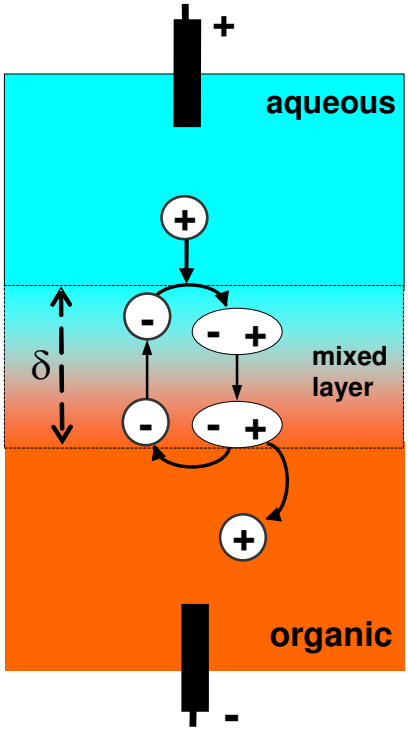

Figure. 3.5. Scheme of the shuttling mechanism of IT. Transfer of a cation from water to organic phase involves the formation of a short-lived ion pair with a hydrophobic anion.

The aqueous and organic phases in Fig. 3.5 are separated by ~1 nm-thick mixed solvent layer [6,22]. An ion pair (⊖⊕) formed by a hydrophilic cation (⊕) and a hydrophobic organic anion (⊖) at the outer boundary of the aqueous phase diffuses across the mixed solvent layer towards the organic phase and dissociates. The released

cation is driven into the bulk of the organic phase by the electric field, while the anion travels (via diffusion/migration) across the mixed solvent layer and assists the transfer of the next cation. Besides the interfacial voltage, which carries the cation and the anion in opposite directions, the shuttling process is driven by the gradient of the cation concentration across the mixed layer, which is high (e.g., c_{X+}= 0.1 M) on the aqueous side of the interface and low on the organic side.

Determination of the Ion Association Constant of KTPBCl in DCE.

To quantitatively describe the formation and decomposition of an ion pair, one needs to know the value of the ion association constant

$$K_A = \frac{c_{pair}}{c_{X^+} c_{-}} \tag{4}$$

where c_{pair} and c_{-} are the concentrations of the ion pair and the hydrophobic counterion, respectively. Although interfacial ion pairing has been studied [23], the association constants for this process are difficult to measure. We carried out conductimetric experiments to determine the association constant for K^+ and $TPBCl^-$ in DCE. This value can be used as a rough approximation for the interfacial association constant, which may actually be somewhat smaller because the polarity of the interfacial region is the arithmetic average of the polarities of water and DCE [24]. A saturated solution of potassium tetrakis(4-chlorophenyl)borate in DCE was prepared and allowed to equilibrate with solid KTPBCl overnight. Conductivity measurements (see Supporting

Information) were made by diluting the filtered stock solution with pure triply distilled DCE. The dilution shifted the equilibrium (5) to the left

$$K^+ + TPBCl^- \overset{K_A}{\rightleftarrows} K^+TPBCl^- \tag{5}$$

The combination of the mass action expression for reaction (5) with the electroneutrality and conservation of mass equations gives

$$[K^+] = [TPBCl^-] = \frac{\sqrt{1+4K_A c_{KTPBCl}} - 1}{2K_A} \tag{6}$$

where K_A is the association constant and c_{KTPBCl} is the total concentration of dissolved salt at the given dilution. Since the solution conductance, L, is proportional to the concentration of dissociated salt in solution,

$$\frac{L}{L_0} = \frac{\sqrt{1+4K_A c_{KTPBCl}} - 1}{\sqrt{1+4K_A c_0} - 1} \tag{7}$$

where L_0 = 24.3 μS is the conductance and c_0 = 73 μM is the concentration of salt in the saturated solution before dilution. The fit of the experimental data to Eq. (7) shown in Figure 3.6 yields the association constant for K^+TPBCl^-, $K_A = 2.1 \times 10^4$ M^{-1}.

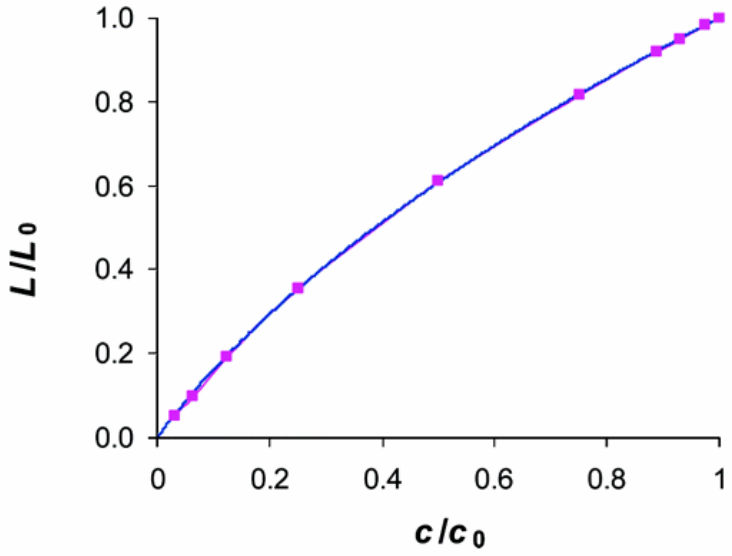

Figure. 3.6. Experimental (squares) and theoretical (solid line) dependences of DCE solution conductivity on KTPBCl concentration.

For the aqueous side of the interface, where c_{X+} = 0.1 M, one obtains from Eq. (4)

$$\frac{c_{pair}}{c_{-}} = K_A c_{X^+} \cong 2000 \tag{8}$$

Eq. (8) indicates that nearly all $TPBCl^-$ ions reaching the aqueous side of the interface get paired with K^+. On the organic side of the interface, the low cation and anion concentrations result in decomposition of an ion pair. Assuming c_- = 100 nM,

$$\frac{c_{X^+}}{c_{pair}} = 1/K_A c_{-} \cong 5 \cdot 10^3 \tag{9}$$

i.e., practically all ion pairs dissociate releasing K^+ and $TPBCl^-$ ions.

The rate of Ion Shuttling.

The mass transfer rate for the ion shuttling mechanism is determined by the transport of the counterions and/or ion pairs across the mixed solvent layer. The counterion transport, which is accelerated by the interfacial voltage, should be faster than the diffusion of neutral ion pairs. Since almost all counterions reaching the aqueous phase get ion-paired (cf. Eq. (8)), the steady-state diffusion current across the mixed solvent layer can be expressed as

$$i = \pi a^2 n F D_{pair} c_-^s / \delta \qquad (10)$$

where D_{pair} is the diffusion coefficient of an ion pair, c_-^s is the counterion concentration in organic phase near the phase boundary, and $\delta \sim 1$ nm is the thickness of the mixed solvent layer. From Eq. (10) one can see that the c_-^s value has to be ~3 orders of magnitude higher than the 1 nM bulk concentration of $TPBCl^-$ to support the current measured in Fig. 3.1A (curve 2). An accumulation of this magnitude can be expected from both the classical Gouy-Chapman theory [6] and the recent molecular dynamics simulations [25] since the major portion of the interfacial potential drop (several hundred mV) occurs within the thick diffuse layer in DCE. The shuttling mechanism could not be deduced from the published experimental data obtained with the excess supporting electrolyte in organic phase, where the ion shuttling process was rapid and did not limit the overall IT rate.

The above model predicts that the rate of ion shuttling should be proportional to the interfacial area in contrast to the direct proportionality between the steady-state diffusion current and the pipette radius expected from the conventional IT theory (cf. Eqs. (3) and (10)). The experimental verification of this prediction is shown in Figure 3.7. Each line in Fig. 3.7 has a non-zero intercept, whose value increases with increasing *E*. This behavior can be attributed to the combination of the charging current, small current of organic ion transfer, reference potential instability, and other experimental issues.

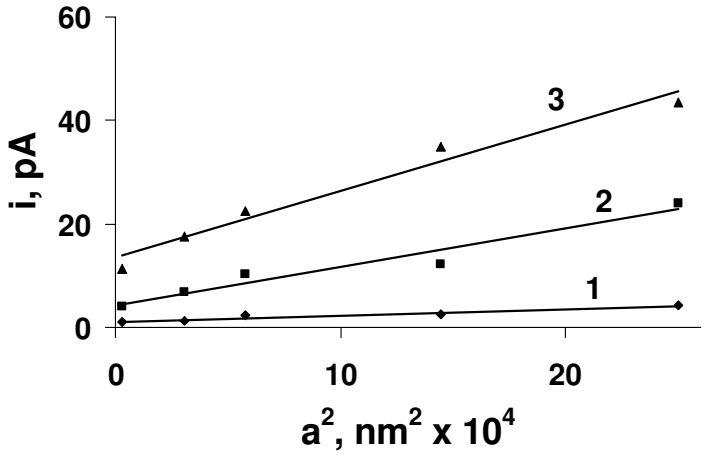

Figure. 3.7. Dependences of Li^+ transfer current on the square of the pipette radius at different interfacial voltages. *E*, mV = 350 (1), 400 (2), and 450 (3). DCE contained 2 μM THATPBCl. For other parameters, see Fig. 3.1A.

The developed model also explains why only hydrophobic counterions can facilitate IT reactions. An aqueous ion is not expected to form an ion pair with a hydrophilic counterion. Moreover, if such a pair were to form, it would be too hydrophilic to partition to the organic phase. The observed differences in transfer behaviors of two groups of ions (i.e., metal cations, protons, fluoride and hydroxide vs.

tetraalkylammonium cations and moderately hydrophilic anions) cannot be attributed to different energetics of those processes. For example, the Gibbs free energy of Cl^- transfer to DCE (51 kJ/mol) is within the range of free energies of K^+, Na^+, and Li^+ transfers (50 to 57 kJ/mol). [26] The sharp contrast between the transfer of Cl^- to neat DCE at moderate interfacial voltages and the very strong hindrance of metal cation transfers points to very slow kinetics of the latter processes. Apparently, the group of IT reactions that do not require the presence of a hydrophobic counterion in organic phase are low-barrier processes whose rates are determined either by interfacial diffusion/migration alone [12,13] or in combination with interfacial protrusions. [10,27] In contrast, high-barrier IT reactions do not proceed without a facilitating agent. Since most of the applied voltage drops within a thick diffuse layer in organic phase, [9,28] the fraction of voltage dropping across the interfacial boundary may actually be too small to cross a high barrier.

3.4 Conclusion

Two types of ion transfer behavior were observed in our experiments at liquid/liquid nano-interfaces: while a number of ions can be transferred from water to neat organic solvents, the transfers of a wide class of hydrophilic ions (e.g., metal cations, protons and some anions) must be facilitated by hydrophobic organic counterions. This finding contradicts the generally accepted notion of those IT reactions as unassisted, one-step processes. A new shuttling mechanism is proposed to describe this class of IT reactions. It involves the formation of a short-lived ion pair at the interface and shuttling of a hydrophilic ion across the mixed solvent layer. Although the concept of ion shuttling across membranes is well known, it has never been applied to liquid/liquid interfaces.

This model explains how a tiny amount of hydrophobic counterions (e.g., <1 nM) can be sufficient to induce measurable IT current. The transfer reactions requiring facilitation by hydrophobic counterions may represent the case of high-barrier, activation-controlled IT [9,10], while the transfers occurring with no organic counterion can be seen as low-barrier, diffusion-controlled IT processes [12,13].

Chapter IV

Role of Trace Amounts of Water in the Transfers of Hydrophilic and Hydrophobic Ions to Low Polarity Organic Solvents

4.1 Introduction

A detailed knowledge of ion transfer (IT) mechanisms between water and low polarity media is crucial for many areas of chemistry and biochemistry such as phase transfer catalysis, separations, and biomembranes [1,2]. Recent theoretical and experimental studies and molecular dynamics simulations of IT at the interface between two immiscible electrolyte solutions (ITIES) [3-12] and water/lipid membrane interface [13-15] improved our understanding of thermodynamics, kinetics and ion distribution at the phase boundary in these systems. IT experiments at nanometer-sized ITIES [16] revealed mechanistic differences between the transfers of relatively hydrophobic and strongly hydrophilic ions: the former can be viewed as unassisted, one-step reactions, while the latter processes must be facilitated by hydrophobic counterions present in organic phase (shuttling mechanism [16b]). Here we show another important mechanistic difference between the two classes of ITs: relatively hydrophobic ions are transferred into neat organic solvents (e.g., 1,2-dichloroethane, DCE), but hydrophilic ions can only be transferred to water clusters dispersed in organic phase.

4.2 Result and Discussion

Cyclic voltammograms (CVs) of alkali metal ions and tetramethylammonium cation transfers (Fig. 4.1) were obtained using a nanopipette filled with 0.1 M XCl (X^+ = Li^+, Na^+, Cs^+ or TMA^+) aqueous solution and immersed in DCE containing no

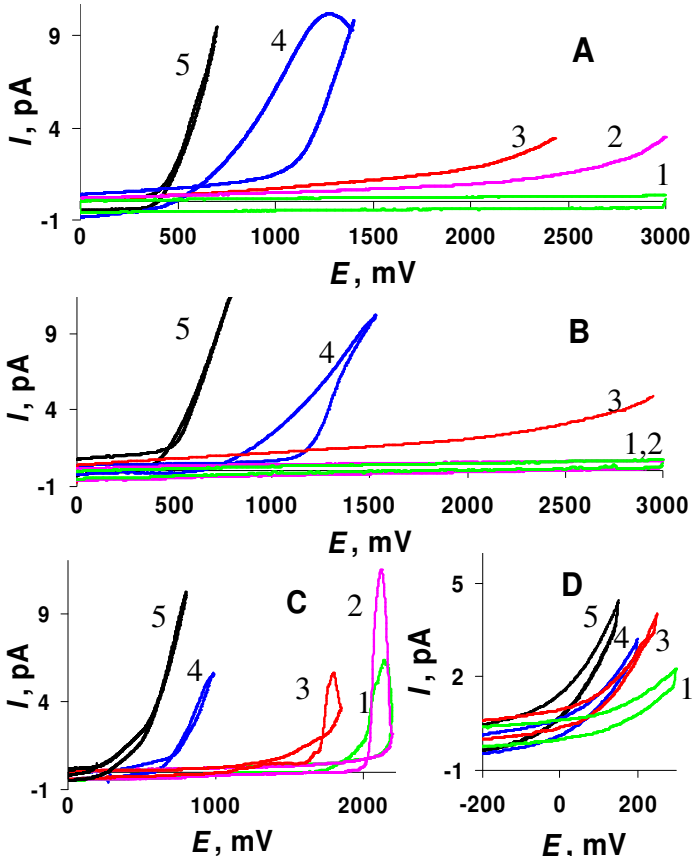

Figure. 4.1. Voltammograms of Li^+ (A), Na^+ (B), Cs^+ (C), and TMA^+ (D) transfers from water to DCE containing the following amounts of water: 130 mM H_2O (5), 13 mM (4), 1.3 mM (3), 130 μM (2), and 0 (1). The radius of nanopipette orifice was ~150 nm. The potential scan rate was 50 mV/s.

added electrolyte [17]. With no water added to neat DCE, no current of Li^+ or Na^+ transfer can be seen in Figs. 4.1A and 4.1B (green curves) at any interfacial voltage (E) up to E = 3 V. In contrast, all alkali metal ions (the data for K^+ is not shown) readily transferred to water-saturated DCE (black curves in Figs. 4.1A and 4.1B; the concentration of water, ~0.13 M at 25 °C [18]). These ions could also be transferred to DCE containing much less water (e.g., 130 μM; pink curve in Fig. 4.1A). The same trend can be seen in Figs. 4.1A and 4.1B: the higher the water concentration the lower the interfacial voltage required to drive the IT reaction [19].

Somewhat less hydrophilic Cs^+ ions could be transferred to neat DCE with no added water at $E \geq 2V$ (green curve in Fig. 4.1C). This process is greatly facilitated by addition of water. In contrast, much less hydrophilic tetramethylammonium (TMA^+) ions readily transfer to neat DCE at low interfacial voltages, and the effect of water concentration in DCE on this process is small (Fig. 4.1D). Since only strongly hydrophobic organic counterions (e.g., tetrakis(4-chlorophenyl)borate) can assist the transfers of metal cations to neat organic solvents [16], the facilitation of this reactions by added water cannot be explained by its ionization in DCE.

The effect of added water on conductivity of DCE can be seen from admittance versus frequency curves (Fig. 4.2). The conductivity of neat (i.e., triply distilled) DCE corresponds to an effective concentration of ionic impurities ~80 nM [16b]. In Fig. 4.2, the admittance at high frequencies is determined by the cell capacitance. It is proportional to the frequency of excitation and independent of water concentration in DCE. In the low-frequency plateau region, the cell admittance is essentially equal to the solution conductance. Surprisingly, the conductance decreases with increasing concentration of water in DCE. The conductivity of water-saturated DCE (orange curve in Fig. 4.2) is five times lower than that of essentially dry DCE (green curve). The linear plot of conductance vs. $\log([H_2O])$ is shown in Fig. 4.2 (inset).

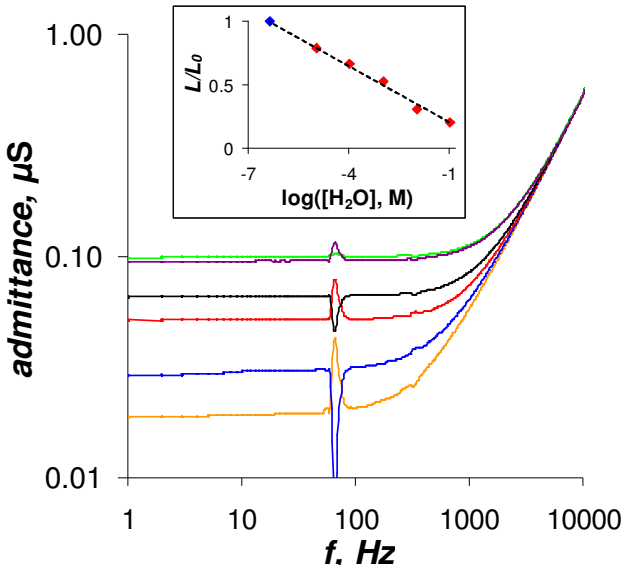

Figure 4.2. Frequency dependences of the conductimetric cell admittance for different concentrations of water in DCE and a plot of normalized conductance (L/L_0) versus water concentration in DCE (inset). L_0 is the conductance of the cell filled with neat DCE. A spike at f = 60 Hz is an instrumental artifact. The blue point in the inset was obtained by extrapolation of the experimental plot to the conductance of neat DCE (L_0 = 95 nS). The concentration of water added to DCE (from bottom to top), mM: 130, 13, 1.3, 0.13, 0.013, and 0.

A significant variation in solution conductivity is due to the change either in viscosity or in the total concentration of charges. Since the addition of 0.1 mM of water could not have caused a major increase in DCE viscosity, the data in Fig. 4.2 suggests that the effective concentration of charges in DCE decreases significantly with increasing [H_2O]. This effect cannot be attributed to the extraction of ionic impurities from DCE during its equilibration with water because only a small fraction of water-saturated DCE was used to prepare most solutions in Fig. 4.2 (e.g., 0.1% of the total solution volume for the black curve).

The diminished effective concentration of charges in water-equilibrated DCE can be attributed to the formation of water clusters into which the ionic species are extracted.

The existence of such clusters in nitrobenzene and their role in solvation of ions were revealed by NMR studies [21]. DCE is less polar and less miscible with water than nitrobenzene, and so even more extensive extraction of ions from DCE to water clusters dispersed in it can be expected.

A strong catalytic effect of trace amounts of water on IT suggests that hydrophilic metal ions (and protons; see Supporting Information) are actually transferred to water clusters dispersed in DCE rather than to the bulk organic solvent. Although the detailed mechanism of such a transfer has yet to be elucidated, it probably occurs when an aqueous cluster comes close to the phase boundary and interacts with a water "finger" that forms during the IT reaction [11]. Although water molecules continuously egress from the pipette to neat DCE, they diffuse rapidly from the nano-interface into bulk DCE and therefore cannot induce IT processes. This model explains why the transfers of strongly hydrophilic metal ions to water-saturated DCE occur at modest interfacial voltages.

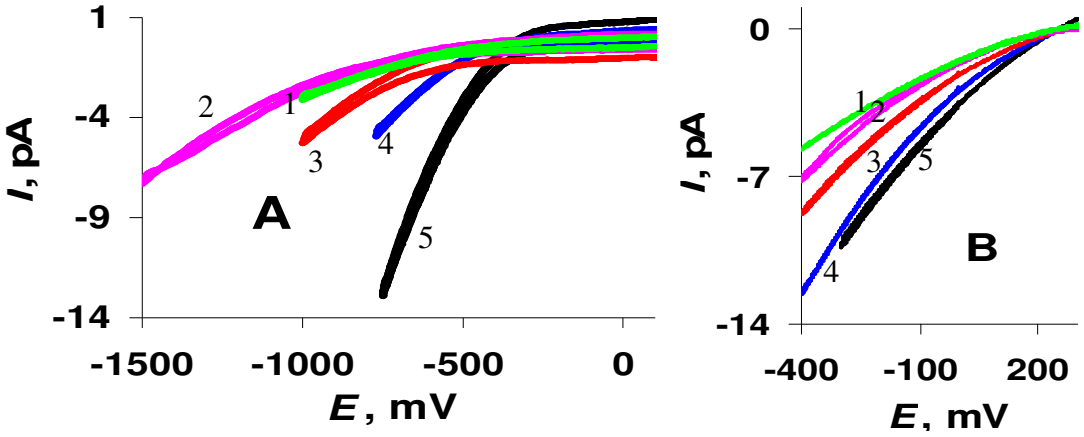

Figure 4.3. Voltammograms of Cl^- (A) and TPB^- (B) transfers from water to DCE containing the following amounts of water: 130 mM H_2O (5), 13 mM (4), 1.3 mM (3), 130 μM (2), and 0 (1). The radius of nanopipette orifice was ~150 nm. Aqueous solution contained 0.1 M NaCl (A) or NaTPB (B).

It is also clear that the behavior of more hydrophobic cations (e.g., TMA^+), which can be readily transferred to neat DCE, is almost unaffected by [H_2O] in organic phase. The transfers of anions (Fig. 4.3) exhibit similar trends. Relatively hydrophilic Cl^- can be transferred to neat DCE only at high negative voltages (Fig. 4.3A). Although the effect of water addition on this process is less pronounced than it is for more strongly hydrated Li^+ and Na^+, the shift of the Cl^- wave between the green (neat DCE) and black (water-saturated DCE) curves is ~1V. In contrast, the onset of transfer of hydrophobic tetraphenylborate (TPB^-; Fig. 4.3B) is almost independent of [H_2O] in DCE.

4.3 Conclusion

In summary, our results point to significant mechanistic differences between the transfers of hydrophilic and hydrophobic ions to low polarity solvents. Hydrophobic ions undergo simple transfers from water to the organic solvents. Such reactions do not require the presence of organic electrolyte [16], and they are essentially unaffected by concentration of water in organic solvent. In contrast, strongly hydrophilic ions are transferred from the aqueous phase to water clusters dispersed in organic phase. Therefore, the more hydrophilic the ion the more significant the increase in its transfer rate with increasing concentration of water in organic phase. The reported results may be relevant to passive ion permeation through biomembranes [13,14].

Chapter V

Electrochemical Attosyringe

5.1 Introduction

Many biologically important molecules, such as DNA and proteins, cannot cross the cell membrane. Microinjection techniques are widely used in cell biology when one needs to introduce such substances into the cytoplasm of living cells [1]. Important advantages of microinjection over other techniques, such as lipofection [2] and electroporation [3], include the possibilities to target specific cells and to inject practically any material into the cell with some degree of spatial selectivity [4].

The most common mode of microinjection is "stab injection", where a micropipette rapidly perforates the cell membrane, injects some amount of material and withdraws. However, it is difficult to control either the location of the pipette tip during the stab injection or the amount of the injected material [5]. These problems, along with a relatively large pipette tip size (usually, micrometers) and high volume of the injected solution, often cause damage to cells and dramatically decrease the injection success rate [6]. The above limitations, which are common to pressure microinjectors, are largely due to the difficulty in using high pressures to move liquid through a submicrometer-sized pipette orifice. Some novel approaches were used recently to overcome this problem. For example, Knoblauch *et al.* [6] introduced an injector based on the temperature expansion of a liquid alloy. However, controlling the amount of heat delivered to the alloy during the injection and the dispensed volume may not be straightforward especially in the case of multiple injections. Among other recently reported devices are an electroosmosis-based nanopipettor that can deliver pL-range volumes [7], a cell

nanoinjector, in which cargo is delivered by a carbon nanotube used as an AFM tip [8], and a double-barrel nanopipette for depositing liquid drops on a surface [9].

In this Chapter, we describe a new device for cellular injections—an "electrochemical attosyringe." The device consists of a nanopipette that is produced by heat-pulling a capillary and separating it into two halves, each of which is shaped as a needle. The radius of the pipette orifice depends of the choice of pulling parameters and can be varied from a few nanometers to >1 μm. The prepared nanopipette is filled with a water-immiscible organic solvent and immersed in an aqueous solution (Fig. 5.1).

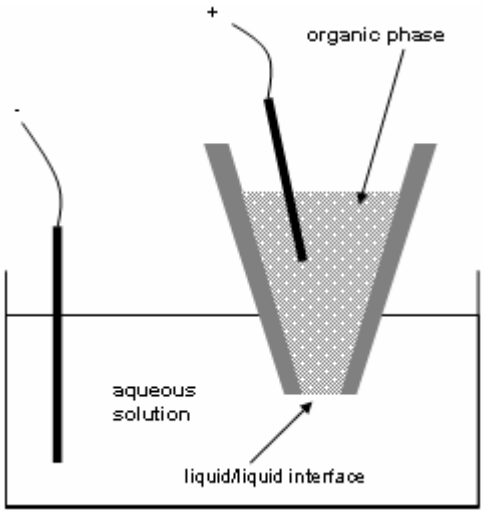

Figure. 5.1. Scheme of the electrochemical attosyringe.

The potential drop between the two liquid phases can be controlled by applying voltage between the reference electrode inserted in the pipette and another reference electrode immersed in the outer solution. It is well known that the application of voltage across the liquid/liquid interface changes the surface tension [10]. We discovered recently that the resulting force is sufficiently strong to induce the flow of liquid into/out of the pipette. When the potential of the inner (organic) solution is made negative, the shape of the meniscus at the interface of the two liquids changes, and water enters the pipette. The application of a sufficiently positive potential to the inner reference

electrode results in the expulsion of water. Here we make use of this effect to deliver ultra-small volumes of solution into mammalian cells in culture.

5.2 Material and Methods

Nanopipette Preparation.

A Model P-2000 laser puller from Sutter Instrument Co. (Novato, CA) was used to prepare nanopipettes from borosilicate glass capillaries (OD = 1mm, ID = 0.58 mm), as described previously [11,12]. To draw/dispense aqueous solutions, a nanopipette was filled from the back with a 10 mM solution of tetrahexylammonium tetrakis(4-chlorophenyl)borate (THATPBCl) in 1,2-dichloroethane (DCE) using a 10-µL syringe. To deliver organic solutions, the pipette was filled with a 100 mM aqueous $MgSO_4$. A 0.2-mm Ag wire coated with either AgTPBCl or Ag/AgCl was inserted in each pipette.

Instrumentation and Procedures.

The sequences of voltage steps for egress/ingress experiments were computer-generated with the homewritten software. For the current vs. voltage measurements, a linear voltage ramp was applied to the syringe using an EI-400 bipotentiostat (Cypress Systems, Chemlsford, MA) which was also used to monitor the current flowing across the liquid/liquid interface. Experiments not involving living cells were performed in quartz cuvettes under long-distance video microscopic control (Thales Optem, Fairport, NY). The scanning electrochemical microscope (SECM) [13] was homebuilt. In injection experiments, the nanopipette was attached as a probe to the 3D stage of the SECM, and the Petri dish in which a monolayer of cells was immersed in the buffer solution was mounted on the horizontal stage of an Axiovert-100 inverted fluorescence microscope (Zeiss). A video camera (IK – TU40A, Toshiba) was attached to the microscope to capture optical and fluorescence images. The SECM was set on the same optical table as the microscope so that the pipette could be positioned above the cell

culture plate. A 0.2-mm Ag/AgCl electrode was immersed in the buffer solution and used as an external reference.

Cells and Reagents.

Mid-passage MCF-10A cells, a human breast epithelial cell line, were cultured in DMEM/F12 media (1:1) supplemented with 5% equine serum, insulin (10 µg/ml), epidermal growth factor (20 ng/ml), cholera toxin (100 ng/ml), and hydrocortisone (0.5 µg/ml) and maintained with penicillin (100 units/ml), streptomycin (100 µg/ml), and fungizone (0.5 µg/ml). Cells were redistributed at 1:3 to 1:6 every 3 to 4 days. Cells were plated at 5-20% confluence (2-8 x 10^3 cells/60-mm plate) on the day before the experiment. Prior to each experiment, the culture medium was rinsed with a buffer containing 130 mM sucrose, 15 mM potassium chloride, 18 mM potassium acetate, 10 mM magnesium acetate, 500 µM calcium chloride and 10 mM HEPES. All aqueous solutions were prepared from deionized water (Milli-Q, Millipore Corp., Billerica, MA). Culture media, serum, and antibiotics (fungizone, penicillin, streptomycin) were purchased from Invitrogen Corp. (Rockville, MD). Ethidium bromide (EB) from Calbiochem (San Diego, CA) was used as received. A stock solution of 10 mM EB in water was made and kept on the shelf for no more than two weeks. BODIPY®-FLATP was purchased from Invitrogen Corp. (Eugene, OR) and kept at -18 °C between experiments.

Dye Injection and Imaging.

The pipette tip was brought near the cell and the medium was flushed and replaced with a sucrose buffer solution containing either EB or BODIPY® FLAP fluorescent dye. The voltage applied to the syringe was stepped to -200 mV to load the nanopipette with the aqueous solution. After the desired solution volume entered the nanopipette, the voltage was changed to +400 mV to stop the ingress. Then, the voltage

was raised again to +700 mV, at which the sucrose solution was completely expelled from the syringe. This sequence was repeated several times prior to cell injection to verify the consistency of the syringe operation.

Using a piezo actuator of the SECM instrument, the nanopipette was moved towards the cell until its tip punctured the membrane. The voltage applied to the syringe was raised to +700 mV, at which the sucrose solution was injected inside the cell. Care was taken not to eject all aqueous solution from the pipette in order to prevent the direct contact of the cell membrane with DCE. The pipette was withdrawn and moved to the next cell. The injection procedure was repeated. To obtain a fluorescence image, the medium was rinsed several times with a buffer solution containing no dye, and then a picture was taken under UV illumination.

5.3 Results

Sampling and Dispensing Fluids with the Attosyringe.

The potential control of the fluid injection/ejection is shown in Fig. 5.2. The five panels of Fig. 5.2 were obtained with a video microscope (~1000x) focused on the tip of a nanopipette filled with DCE solution. In Fig. 5.2a, the interfacial voltage (*E*) was maintained at +600 mV (organic phase positive) to prevent the ingress of water inside the pipette. When the voltage was lowered to -100 mV, the aqueous solution immediately flowed inside the pipette. This flow was stopped by stepping the organic phase potential to ca. +90 mV (Fig. 5.2b). The volume of aqueous solution inside the pipette remained constant as long as the potential was held at +90 mV. When the potential was stepped back to ca. +600 mV, aqueous solution was completely removed from the pipette (Fig. 5.2c). This injection/ejection process could be performed repeatedly with the same nanopipette, as shown in Figs. 5.2d and 5.2e.

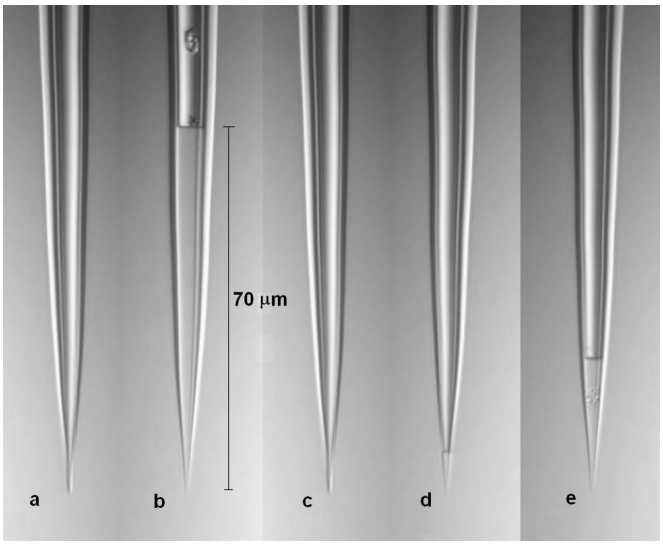

Figure. 5.2. Sequential ingress/egress of water in a DCE-filled nanopipette (a) initial immersion, E = +600 mV; (b) ingress of water after the voltage was stepped to -100 mV an then to +90 mV; (c) complete egress of water at E = +600 mV; (d) same as (b) but with a shorter step time at E = -100 mV; (e) the voltage was stepped again to -100 mV and then back to +90 mV. The aperture radius was ~300 nm. The pipette was filled with 10 mM THATPBCl in DCE and immersed in 10 mM KF aqueous solution.

In a very similar way, one can fill the pipette with water and immerse it in a water-immiscible liquid (e.g., organic solvent). This arrangement, which enables the injection/ejection of liquids other than water, is potentially useful, e.g., for nanolithography and sample injection in capillary electrophoresis and automated analysis systems.

The volume of injected solution depends strongly on the pipette radius, the duration of the potential step and its amplitude. For the sake of visibility, the nanopipette used in Fig. 5.2 was relatively large (aperture radius, $a \cong 300$ nm). In Fig. 5.2b, 5.2d, and

5.2e, a long, an intermediate, and a short time step were used, thus showing different volumes of solution sampled inside the pipette. Assuming that the pipette tip approximates a truncated cone geometry, one can evaluate these volumes as 2300, 500, and 23 fL, respectively (1 fL = 1 μm^3 = 10^{-15} L). The smallest volume that can be dispensed with such a pipette is ~1 fL. However, much smaller pipettes (i.e., a < 10 nm) can easily be produced [11] and used to dispense as little as <1 attoliter (i.e., 10^{-18} L) of liquid. Estimating the solution volume is straightforward when it is relatively large (e.g., >1 fL). Smaller volumes can be evaluated and injections from very small pipettes can be monitored by measuring the pipette resistance and/or current vs. potential curves.

Volume Control by Resistance Measurements.

The organic phase conductivity usually is much lower than that of the aqueous solution. The total pipette resistance is largely determined by that of solution filling its narrow shaft. Thus, the ingress of the external liquid into the pipette produces either a significant increase (when organic solvent is drawn into the water-filled pipette) or decrease (when water is drawn into the organic-filled pipette) in pipette resistance, which can be used to evaluate the volume of the loaded solution. The inside of a laser-pulled micropipette has a shape of a truncated cone that can be described by two parameters: the pipette aperture radius, a, and the angle between the cone element and its axis, α. When the outer solution ingresses into the pipette up to a height h with respect to the orifice, the theoretical value of the pipette resistance can be obtained from Eq. (1):

$$R = R_{out} + \frac{1}{\kappa_{inner} \pi a \tan\alpha} \left(\frac{\rho_{outer}^{inner}}{1 + \left(L \tan\alpha\right)^{-1}} + \frac{1}{1 + L \tan\alpha} \right) \qquad (1)$$

where $\rho_{outer}^{inner} = \kappa_{inner}/\kappa_{outer}$ is the ratio of conductivity of the inner solution to that of the outer solution, $L = h/a$, and R_{out} includes the external solution resistance and the interfacial ion-transfer resistance.

Fig. 5.3 shows the fit between the theory (Eq. **1**, solid line) and the experimental data for a pipette radius a = 110 nm (symbols). One should notice that only one fitting parameter, R_{out}. All other quantities were determined independently, and their values were not used as adjustable parameters.

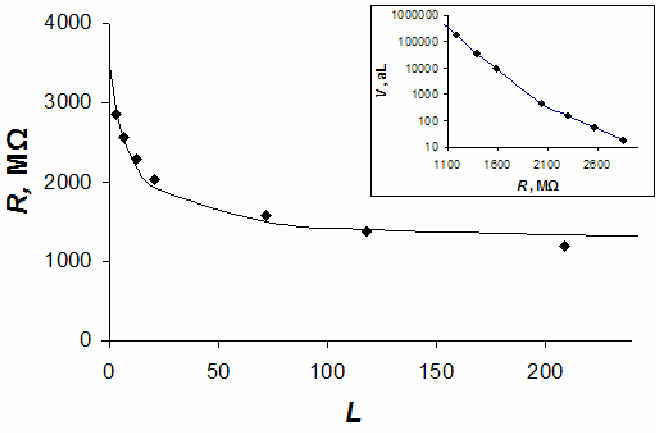

Figure. 5.3. Dependence of the pipette resistance on the amount of water drawn into it. Measured values of pipette resistance (symbols) are fitted to the theory (solid line). The best fit was obtained with R_{out} = 1.2 GΩ. The pipette was filled with DCE containing 10 mM THATPBCl and immersed in a 100 mM $MgSO_4$ aqueous solution. a =110 nm, α = 6.3°, κ_{inner} = 114 μS/cm, and ρ_{outer}^{inner} = 56. The inset shows the correspondent volume vs. resistance dependence calculated from Eq**. 2**.

The pipette radius was found from ion-transfer voltammetry using the second half of the same pipette [11]. κ_{inner} = 114 μS/cm and ρ_{outer}^{inner} = 56 were determined by conductimetry. α = 6.3° was determined from optical micrographs of the pipette.

The volume of the second liquid phase inside the pipette can be calculated as follows

$$V = \frac{\pi a^3}{3\tan\alpha}\left(\left(1 + L\tan\alpha\right)^3 - 1\right) \tag{2}$$

Table 5.1 shows the *V* values obtained from Eq. **2** for different *R* and *L* values.

Table 5.1 Resistance (*R*), *L,* and volume (*V*) values obtained from Fig. 5.3

R, MΩ	*L*	*V*, aL
1339	208.6	175270
1406	117.9	34738
1497	72.0	9029
1928	20.9	443
2193	12.5	158
2536	6.8	55
2923	3.1	18

The smallest measured volume of the filling solution in Table 5.1 is 18 aL, and the smallest volume of dispensed liquid was 37 aL. Smaller volumes can be evaluated by interpolating the *R* vs. *L* curve between *L* = 0 and the first point for experimental point and/or by using smaller pipettes.

Injection Control by Measuring Current-Voltage Curves.

If a pipette is too small for video microscopic observation, the ingress/egress of the outer liquid can be monitored by recording current vs. voltage (or current vs. time) dependences. The main goal here is to avoid the complete expulsion of water from the pipette, which may cause damage to the cell membrane if it comes into direct contact with organic filling solution. Fig. 5.4 shows a current vs. time curve (curve 2), which was obtained by changing the voltage applied to a 400-nm-radius pipette (curve 1).

Curve 2 consists of several linear portions and two highly non-linear regions occurring within the time interval between ~30 s and ~45 s. Video micrographs obtained simultaneously with electrical measurements (not shown) showed that the linear current vs. time (or current vs. voltage) behavior was observed when the pipette was completely filled with DCE. This ohmic response could be fitted to the theory (dashed line) assuming the constant pipette resistance, R = 550 MΩ.

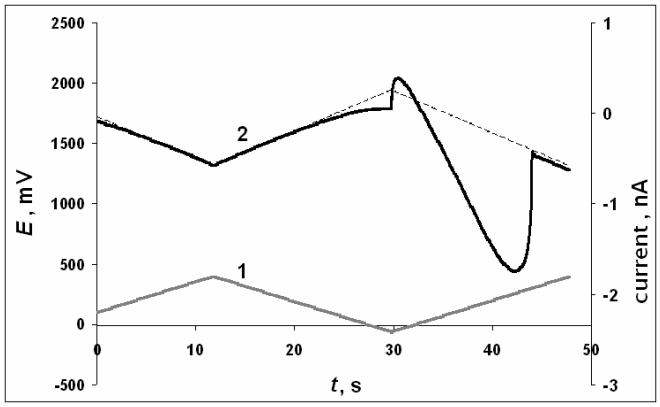

Figure. 5.4. Time dependences of the voltage applied to a pipette (1) and current flowing across the water/DCE interface (2) during the ingress and egress of the outer aqueous solution. The pipette was filled with DCE containing 10 mM THATPBCl and immersed in a 100 mM $MgSO_4$ solution. The pipette radius was 400 nm. The dashed line is the theoretical fit to the linear portions of the current response obtained with a pipette resistance, R = 550 MΩ.

In contrast, highly non-linear current-voltage response corresponds to changes in resistance caused by the ingress/egress of water. The ingress began at t ≅ 30 s and ended at t ≅ 32 s, when the current-time dependence became essentially linear again, but with a much steeper slope corresponding to a lower pipette resistance. Another region of non-linear current-voltage behavior (42s ≤ t ≤ 46s) corresponds to the expulsion of water from

the pipette. When this process is complete, the current-time dependence becomes linear again and follows the same theoretical curve (dashed line). By stopping the injection after the current minimum but before the response becomes linear again, one can ensure that most—but not all—solution loaded into the pipette is ejected from it.

Other modes of voltage control can also be used to operate the syringe, notably, an AC excitation or a cyclic voltage ramp. With a low frequency AC voltage (up to ~20 Hz; 200 mV amplitude) superimposed on a +90 mV DC bias, we observed liquid ingress and egress cycles at the same frequency, essentially synchronized with the applied AC voltage. The electrochemical syringe operated in an AC mode can serve as nanopump driver for microfluidic applications.

Injection of Fluorescent Dye into Mammalian Cells.

We used fluorescent dyes to investigate various aspects of attosyringe performance in cellular injections. The cultured human breast cells (MCF-10A) were previously employed in electrochemical experiments and showed excellent viability during >4 hours time periods under similar experimental conditions [14]. Two fluorescent dyes were employed in our experiments, cationic EB [15] and anionic BODIPY®FLATP [16]. It was shown previously that neither one can cross a mammalian cell membrane.

The injection sequence is shown in Fig. 5.5. With the help of the SECM, which was used as a precise micromanipulator, a tilted nanopipette was placed a few microns away from the cell surface (Fig. 5.5a). Buffer solution containing 10 μM EB was introduced in the nanopipette by applying negative potential to the internal reference electrode and then bringing the voltage to a value at which the solution flow stops (Fig. 5.5b). The pipette was slowly (0.5 μm/s) moved towards the cell and inserted into it (Fig. 5.5c). To minimize the membrane damage, the penetration depth was ≤1 μm. The applied voltage was stepped to 400 mV at which the aqueous solution was slowly (in ~10

seconds) injected into the cell. To stop the injection, the voltage was lowered to -50 mV, so that some solution remained inside the nanopipette, and no direct contact occurred between 1,2-dichloroethane and the cell membrane (Fig. 5.3d). If a pipette is too small for videomicroscopic observation, the injection can be controlled by monitoring either syringe resistance or ion-transfer current, as discussed above. In Fig. 5.5, the injected volume (<100 fL) was sufficiently small, so that no changes in the cell shape, size or position could be detected. After the complete pipette retraction, the process could be repeated to inject solution into another cell.

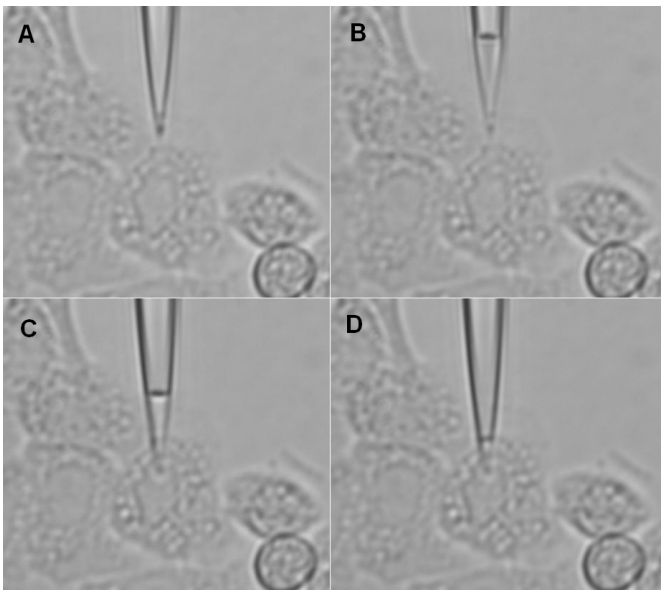

Figure. 5.5. Cell injection using the electrochemical syringe. An ~150-nm-radius pipette is positioned near the cell surface (a), and some amount of buffer solution is loaded into it (b). The nanopipette is then translated toward the cell and penetrates the cell membrane (c). The buffer is injected inside the cell. The injection was stopped before the organic solution reached the pipette tip (d).

The insertion of the pipette into a cell shown in Fig. 5.5 relies on video microscopic control. Even with a relatively large orifice radius (e.g, a =150 nm), the tip of the pipette is too small to be seen. With smaller pipettes, the uncertainty of positioning the pipette may become a problem. Additional control over the cell approach and penetration by the pipette can be achieved by measuring the current flowing across the liquid/liquid interface as a function of the pipette displacement. Because of the blocking effect, the current decreases sharply when the distance between the pipette tip and the cell surface becomes comparable to the pipette radius [17,18]. The current vs. pipette displacement curve can be used to estimate the tip/cell distance during the approach and subsequently control the penetration depth.

In Fig. 5.6, the syringe was used to inject BODIPY® FLATP into immobilized MCF-10A cells. After each injection, the syringe was withdrawn and moved to the next cell.

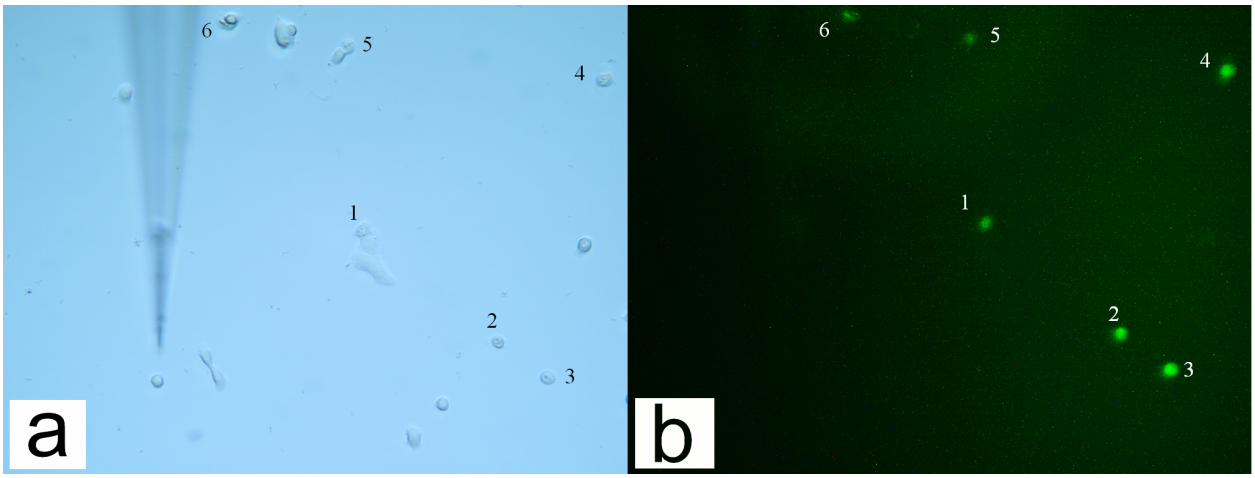

Figure. 5.6. Optical (a) and fluorescence (b) micrographs of immobilized MCF-10 cells. The numbers in (a) and (b) correspond to the same six cells into which BODIPY® FLATP fluorescent dye was injected. (b) The picture was obtained ~30 min after washing the cells with fresh buffer solution to remove excess dye.

The florescence micrograph (Fig. 5.6b) shows that all cells in which the dye was injected became fluorescent. In contrast, other cells present in the optical micrograph (Fig. 5.6a) cannot be seen in Fig. 5.6b because BODIPY® FLATP does not cross the cell membrane. The concentration of dye in the labeled cells did not decrease significantly with time.

Control experiments were done to verify that the solution was injected into cells by the pumping action of the syringe rather than by diffusion from the pipette or by leaking through the hole punched in the membrane. In Fig. 5.7, solution of EB was injected into three cells labeled with the numbers 1 – 3.

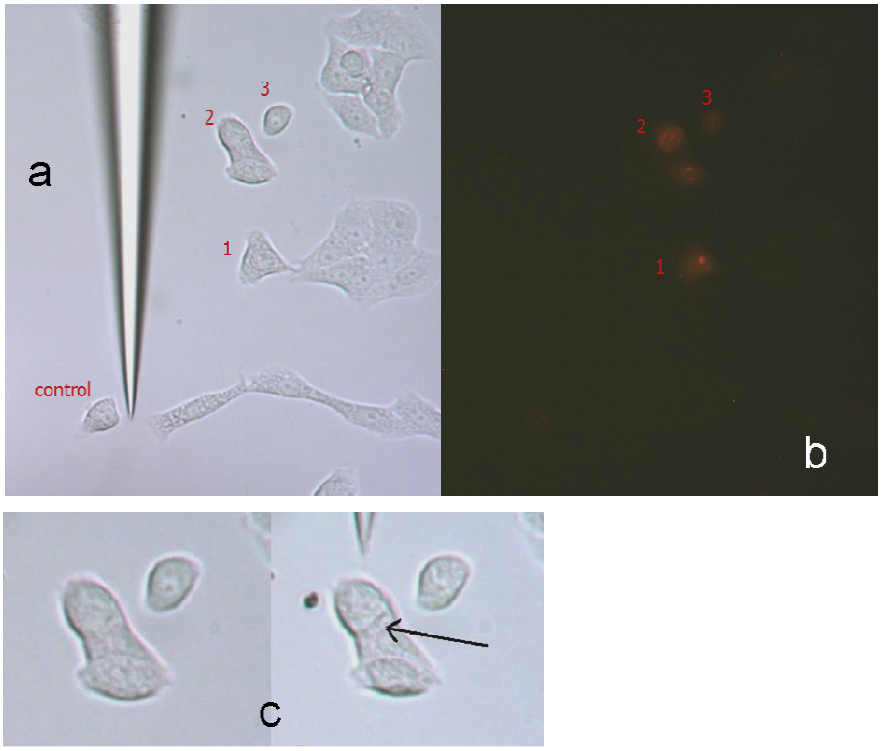

Figure. 5.7. (a) Optical and (b) fluorescence images of a cell field. Cells 1, 2 and 3 were injected with a 10 μM EB buffer solution. The control cell was penetrated by the nanopipette without solution injection. (c) Cell 2 in the beginning of the experiment (left) and ~20 min later (right). The arrow points to the membrane separation.

The same pipette containing EB was used for a mock injection: the pipette was inserted in the control cell, but no solution was injected. Although the pipette spent inside the control cell approximately the same time as in each of three injected cells, the fluorescence images of these cells are markedly different: cells 1, 2 and 3 have become fluorescent, but the control cell did not (Fig. 5.7b). Thus, simple diffusion of EB through the nanopipette orifice and leaking of the outer solution through the hole in the membrane are not sufficiently fast to introduce a significant amount of dye into the cell. Cell # 2 in Fig. 5.7b seems to contain two stained nuclei, which resulted from a single injection of dye. The comparison of the blown up optical micrographs of the same cell in Fig. 5.7c obtained before (left) and immediately after (right) the injection show a line separating the two halves of the cell. This feature, which became more prominent over a few minutes time period, suggests that cell #2 was in the process of mitosis when the dye was injected.

Cell viability was verified by trypan blue-exclusion experiments. Because live cells pump out this blue dye, but dead cells do not, dead cells appear blue while live cells appear uncolored. After each series of injections, trypan blue solution (~5 μM) was added to the cell medium. In this way, all MCF-10A cells were confirmed to be alive following the injection.

5.4 Discussion

While the basic idea of the electrochemical syringe is simple, the physicochemical processes involved in its operation are very complicated [19]. The surface tension effects largely responsible for the liquid flow are not limited to the liquid/liquid interface but also depend on the water/glass and organic solvent/glass boundaries, and a three-phase water/organic/glass boundary. The properties of the inner pipette wall can be changed by modifying its surface [18,20]. Rendering the glass surface more hydrophobic, e.g., via

silanization, inhibits the ingress of water into the capillary [18]. In this way, both the extent of control over the solution ingress/egress and the magnitude of the required voltage can be varied.

Other parameters affecting the syringe operation include the concentrations and the nature of electrolytes in both aqueous and organic solutions. If the electrolyte concentrations are too low, the applied voltage drops within the bulk solution phase rather than across the liquid/liquid interface [10], thus preventing one from controlling the surface tension and the fluid motion. Typically, the ionic strength inside the cell and in the culture medium is sufficiently high, and the concentration of organic electrolyte should be at least 10 mM. On the other hand, by some less obvious reason, ionic concentrations that are too high either in aqueous or in organic phase (e.g., >0.1 M) also impair the electrochemical control of the fluid motion.

Both aqueous and organic solutions contain relatively high concentrations of ionic species, which can cross the phase boundary when voltage is applied across the liquid/liquid interface [10]. For optimal syringe performance, the ion-transfer current should be minimized by using hydrophobic organic electrolyte (e.g., THATPBCl). By lowering ion-transfer current, one can also minimize the polarization of the cell membrane during the injection. Generally, the pipette current should be much smaller than the combined current through the cellular ion channels. Since an individual channel current is of the order of a few pA [21], the electrochemical injection should not cause significant depolarization of the cell membrane if the pipette current is on the pA scale.

Because the glass surface is usually charged (the charge density depends on the nature of the solution in contact with glass and its pH) [22], both electrophoresis and electroosmosis occur within the narrow shaft of the nanopipette when external voltage is applied to it [12,23]. These processes further complicate the theoretical description of the electrochemical syringe. The electrophoresis is especially important if the species to be injected into the cell are charged: while the injection of cationic species is facilitated by

the applied voltage, anions are moved by the electric field in the opposite direction and may even be transferred to the organic filling solution. Fortunately, the expulsion of water from the pipette caused by the change in surface tension is usually faster than electrokinetic processes, and thus both cationic (e.g., EB) and anionic (e.g., BODIPY® FLATP) species can be injected.

The electrochemical syringe offers several important advantages over other existing microinjectors. It is easy to fabricate, inexpensive, and easy to use. It can be made very small, and can reproducibly draw and eject small volumes of liquid as many times as needed. The electrochemical injection method does not require pressure to be applied to the nanopipette. This is an advantage because the radius of a nanopipette used for electrochemical injections can be much smaller, and a better control of the injected volume can be achieved. Unlike the stab injection method, in which the volume of injected material is determined by the time the pipette spends inside the cell, with the electrochemical syringe this time constraint is removed since the flow can be induced or stopped by changing the applied voltage. This, in turn, allows for a better control of the injection while minimizing the extent of penetration and thus reducing damage caused to the cell.

While a small injection volume is useful when one works with biological cells, dispensing higher volumes of fluids may be required for other applications [24]. With larger pipettes (e.g., $a \sim 10$ μm) that can also be used as an electrochemical syringe, one can deliver pL volumes of fluids. A very wide range (≥6 orders of magnitude) of the dispensed solution volume suggests that electrochemical syringe can find applications in various fields from cell biology to nanolitography to microfluidics [25,26].

Chapter VI

Nanoelectrochemistry of living cells

6.1 Introduction

The changes in intracellular redox state can be related to various pathological conditions such as oxidative stress [1], diabetes [2] and cancer [3]. Electrochemical measurements can provide comprehensive information about intracellular redox state including concentrations of redox species, kinetics of redox reactions and charge transport rates. Microelectrodes positioned near the cell surface [4,5] and the scanning electrochemical microscope (SECM) [6-8] have been used for such measurements. The applications ranged from dopamine [4] and cholesterol [9] analysis to studies of menadione metabolism in yeast [10] and hepatoblastoma cells [11] to detection of reactive oxygen species [12] and monitoring the drug efflux from cancer cells [13]. The SECM was also used for micron-scale topographic and reaction rate imaging of various types of biological cells [14-17].

We showed earlier that intracellular redox activity can be probed noninvasively by measuring the rate of transmembrane charge transfer (CT) using the feedback mode of the SECM operation [17]. In such experiments, the tip electrode is placed in solution containing the oxidized (or reduced) form of a redox mediator. A mediator species is then reduced (or oxidized) at the tip electrode. A piezo-positioner is used to move the tip towards the surface of an immobilized cell. If the mediator species is hydrophobic, the product of the tip reaction can cross the cell membrane and be re-oxidized (or re-reduced)

via intracellular redox reaction (Fig. 6.1A). This process can produce an enhancement in the faradaic current at the tip electrode (positive feedback) depending on the mediator regeneration rate and the tip/membrane separation distance (*d*).

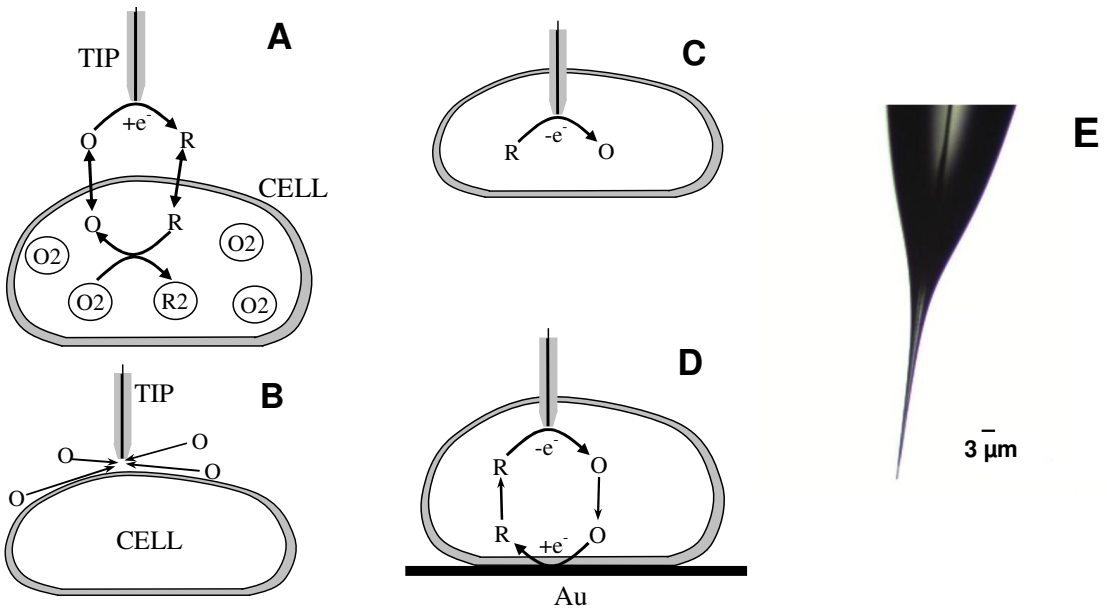

Figure 6.1. (A) – (D) Schematic diagrams of the SECM experiments with single cells and an optical micrograph of a typical nanotip employed in such experiments (E). (A) The tip is positioned in the solution close to the cell surface. Positive feedback is due to bimolecular electron transfer between hydrophobic redox mediator (O/R) and cell-bound redox moieties (O2/R2). (B) The lipid cell membrane is impermeable for a hydrophilic redox mediator. Negative feedback is due to the hindered diffusion of redox species to the tip electrode. (C) Nanoelectrode voltammetry inside the cell. (D) Positive feedback is produced by mediator regeneration via electron transfer at the underlying Au surface.

If the mediator is hydrophilic, it cannot cross the cell membrane, which blocks the diffusion of species O to the tip (Fig. 6.1B), so the tip current (i_T) decreases with *d*

(negative feedback). Some useful information about intracellular redox state was extracted from the analysis of i_T vs. d curves [17]. However, the mechanism of mediator regeneration by the cell is rather complicated, and the need to include transmembrane CT processes makes the data analysis even more difficult [18].

More informative and easier to interpret data could be obtained by making electrochemical measurements inside an immobilized cell or by using "artificial cells" [19, 20]. Only few examples of intracellular electrochemical measurements have been reported to date [21-23]. One of the main obstacles here is the electrode size and geometry: even a sharp conical electrode puncturing a lipid membrane may cause a solution leakage [20]. Also, one would need nanometer-sized electrodes for spatially resolved intracellular measurements, and the characterization of conical nanoelectrode geometry is challenging [24].

Here we report the use of the SECM equipped with well-characterized polished nanotips (radius, $a \geq 10$ nm) for spatially resolved quantitative experiments inside living cells (Fig. 6.1C). In this way, one can determine the mass/charge-transfer rate across the cell membrane (Fig. 6.1D), evaluate the membrane potential, and measure the redox properties with a nanoscale resolution. Very sharp tips (Fig. 6.1E) with the radius of insulating glass, $r_g \cong 3a$ were used to minimize the mechanical damage to the cell.

Under steady-state conditions, the thickness of the diffusion layer is equal to a few nanoelectrode radii, and therefore a nanoprobe "sees" only local electrochemical properties of a nanometer- or a submicrometer-sized domain. In a system as complicated as a living cell, the ability to probe local redox environment instead of analyzing complicated response originating from different subcellular compartments is an important

advantage. The high spatial resolution offered by nanotips can also be used for nanoscale imaging of cellular topography and surface reactivity that could be complementary to AFM [25], scanning ion-conductance microscopy [26], and "superresolution" optical methods [27].

6.2 Results

SECM Measurements and Intracellular Voltammetry.

The current vs. distance (i_T -d) curve in Fig. 6.2A was obtained with a hydrophilic redox mediator, 1 mM $Ru(NH_3)_6^{3+}$, which could not permeate the cell membrane acting as an insulator. A 42-nm polished Pt tip approached and penetrated an immobilized MCF-10A cell (positive d corresponds to the tip approaching the membrane; negative distances—within the cell volume). The experimental approach curve (symbols) fits the SECM theory [28] (solid line) for $d \gtrsim 0.5a$ at which the tip began to push the cell membrane. One should notice that the tip/membrane separation distance at the point of the closest approach is ~20 nm. This indicates that the SECM equipped with a nanometer-sized tip can potentially be used for topographic imaging of cell surfaces with a ~20-nm scale resolution.

At $d \cong -1.2a$, the tip gets inside the cell, and the current vanishes. Accordingly, the wave of $Ru(NH_3)_6^{3+}$ reduction was observed in the outer buffer solution (curve 1 in Fig. 6.2B) but not inside the cell (curve 2). This indicates that the membrane immediately forms a tight seal around the penetrating nanotip that prevents the external solution from leaking inside the cell. The use of a small and very sharp tip is essential here: from Fig. 1E one can see that the maximum radius of the electrode portion inserted into the cell is

<<1 µm even when the length of that part is ~5 µm. (One should notice that the tip of the nanoelectrode is not visible in Fig. 6.1E).

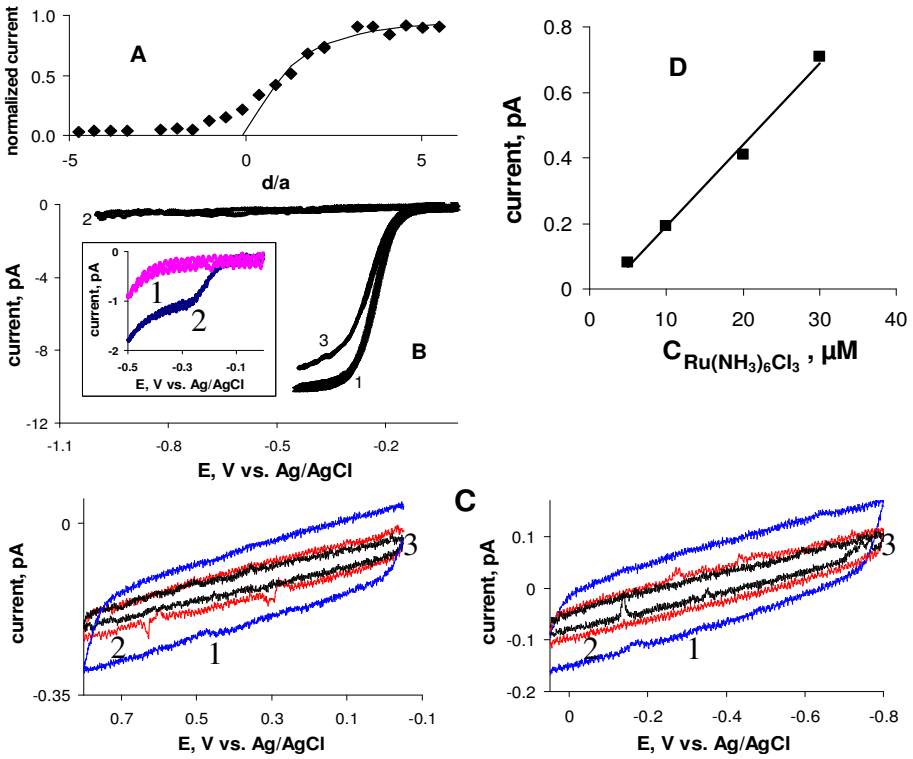

Figure. 6.2. Current vs. distance curve obtained with a Pt tip approaching and penetrating an MCF-10A cell (A) and voltammograms obtained at nanoelectrodes inside living cells and in solution (B – D). (A) Solid line is the theoretical curve for an insulating substrate [28]. The tip current is normalized by the value measured in the bulk solution. The approach speed was 20 nm/s. (B) Voltammograms obtained (1) in the bulk solution outside of the cell, (2) inside the cell, and (3) in external solution after the tip was withdrawn from the cell. Inset: voltammograms obtained in PBS (2) and inside the cell (1) without purging solution with nitrogen. (C) Intracellular voltammograms obtained by scanning the electrode potential between 0 and +0.8 V (left), and 0 and -0.8 V (right). The scan rate was (mV/s): 50 (1), 20 (2) and 10 (3). The concentration of $Ru(NH_3)_6Cl_3$ in PBS was 1 mM (A) – (C) and 0.1 mM (inset in B). (D) Dependence of the steady-state diffusion limiting current vs. concentration of $Ru(NH_3)_6Cl_3$. The tip radius (nm) was: 42 (A), 39 (B), 54 nm (C), and 73 (D).

In contrast to $Ru(NH_3)_6^{3+}$, the oxygen reduction wave inside the cell (inset in Fig. 6.2B, curve 1) is very similar to that measured outside (inset in Fig. 6.2B, curve 2 at potentials, $E \lesssim$ -400 mV), due to rapid oxygen transport across the membrane. This wave disappeared when the solution was purged with nitrogen to remove O_2 (curve 2 in Fig. 6.2B). From curve 2, one also can see that the concentration of mobile redox species in the cell is very low. Our previous experiments [17,18] showed that the effective concentration of redox centers in the cell, which can be reduced (or oxidized) within the potential window in Fig. 6.2B, is ≥1 mM. Thus, most (if not all) of those redox moieties are immobilized and cannot freely diffuse in the cytoplasm. We used a home-built ultra-sensitive potentiostat to check if micromolar concentrations of any mobile redox species can be detected inside the cell. The voltammograms in Fig. 6.2C were obtained by scanning the tip potential in either positive (left panel) or negative (right panel) direction. No voltammetric waves were detected in the curves obtained at different scan rates (50 mV/s, curves 1; 20 mV/s, curves 2, and 10 mV/s, curves 3). The sensitivity of these measurements can be evaluated from Fig. 6.2D, which presents a calibration curve for a 73-nm tip obtained with a concentration of $Ru(NH_3)_6^{3+}$ ranging from 5 to 50 μM. Clearly, the oxidation-reduction of ≤1 μM of species should be detectable in our experiments.

The approach curves and intracellular voltammograms in Fig. 6.3 obtained with a hydrophobic mediator ($FcCH_2OH$) that can cross the lipid membrane, are very different. In this case, i_T decreased and then stabilized at a non-zero value after the tip penetrated the cell (Fig. 6.3A). The well-shaped voltammograms of $FcCH_2OH$ were obtained both in the outer solution (Fig. 6.3B, curve 1) and inside the cell (curve 2).

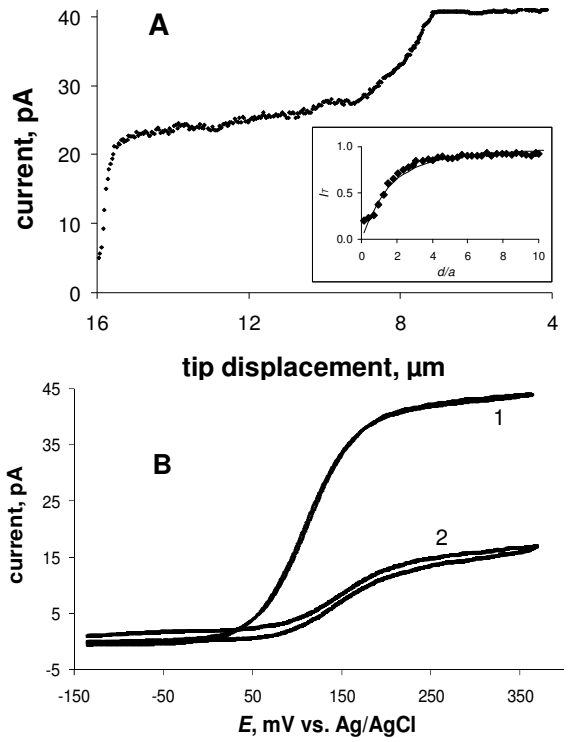

Figure. 6.3. (A) A 144-nm tip approaches and penetrates an MCF-10A cell in PBS containing 1 mM $FcCH_2OH$. (B) Steady-state voltammograms obtained at the same tip outside (1) and inside (2) the cell. The inset in (A) shows the fit between the experiment (symbols) and the theory (solid line) for the final part of the curve where the tip approached the inner side of the cell membrane attached to the bottom of the Petri dish.

Four distinct regions can be seen in the approach curve in Fig. 6.3A. The essentially flat initial part (tip displacement, $l \lesssim 7$ µm) corresponds to the tip/cell distances much longer than a. Negative feedback is observed when the tip moves closer to the cell, pushes the membrane and finally penetrates it at $l \cong 9$ µm. Since $FcCH_2OH$ is present inside the cell, the exact penetration moment is harder to detect than in the case of a hydrophilic redox mediator (cf. Fig. 6.2A). When the tip is inside the cell but close to

the membrane, the measured current is ~30 - 40% lower than that in the outer solution. This difference can be attributed to the lower diffusion coefficient of $FcCH_2OH$, and it is consistent with the relative viscosity (cytoplasm versus water) of 1.5 [29]. A slow decrease in the tip current occurring in next part of the approach curve (9 μm $\lesssim l \lesssim$ 14.5 μm) corresponds to the concentration profile of $FcCH_2OH$ inside the cell.

A much steeper current decay in Fig. 6.3A occurs when the tip approaches the bottom of the cell that is attached to the insulating plastic surface (15 μm $\lesssim l$). An excellent fit between the experimental data and theory in Fig. 6.3A (inset) suggests the possibility of spatially resolved, quantitative intracellular measurements. This result is in accordance with the high-quality of voltammograms of hydrophobic mediators obtained inside the cell (e.g., curve 2 in Fig. 6.3B). A number of reproducible intracellular voltammograms were recorded over a time period of several minutes. Furthermore, the voltammograms of $Ru(NH_3)_6^{3+}$ and $FcCH_2OH$ measured after withdrawing the tip from the cell were similar to those obtained before the cell penetration (cf. curves 1 and 3 in Fig. 6.2A). A usual concern in bioelectrochemistry is that the electrode response may be affected by protein adsorption and fouling of its surface. Apparently, surface fouling was not an issue in our nanoelectrode experiments.

Cell viability was verified by trypan blue-exclusion experiments. Because live cells pump out this dye, but dead cells do not, dead cells appear blue while live cells appear uncolored. After the tip was withdrawn from the cell (which was not possible to do in a few cases when the cell adhesion to the dish surface was not sufficiently strong), ~5 μM solution of trypan blue was added to the cell medium. In this way, MCF-10A cells were confirmed to be viable 1 – 2 hours after intracellular electrochemical experiments.

Evaluation of the Membrane Potential.

The tip potential in both curves in Fig. 6.3B was measured with respect to the same Ag/AgCl reference electrode located in PBS outside the cell. The 36 mV difference between the half-wave potentials ($\Delta E_{1/2}$) in curves 2 and 1 can be attributed to the potential drop across the cell membrane. This experiment was repeated with 18 different MCF-10A cells and different nanoelectrodes (19 nm ≤ a ≤ 182 nm) yielding $\Delta E_{1/2}$ = 46 ± 4 mV (the uncertainty is expressed as a 95% confidence interval). $\Delta E_{1/2}$ was also measured for three MCF-10A cells bathed in PBS that contained a different hydrophobic redox species (TMPD). Although the quality of intracellular voltammograms of TMPD was not as high as for $FcCH_2OH$, a similar mean value, $\Delta E_{1/2}$ = 39 mV, was obtained for this system.

To further investigate the correlation between $\Delta E_{1/2}$ and membrane potential, this quantity was measured again after 600 nM of valinomycin was added to PBS without removing the tip from the cell. Valinomycin, which depolarizes the membrane by acting as a potassium carrier, was expected to diminish the membrane potential. In each of these experiments, which were done for seven MCF-10A cells, the $\Delta E_{1/2}$ decreased markedly, and the mean value (16.7 mV for $FcCH_2OH$ mediator) was much lower than that measured without valinomycin.

Although there is some variability in the membrane potential values reported in the literature, our $\Delta E_{1/2}$ values are somewhat more positive than most numbers obtained for mammalian cells by different techniques (e.g., -58.6 mV to -2.7 mV reported for MCF-7 human mammary tumor cells in ref. 30). To determine whether this difference results from membrane polarization that may be induced by current flowing between the

intracellular nanoprobe and the external reference electrode, we measured the dependence of $\Delta E_{1/2}$ on concentration (c_{FcCH_2OH}). The ohmic potential drop across the membrane (iR, where R is the membrane resistance) is proportional to current flowing at the tip electrode inserted in the cell. Five voltammograms in Fig. 6.4A were obtained with the same 112 nm tip in the bulk solution (curve 1) and inside the same cell (curves 2 – 5). By changing c_{FcCH_2OH} in solution, we measured the linear concentration dependence of the tip current corresponding to the half-wave potential ($i(E_{1/2})$; Fig. 6.4B).

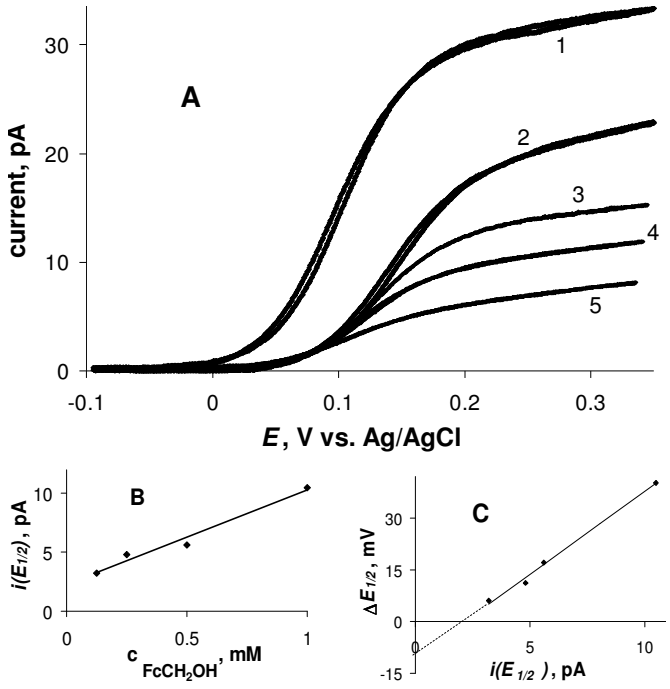

Figure. 6.4. (A) Voltammograms of $FcCH_2OH$ at a 112 nm Pt tip obtained in the bulk solution (1) and inside the same cell (2 – 5); and corresponding dependences of $i(E_{1/2})$ vs. c_{FcCH_2OH} (B) and $\Delta E_{1/2}$ vs. $i(E_{1/2})$ (C). (A) c_{FcCH_2OH} (mM) was: 1 (1) and (2), 0.5 (3), 0.25 (4), and 0.125 (5).

The $\Delta E_{1/2}$ value decreased upon dilution of $FcCH_2OH$, and $\Delta E_{1/2}$ vs. $i(E_{1/2})$ plot was also linear (Fig. 6.4C). The membrane resistance extracted from the slope of this line is ~4 GΩ. The extrapolation of the $\Delta E_{1/2}$ vs. $i(E_{1/2})$ dependence to zero current shows that the membrane potential corrected for the polarization effect is somewhat more negative (e.g., ~ -10 mV in Fig. 6.4C).

Measuring the Mass/Charge Transfer Rate across the Cell Membrane.

In these experiments, the cells were immobilized on a conductive surface, i.e., a glass slide coated with an evaporated Au film. Menadione, which can readily cross the MCF-10A cell membrane [17], was used as a redox mediator. Its reduced form (menadiol) was generated at the tip and reoxidized at the Au surface (Fig. 6.1D). SECM approach curves (Fig. 6.5) were obtained by moving the tip downward inside the cell until its insulator sheath began to push against the membrane and the underlying surface. Since the mediator regeneration at the Au surface is rapid, it was possible to evaluate the mass-transfer rate of mediator species across the membrane from the tip current vs. distance curve. When the feedback current is controlled by the rate of membrane transport, the shape of i_T vs. d curve can be described by equation derived for the finite heterogeneous kinetics of the mediator regeneration at the substrate [18].

Fitting an experimental current vs. distance curve to the theory [31] yields the dimensionless heterogeneous rate constant, $\kappa = Pa/2D$, where $P = KD_m/l_m$ is the permeability coefficient, D and D_m are the diffusion coefficients of redox species in the cytoplasm and in the membrane, respectively, K is the solution-to-membrane partition coefficient of the redox species, and l_m is the membrane thickness. Curves 1 and 2 in Fig.

6.5 were obtained with 790-nm and 280-nm tips, and yielded the κ values of 1.01 and 0.42, respectively.

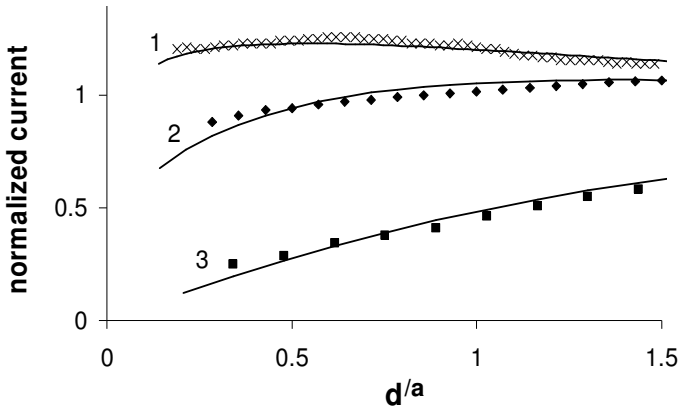

Figure. 6.5. Evaluating the rate of charge/mass transport across the cell membrane from SECM approach curves. The tip radius (nm) was: 790 (1), 280 (2), and 146 (3). Experimental data (symbols) was fitted to the theory (solid lines) for finite charge transport kinetics [31] (curves 1 and 2) and pure negative feedback [28] (curve 3).

The difference between the corresponding P values (with D = 4.7 ^{x} 10^{-6} cm^2/s, the menadione diffusion coefficient in cytoplasm), i.e., 0.13 cm/s and 0.15 cm/s, is within the range of our experimental error. Curve 3 in Fig. 6.5 was obtained with a smaller, 146-nm tip, for which the expected κ was ~0.2. This value is close to the lower limit for the rate constant measurable by SECM. Therefore, curve 3 could be fit to the SECM theory for an insulating substrate, and no reliable P value could be extracted from it.

Nanoscale Electrochemical Imaging of Cell Membranes.

Two SECM images of MCF-10A cells are shown in Fig. 6.6. A 11.8 µm x 11.2 µm constant-current image (Fig. 6.6A), representing most of the cell surface, was obtained with a 123 nm tip in PBS containing 1 mM $Ru(NH_3)_6^{3+}$. While some topographic features visible in the SECM image can also be found in the optical micrograph of the same cell (Fig. 6.6B), no close similarity can be expected because Fig. 6.6B is a transmitted light picture obtained using the inverted microscope. The spatial resolution of the SECM image is ~200 nm.

Since the spatial resolution of SECM is determined by the tip radius [31], one can "zoom in" on a small area of the cell membrane by using a smaller tip. In Fig. 6.6C, a 0.6 µm x 1.5 µm area was imaged in a constant-height mode using a 47 nm probe. The tip was moved vertically towards the cell, and the resulting current vs. distance curve (similar to that in Fig. 6.2; not shown) was recorded. The approach was stopped before the tip current deviated from the theory, i.e., before the insulating sheath began to push the membrane. To obtain the image, the tip was scanned laterally in the x-y plane above the cell. The lateral resolution of such an image is better than 100 nm, and it can be further improved by decreasing the tip/membrane separation distance.

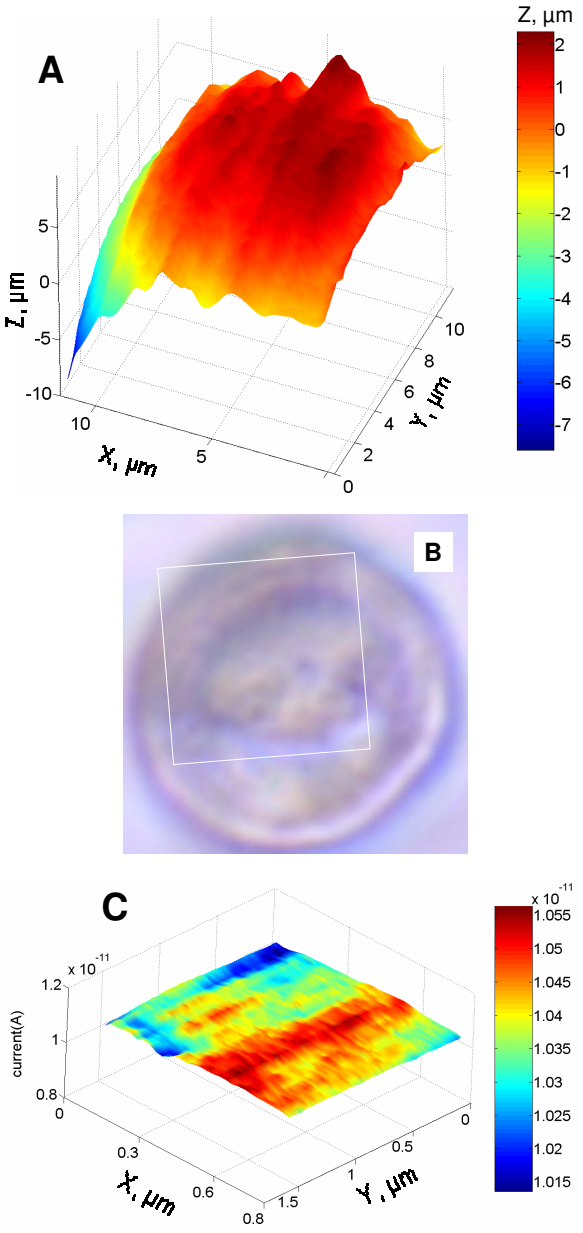

Figure. 6.6. Human breast epithelial (MCF-10A) cells imaged by the SECM. (A) 11.8 µm x 11.2 µm constant-current image of a cell obtained with a Pt tip (a = 123 nm, $r_g = 3a$) and (B) Optical image of the same cell. A rectangular frame shows the area of the cell imaged in A. (C) Constant-height image of a 0.6 µm x 1.5 µm portion of cell surface obtained with a 47 nm tip. PBS contained 1 mM $Ru(NH_3)_6Cl_3$ as redox mediator.

6.3 Discussion

Quantitative nanoelectrochemical measurements inside a living cell can be done to evaluate potentials, concentration profiles, and charge-transfer kinetics. A very small size of the used nanoprobes allows one to minimize the damage to the cell and to achieve high spatial resolution. However, intracellular redox moieties are apparently localized and cannot diffuse freely within the cell (Figs. 6.2B and 6.2C). This necessitates the use of a redox mediator in intracellular voltammetry. To probe enzymatic redox reactions, the mediator concentration must be on the micromolar scale [18], and very low (fA-range) currents have to be measured. Another difficult problem is to precisely position a nanoelectrode at a specific location within the cell (e.g., in a proximity of a mitochondrion). In the future, it may be possible to address this issue by using redox-sensitive fluorescent labels.

Previously developed approaches to evaluation of the membrane potential (e.g., those based on cell-attached patches [32], ion-selective probes [33], and fluorescent dyes [34] have numerous shortcomings from the relatively large size of a potentiometric probe to ambiguity of data analysis [32]. Intracellular voltammetry is a relatively straightforward method, in which the membrane potential is evaluated with no additional assumptions or complicated data analysis. The measurements should be made with the as low concentration as feasible in order to minimize the ohmic potential drop across the membrane. $\Delta E_{1/2}$ varies slightly when the tip is moved inside the cell. Such variation may occur when additional membranes appear between the extracellular reference electrode and the tip as the latter enters a subcellular compartment (e.g., Golgi apparatus). To avoid

this complication, one should extract $\Delta E_{1/2}$ from voltammograms obtained at the tip soon after it has penetrated the cell.

Measurements of transport rates across biomembranes are challenging even for model systems, e.g., lipid bilayers [35]. We have previously tried to evaluate the rate of the cross-membrane charge transport from extracellular SECM experiments by analysis of a model involving two additional steps. The *P* values measured in ref. 18 for the same mediator (menadione) and the same cell line (MCF-10A) were about one order of magnitude lower. Most likely, the results in ref. 18 were affected by slow intracellular redox reaction. The intracellular SECM experiments are free from this problem. One should notice that a solution film always exists between the bottom of the cell and the surface to which it adheres. Although the film thickness of ~10 nm [36] is too small to affect our measurements, a possible effect of the underlying gold surface on membrane permeability has yet to be investigated.

To our knowledge, the only reported nanoscale SECM images of biological samples are those of mouse monoclonal IgG, DNA and other biomolecules obtained on a mica substrate in humid air [37]. The main difficulty in feedback mode SECM imaging of living cells on the nanoscale is that the separation distance between the tip and the membrane has to be of the order of the tip radius. In the constant current mode (Fig. 6.6A), the constant distance between the tip surface and the cell is maintained, and the tip follows the cell contour [38]. In this way, the entire cell or a major portion of it can be imaged with a high spatial resolution using a tip radius much smaller that the cell dimensions. Using this approach, high quality topographic images of neuron cells were

obtained previously with a spatial resolution of ~1 μm (14). Here, we used a small and very sharp tip with r_g <3*a* to increase the resolution to ~200 nm.

The constant-height image (Fig. 6.6C) was obtained by scanning a 47 nm tip laterally above the cell in the x-y plane. If the tip radius is significantly smaller than the variations in height between different parts of a cell, either the higher parts get scratched in the process of imaging, or the lower parts are not imaged clearly. However, a small and relatively flat portion of the cell surface (e.g., 0.6 μm x 1.5 μm in Fig. 6.6C) can be imaged with the spatial resolution much higher than that in any previously reported SECM image of living cells.

A hydrophilic mediator used to obtain images in Fig. 6 could not permeate the cell membrane. Thus, both images represent only cell topography. Previously [17], we mapped redox reactivity of mammalian cells with micrometer spatial resolution using a hydrophobic mediator. A current-distance curve (Fig. 6.3) suggests that reactivity mapping can also be done at the nanoscale because some feedback from the cell could be seen when the tip approached its surface. The combination of SECM with fluorescence microscopy [39] should help one interpret such images and extract spatially resolved information on cellular redox reactivity.

6.4 Materials and Methods

Electrodes.

A two-electrode setup was employed for voltammetry and SECM experiments with a nm-sized Pt working electrode and a commercial Ag/AgCl reference. 100-nm-

thick evaporated Au films on glass were obtained as a gift from Alexander Vaskevich (Weizmann Institute of Science) and used as a conductive SECM substrate for CT rate measurements across the cell membrane. The preparation of polished, needle-like, disk-shaped nanotips was similar to the previously described procedures (40). Briefly, 25-μm annealed Pt wires were pulled into borosilicate glass capillaries (1.0-mm o.d., 0.58-mm i.d.) under vacuum with the help of a P-2000 laser pipet puller (Sutter Instrument Co., Novato, CA). The pulling program was modified by increasing the heat and velocity parameters to obtain a long and sharp tip with a thin glass sheath required for easier membrane penetration. Polishing was performed under videomicroscopic control on a 50-nm lapping tape [40]. The effective radius was evaluated from steady-state voltammetry and SECM [40].

Cell Culture.

Mid-passage MCF-10A cells, a human breast epithelial cell line, were cultured in a 60-mm plastic culture dish containing DMEM/F12 media (1:1) supplemented with 5% equine serum, insulin (10 µg/ml), epidermal growth factor (20 ng/ml), cholera toxin (100 ng/ml), and hydrocortisone (0.5 µg/ml) and maintained with penicillin (100 units/ml), streptomycin (100 µg/ml), and fungizone (0.5 µg/ml). Cells were redistributed at 1:3 to 1:6 every 3 to 4 days. Cells were plated at 5-20% confluence (2-8 x 10^3 cells/60-mm plate) on the day before the experiment. For experiments requiring an underlying conductive surface, cells were cultured on a glass slide covered with an evaporated Au film, which was fixed in a culture dish. Culture media, serum, and antibiotics (fungizone, penicillin, streptomycin) were purchased from Invitrogen Corp. (Rockville, MD). Prior to

each experiment, adherent cells were rinsed with pH 7.4 phosphate-buffered saline (PBS) without calcium or magnesium (Cambrex Bio Science Inc., Walkersville, MD USA), which was used as electrolyte in all electrochemical experiments.

Instrumentation and Procedures.

All measurements were performed at ambient temperature in a plastic culture dish mounted on the horizontal stage of an Axiovert-100 inverted fluorescence microscope (Zeiss) that was set on an optical table. The cells were immersed in PBS containing the redox mediator. A home-built SECM instrument [40] was set on the same optical table as the microscope, so that the SECM tip could be positioned above the cell culture plate. Three types of experiments were performed: (i) i_T vs. d curves (approach curves [31]) were obtained by positioning the tip above the cell and slowly moving it vertically down towards the cell surface, penetrating the cell, and continuing to move towards the underlying plastic or Au surface; (ii) topographic images of the cell were obtained by recording variations in tip current (constant-height mode [31]) or z-coordinate (constant-current mode [31]) while the probe was scanned laterally above the cell surface; and (iii) steady-state voltammograms were obtained by positioning the tip either above the cell or inside it and sweeping the tip potential.

In penetration experiments, when $Ru(NH_3)_6Cl_3$ was used as a redox mediator, solutions were deaerated. To prevent damage to the cells, oxygen was removed from the medium for a brief period that immediately preceded the actual measurements. The nearly complete removal of O_2 was evident from cyclic voltammetry (Fig. 6.2B, curve 2).

Chapter I References and Notes

1. G. Gouy, C. R. *Acad. Sci.* **1910**, *149*, 654.
2. D. L. Chapman, *Philos. Mag.* **1913**, *25*, 425.
3. E. J. W. Verwey, K. F. Niessen, *Philos. Mag.* **1939**, *28*, 35.
4. C. Gavach, P. Seta, B. D'Epenoux, *J. Electroanal. Chem.* **1977**, *83*, 225.
5. M. Gros, S. Gromb, C. Gavach, *J. Electroanal. Chem.* **1978**, *89*, 29**.**
6. Y. Cheng, V. J. Cunnane, D. J Schiffrin, L. Murtomäki, *J. Chem. Soc. Faraday Trans.* **1991**, *81*, 107.
7. H. H. Girault, in *Modern Aspects of Electrochemistry*, J. O.M. Bockris, Ed. (Plenum, New York, 1993), vol. **25**, p. 1.
8. G. Luo, S. Malkova, S. V. Pingali, D. G. Schultz, B. Liu, M. Meron, I. Benjamin, P. Vanysek, M. L. Schlossman, *J. Phys. Chem. B* **2006**, *110*, 4527.
9. H. H. Girault, D. J. Schiffrin, *J. Electroanal. Chem.* **1983**, *150*, 43.
10. (a) H. H. Girault, D. J. Schiffrin, B. D. V. Smith, *J. Colloid Interface Sci.* **1984**, *101*, 257; (b). H. H. Girault, *Electrochim. Acta* **1987**, *32*, 383.
11. G. Luo, S. Malkova, J. Yoon, D. G. Schultz, B. Lin, M. Meron, I. Benjamin, P. Vanysek, M. Schlossman, *Science* **2006**, *311*, 216.
12. (a) I. Benjamin, *J. Phys. Chem.* **1992**, *97*, 1432; (b) I. Benjamin, *Science* **1993**, *261*, 1558; (c) K. J. Schweighofer, I. Benjamin, *J. Phys. Chem.* **1995**, *99*, 9974; (d) K. J. Schweighofer, I. Benjamin, *J. Electroanal. Chem.* **1995**, *391*, 1; (e) K. J. Schweighofer, I. Benjamin, *J. Phys. Chem. A* **1999**, *103*, 10274.
13. L. X. Dang, *J. Phys. Chem. B* **1999**, *103*, 8195.
14. (a) P. A. Fernandes, M. N. D. S. Cordeiro, J. A. N. F. Gomes, *J. Phys. Chem.* B **1999**, *103*, 8930; (b) P. A. Fernandes, M. N. D. S. Cordeiro, J. A. N. F. Gomes, *J. Mol. Struct. :THEOCHEM* **1999**, *463*, 151.
15. A. Pohorille, M. A. Wilson, *J. Mol. Struct.: THEOCHEM* **1993**, *284*, 271.

16. T.-M. Chang, L. X. Dang, *Chem. Rev.* **2006**, *106*, 1305.

17. (a) Z. Samec, V. Mareček, D. Homolka, *J. Electroanal. Chem.* **1981**, *126*, 105; (b) Z. Samec, *J. Electroanal. Chem.* **1980**, *111*, 211.

18. H.H. Girault, D. Schiffrin, *J. Electroanal. Chem.* **1988**, *244*, 15.

19. (a) R. A. Marcus, *J. Phys. Chem.* **1990**, *94*, 1050; (b) R. A. Marcus, *J. Phys. Chem.* **1990**, *94*, 4152.

20. T. Kakiuchi, *J. Electroanal. Chem.* **1992**, *322*, 55.

21. W. Schmickler, *J. Electroanal. Chem.* **1997**, *426*, 5.

22. S. Frank, W. Schmickler, *J. Electroanal. Chem.* **2000**, *483*, 18.

23. R. A. Marcus, *J. Chem. Phys.* **2000**, *113*, 1618.

24. A. A. Komyshev, A. M. Kuznetsov, M. Urbakh, *J. Chem. Phys.* **2002**, *117*, 6766.

25. A. J. Bard, F.-R.F. Fan, D. T. Pierce, P. R. Unwin, D. O. Wipf, F. Zhou, *Science* **1991**, *254*, 68.

26. F.-R.F. Fan, C. Demaille, In *Scanning Electrochemical Microscopy*; Bard, A.J., Mirkin, M.V., Eds.; Marcel Dekker: New York, **2001**; p. 75.

27. Y. Shao, M. V. Mirkin, G. Fish, S. Kokotov, D. Palanker, A. Lewis, *Anal. Chem.***1997**, *69*, 1627.

28. B. B. Katemann, W. Schuhmann, *Electroanalysis* **2002**, *14*, 22.

29. P. Sun, M. V. Mirkin, *Anal. Chem.* **2006**, *78*, 6526.

30. C. J. Slevin, N. J. Gray, J. V. Macpherson, M. A. Webb, P. R. Unwin, *Electrochem. Commun.* **1999**, *1*, 282.

31. C. Kranz, G. Friedbacher, B. Mizaikoff, A. Lugstein, J. Smoliner, E. Bertagnolli, *Anal. Chem.* **2001**, *732*, 2491.

32. M. V. Mirkin, F.-R. F. Fan, A. J. Bard, *J. Electroanal. Chem.* **1992**, *328*, 47.

33. H.-Y. Liu, F.-R. F.Fan, C. W.Lin, A. J. Bard, *J. Am. Chem. Soc.* **1986**, *108*, 3838.

34. A. A. Gewirth, D. H. Craston, A. J. Bard, *J. Electroanal. Chem.* **1989**, *261*, 477.

35. (a) L.A. Nagahara, T. Tundat, S. M. Lindsay, *Rev. Sci. Instrum.* **1989**, *60*, 3128. (b) J. Wiechers, T. Twoney, D. M. Kolb, R. J. Behm, *J. Electroanal. Chem.* **1988**, *248*, 451.

36. C. M. Vitus, S. C. Chang, M. J. Weaver, *J. Phys. Chem.* **1991**, *95*, 7559.

37. B. Zhang, E. Wang, *Electrochim. Acta* **1994**, *39*, 103.

38. G. Zhao, D. M. Giolanda, J. R. Kirchoff, *Anal. Chem.* **1995,** *67*, 2592.

39. R. M. Penner, M.J. Heben, N. S. Lewis, *Anal. Chem.* **1989**, *61*, 1630.

40. P. Sun, Z. Zhang, J. Guo, Y. Shao, *Anal. Chem.* **2001**, *73*, 5346.

41. K. Potje-Kamloth, J. Janata, M. Jossowitz, *Ber. Bunsen-Ges. Phys. Chem.* **1990**, *93*, 1480.

42. (a) C. J. Slevin, N. J. Gray, J. V. Macpherson, M. A. Webb, P. R. Unwin, *Electrochem. Commun.* **1999**, *1*, 282. (b) C. E. Bach, R. J. Nichols, W. Beckmann, H. Meyer, *J. Electrochem. Soc.* **1993**, *40*, 1281. (c) Y. Zu, Z. Ding, J. Zhou, Y. Lee, A. J. Bard, *Anal. Chem.* **2001**, *73*, 2153.

43. A. J. Bard, M. V. Mirkin, (Eds.) *Scanning Electrochemical Microscopy;* Marcel Dekker: New York, **2001**.

44. (a) M. V. Mirkin, A. J. Bard, *J. Electroanal. Chem.* **1992**, *323*, 29. (b) A. J. Bard, M. V. Mirkin, P. R. Unwin, D. O. Wipf, *J. Phys. Chem.* **1992**, 96, 1861.

45. J. Kwak, A. J. Bard, *Anal. Chem.* **1989**, *61*, 1221.

46. M. V. Mirkin, F.-R. F. Fan, A. J. Bard, *J. Electroanal. Chem.* **1992**, *328*, 47.

47. Y. Shao, M. V. Mirkin, *J. Phys. Chem. B* **1998**, *102*, 9915. (b) J. L. Amphlett, G. Denuault, *J. Phys. Chem. B* **1998**, *102*, 9946.

48. (a) F. -R. F. Fan, A. J. Bard, *Science* **1995,** *267,* 871. (b) F. -R. F. Fan, J. Kwak, A. J. Bard, *J. Am. Chem. Soc.* **1996**, *118*, 9669.

49. A. J. Bard, G. Denuault, R. A. Friesner, B. C. Dornblaser, L. S. Tuckerman, *Anal.Chem.* **1991**, *63*, 1282.

50. C. Wei, A. J. Bard, M. V. Mirkin, *J. Phys. Chem.* **1995,** *99*, 16033. (b) M. Tsionsky, A. J. Bard, M. V. Mirkin, *J. Phys. Chem.* **1996**, *100*, 17881.

51. M. Tsionsky, A. J. Bard, M. V. Mirkin, *J. Am. Chem. Soc.* **1997**, *119*, 10785.

52. B. Liu, A. J. Bard, M. V. Mirkin, S. E. Creager, *J. Am. Chem. Soc.* **2004**, *126*, 1485.

53. (a) B. Liu, S. A. Rotenberg, M. V. Mirkin, *Proc. Natl. Acad. Sci. U.S.A.* **2000**, *97*, 9855. (b) B. Liu, S. A. Rotenberg, M. V. Mirkin, *Anal. Chem.* **2002**, *74*, 6340. (c) C. Cai, B. Liu, M. V. Mirkin, H. A. Frank, J. F. Rusling, *Anal. Chem.* **2002**, *74*, 114.

54. Y. Shao, H. H. Girault, *J. Electroanal. Chem. B* **1992**, *334*, 203.

55. A. A. Stewart, G. Taylor, H. H. Girault, J. McAleer, *J. Electroanal. Chem.* **1990**, *296*, 491.

56. P. D. Beattie, A. Delay, H. H. Girault, *J. Electroanal. Chem.* **1995**, *380*, 167.

57. T. Solomon, A. J. Bard, *Anal. Chem.* **1995**, *67*, 2787.

58. Y. Shao, M. V. Mirkin, *Anal. Chem.* **1998**, *70*, 3155.

59. Y. Shao, M. V. Mirkin, *J. Am. Chem. Soc.* **1997**, *119*, 8103.

60. C. Lee, J. Kwak, A. J. Bard, *Proc. Natl. Acad. Sci. U.S.A.* **1990**, *87***,** 1740.

61. R. K Zhu, S. M. Macfie, Z. F. Ding, *J. Exp. Bot.* **2005**, *56***,** 2831.

62. K. B. Holt, A. J. Bard, *Biochemistry* **2005**, *44*, 13214.

63. T. Yasukawa, T. Kaya, T. Matsue, *Electroanalysis* **2000**, *12*, 653.

64. Y.-S. Torisawa, T. Kaya, Y. Takii, D. Oyamatsu, M. Nishizawa, T. Matsue, *Anal. Chem.* **2003**, *75*, 2154.

65. H. Shiku, T. Shiraishi, H. Ohya, T. Matsue, H. Abe, H. Hoshi, M. Kobayashi, *Anal. Chem.* **2001**, *73*, 3751.

66. Y. Takii, K. Takoh, M. Nishizawa, T. Matsue, *Electrochim. Acta* **2003**, *48*, 3381.

67. W. Feng, S. A. Rotenberg, M. V. Mirkin, *Anal. Chem.* **2003**, *75*, 4148.

68. C. Cai, B. Liu, M. V. Mirkin, H. A. Frank, J. F. Rusling, *Anal. Chem.* **2002**, *74***,** 114.

69. F. Longobardi, P. Cosma, F. Milano, A. Agostiano, J. Mauzeroll, A. J. Bard, *Anal. Chem.* **2006***, 78*, 5046.

70. P. Sun, C. Cai, M. V. Mirkin, manuscript in preparation.

71. B. Liu, W. Cheng, S. A. Rotenberg, M. V. Mirkin, *J. Electroanal. Chem.* **2001**, *500*, 590.

72. J. M. Liebetrau, H. M. Miller, J. E. Baur, S. A. Takacs, V. Anupunpisit, P. A. Garris, D. O. Wipf, ***Anal. Chem.*** **2003**, *75*, 563.

73. D. O. Wipf, A. J. Bard, D. E. Tallman, *Anal. Chem.* **1993**, *65*, 1373.

74. D. O. Wipf, A. J. Bard, *Anal. Chem.* **1992**, *64*, 1362.

75. A. Hengstenberg, C. Kranz, W. Schuhmann, *Chem. Eur. J.* **2000**, *6*, 1547.

76. (a) B. B. Katemann, A. Schulte, W. Schuhmann, *Chem. Eur. J.* **2003**, *9*, 2025. (b) B. B. Katemann, A. Schulte, W. Schuhmann, *Electroanalysis* **2004**, *16***,** 60.

77. P. I. James, L. F. Garfias-Mesias, P. J. Moyer, W. H. Smyrl, *J. Electrochem. Soc.* **1998**, *145*, L64.

78. Y. Lee, Z. F. Ding, A. J. Bard, *Anal. Chem.* **2002**, *74*, 3634.

79. A. Hengstenberg, A. Blöchl, I. D. Dietzel, W. Schuhmann, *Angew. Chem., Int. Ed. Engl.* **2001**, *40*, 905.

80. B. R. Horrocks, D. Schmidtke, A. Heller, A. J. Bard, *Anal. Chem.* **1993**, *65*, 3605.

81. M. A. Alpuche-Aviles, D. O. Wipf, *Anal. Chem.* **2001**, *73***,** 4873.

82. C. Gabrielli, F. Huet, M. Keddam, P. Rousseau, V. Vivier, *J. Phys. Chem. B* **2004**, *108***,** 11620.

83. R. T. Kurulugama, D. O. Wipf, S. A. Takacs, S. Pongmayteegul, P. A. Garris, J. E. Baur, *Anal. Chem.* **2005**, *77*, 1111.

84. M. Tsionsky, J. Zhou, S. Amemiya, F. -R. F. Fan, A. J. Bard, R. A. W. Dryfe, *Anal. Chem.* **1999**, *71*, 4300.

85. S. Amemiya, and A. J. Bard, *Anal. Chem.* **2000**, *72*, 4940.

86. J. P. Wilburn, D. W. Wright, D. E. Cliffel, *Analyst* **2006**, *131*, 311.

87. J. Mauzeroll, A. J. Bard, *Proc. Natl. Acad. Sci. U.S.A*. **2004**, *101*, 7862.

88. J. Mauzeroll, A. J. Bard, O. Owhadian, T. J. Monks, *Proc. Natl. Acad. Sci. U.S.A*. **2004**, *101***,** 17582.

89. J. Guo, S. Amemiya, *Anal. Chem.* **2005**, *77*, 2147.

90. W. Zhan, A. J. Bard, *Anal. Chem.* **2006**, *78*, 726.

Chapter II References and Notes

1. R. D. Rogers, K. R. Seddon, *Science* **2003**, *302*, 792.
2. *Ionic Liquids in Synthesis*; P. Wasserscheid, T. Welton, Eds.; Wiley-VCH: Weinheim, Germany, 2003.
3. *Green Industrial Applications of Ionic Liquids*; R. D. Rogers, K. R. Seddon, S. Volkov, Eds.; NATO Sciences Series, Vol 92. Kluwer: Dordrecht, The Netherlands, 2002.
4. K. Nakashima, F. Kubota, T. Maruyama, M. Goto, *Ind. Eng. Chem. Res.* **2005**; *44*, 4368 and references cited therein.
5. (a) N. Papageorgiou, Y. Athanassov, M. Armand, P. Bonhote, H. Pettersson, A. Azam, M. Gratzel, *J. Electrochem. Soc.* 1**996**, *143*, 3099. (b) P. Wang, S. M. Zakeeruddin, J. –E. Moser, M. Gratzel, *J. Phys. Chem. B.* **2003**, *107*, 13280. (c) P. Wang, B. Wenger, R. Humphry-Baker, J. –E. Moser, J. Teuscher, W. Kantlehner, J. Mezger, E. V. Stoyanov, S. M. Zakeeruddin, M. Gratzel, *J. Am. Chem. Soc.* **2005**, *127*, 6850.
6. F. O. Laforge, T. Kakiuchi, F. Shigematsu, M. V. Mirkin, *J. Am. Chem. Soc.* **2004**, *126*, 15380.
7. For recent reviews of electrochemistry at the ITIES see (a) H. H. Girault, in *Modern Aspects of Electrochemistry*, Vol. 25 (J. O'M. Bockris, B. E. Conway, R. E. White, Eds.), Plenum Press, New York, 1993, p. 1. (b) P. Vanýsek, *TRAC-Trends Anal. Chem.* **1993**, *12,* 357. (c) Z. Samec, T. Kakiuchi, in *Advances in Electrochemical Science and Electrochemical Engineering,* Vol. 4 (H. Gerischer, C. W. Tobias, Eds.), VCH, New York, 1995, p. 297. (d) B. Liu, M. V. Mirkin, *Anal. Chem.* **2001**, *73*, 670A. (e) *Liquid Interfaces in Chemical, Biological, and Pharmaceutical Applications* (A. G. Volkov, Ed.), Marcel Dekker, N.Y., 2001.

8. (a) A. L. Barker, M. Gonsalves, J. V. Macpherson, C. J. Slevin, P. R. Unwin, *Anal. Chim. Acta* **1999**, *385*, 223 (b) M. V. Mirkin, M. Tsionsky, in *Scanning Electrochemical Microscopy* (A. J. Bard, M. V. Mirkin, Eds.), Marcel Dekker, New York, 2001, p. 299.

9. A. L. Barker, J. V. Macpherson, C. J. Slevin, P. R. Unwin, *J. Phys. Chem. B* **1998**, *102*, 1586.

10. (a) C. Wei, A. J. Bard, M. V. Mirkin, *J. Phys. Chem.* **1995**, *99*, 16033. (b) M. Tsionsky, A. J. Bard, M. V. Mirkin, *J. Phys. Chem.* **1996**, *100*, 17881.

11. T. Kakiuchi, N. Tsujioka, S. Kurita, Y. Iwami, *Electrochem. Commun.* **2003**, *5*, 159.

12. A. J. Bard, L. R. Faulkner, *Electrochemical Methods: Fundamentals and Applications*; 2nd ed.; Wiley & Sons: New York, 2001.

13. K. Nakatani, T. Uchida, H. Misawa, N. Kitamura, H. Masuhara, *J. Electroanal. Chem.* **1994**, *367*, 109.

14. (a) E. S. Yang, M.-S. Chan, A. C. Wahl, *J. Phys. Chem.* **1980**, *84,* 3094. (b) A. Zahl, R. van Eldik, T. W. Swaddle, *Inorg. Chem.* **2002**, *41*, 757.

15. P. R. Unwin, A. J. Bard, *J. Phys. Chem.* **1991**, *95*, 7814.

16. J. Kwak, A. J. Bard, *Anal. Chem.* **1989**, *61*, 1221.

17. R. A. Marcus, *J. Phys. Chem.* **1990**, *94*, 4155.

Chapter III References and Notes

1. W. D. Stein, W. R. Lieb, *Transport and Diffusion across Cell Membranes,* Academic Press, Orlando, 1986.
2. M. A. Wilson, A. Pohorille, *J. Am. Chem. Soc.* **1996**, *118***,** 6580.
3. E. Gouaux, R. MacKinnon, *Science* **2005**, *310*, 1461.
4. P. Vanýsek, *TRAC-Trends in Anal. Chem.* **1993,** *12,* 357.
5. A. Berduque, A. Sherburn, M. Ghita, R. A. W. Dryfe, D. W. M. Arrigan, *Anal. Chem.* **2005**, *77*, 7310.
6. (a) H. H. Girault, D. J. Schiffrin, in *Electroanalytical Chemistry*, Vol. 15 (A. J. Bard, Ed.), Marcel Dekker, New York, 1989, p. 1. (2) H. H. Girault, in *Modern Aspects of Electrochemistry*, Vol. 25 (J. O'M. Bockris, B. E. Conway, R. E. White, Eds.), Plenum Press, New York, 1993, chap. 1.
7. Z. Samec, T. Kakiuchi, in *Advances in Electrochemical Science and Electrochemical Engineering,* Vol. 4 (H. Gerischer, C. W. Tobias, Eds.), VCH, New York, 1995, p. 297.
8. I. Benjamin, *Science* **1993**, *261*,1558.
9. (a) W. Schmickler, *J. Electroanal. Chem.* **1997**, *426,* 5. (b) S. Frank, W. Schmickler, *J. Electroanal. Chem.* **2006**, *590*, 138.
10. R. A. Marcus, *J. Chem. Phys.* **2000**, *113*, 1618.
11. T. Shioya, S. Nishizawa, N. Teramae, *J. Am. Chem. Soc.* **1998**, *120*, 11534.
12. T. Kakiuchi, *J. Electroanal. Chem.* **1992**, *322*, 55.
13. K. Kontturi, J. A. Manzanares, L. Murtomaki, D. J. Schiffrin, *J. Phys. Chem. B* **1997**, *101*, 10801.

14. P. Sun, F. O. Laforge, M. V. Mirkin, *J. Am. Chem. Soc.* **2005**, *127*, 8596.

15. (a) Y. Shao, H. H. Girault, *J. Electroanal. Chem.* **1992**, *334*, 203. (b) M. C. Osborne, Y. Shao, C. M. Pereira, H. H. Girault, *J. Electroanal. Chem.* **1994**, *364*, 155. (c) C. Quinn, R. Lahtinen, L. Murtomaki, *J. Electroanal. Chem.*, **1999**, *460*, 149. (d) S. Wilke, *J. Electroanal. Chem.* **2001**, *504*, 184. (e) F. Li, Y. Chen, M. Zhang, P. Jing, Z. Gao, Y. Shao, *J. Electroanal. Chem.* **2005**, *579*, 89.

16. (a) Y. Shao, M. V. Mirkin, *J. Am. Chem. Soc.* **1997**, *119*, 8103. (b) C. Cai, Y. Tong, M. V. Mirkin, *J. Phys. Chem. B* **2004**, *108*, 17872.

17. (a) Y. Shao, B. Liu, M. V. Mirkin, *J. Am. Chem. Soc.* **1998**, *120*, 12700. (b) B. Liu, Y. Shao, M. V. Mirkin, *Anal. Chem.* **2000**, *72*, 510.

18. Y. Chen, Z. Gao, F. Li, L. Ge, M. Zhang, D. Zhan, Y. Shao, *Anal. Chem.* **2003**, *75*, 6593.

19. Y. Shao, H. H. Girault, *J. Electroanal. Chem.* **1990**, *282,* 59.

20. M. H. M. Caçote, C. M. Pereira, L. Tomaszewski, H. H. Girault, F. Silva, *Electrochim. Acta* **2004**, *49***,** 263.

21. P. D. Beattie, A. Delay, H. H. Girault, *J. Electroanal. Chem.* **1995**, *380*, 167.

22. (a) D. J. Henderson, W. Schmickler, *J. Chem. Soc. Faraday Trans.* **1996**, *92*, 3839. (b) I. Benjamin, *Annu. Rev. Phys. Chem.* **1997**, *48*,407.

23. L. I. Daikhin, M. Urbakh, *J. Electroanal. Chem.* **2003**, *560*, 59.

24. H. Wang, E. Borguet, K. B. Eisenthal, *J. Phys. Chem. B* **1998**, *102*, 4927.

25. G. Luo, S. Malkova, J. Yoon, D. G. Schultz, B. Lin, M. Meron, I. Benjamin, P. Vanýsek, M. L. Schlossman, *Science* **2006**, *311*, 216.

26. A. Sabela, V. Mareček, Z. Samec, R. Fuoco, *Electrochim. Acta* **1992**, *37*, 231.

27. A. A. Kornyshev, A. M. Kuznetsov, M. Urbakh, *J. Chem. Phys.* **2002**, *117*, 6766.

28. D. J. Fermin, Z. Ding, H. D. Duong, P.-F. Brevet, H. H. Girault, *J. Phys. Chem.* B **1998**, *102*, 10334.

Chapter IV References and Notes

1. (a) H. H. Girault, in Modern Aspects of Electrochemistry, Vol. 25 (J. O'M. Bockris, B. E. Conway, R. E. White, Eds.), Plenum Press, New York, 1993, chap. 1. (b) Z. Samec, T. Kakiuchi, in Advances in Electrochemical Science and Electrochemical Engineering, Vol. 4 (H. Gerischer, C. W. Tobias, Eds.), VCH, New York, 1995, p. 297.
2. R. B. Gennis, Biomembranes; Springer-Verlag: New York, 1989.
3. Y. Shao, J. A. Campbell, H. H. Girault, *J. Electroanal. Chem.* **1991**, *300*, 15.
4. F. Reymond, H. H. Girault, P.-A. Carrupt, G. Steyaert, B. Testa, *J. Am. Chem. Soc.* **1996**, *118*, 11951.
5. P. Sun, Z. Zhang, Z. Gao, Y. Shao, *Angew. Chem. Int. Ed.* **2002**, *41*, 3445.
6. G. Luo, S. Malkova, J. Yoon, D. G. Schultz, B. Lin, M. Meron, I. Benjamin, P. Vanýsek, M. L. Schlossman, *Science* **2006**, *311*, 216.
7. (a) Y. Shao, M. V. Mirkin, *J. Am. Chem. Soc.* **1997**, *119*, 8103. (b) C. Cai, Y. Tong, M. V. Mirkin, *J. Phys. Chem.* B **2004**, *108*, 17872.
8. T. Kakiuchi, *J. Electroanal. Chem.* **1992**, *322*, 55.
9. R. A. Marcus, *J. Chem. Phys.* **2000**, *113*, 1618.
10. K. Kontturi, J. A. Manzanares, L. Murtomaki, D. J. Schiffrin, *J. Phys. Chem.* **1997**, *101*, 10801.
11. I. Benjamin, *Science* **1993**, *261*, 1558.
12. B. Schnell, R. Schurhammer, G. Wipff, *J. Phys. Chem. B* **2004**, *108*, 2285.
13. M. A. Wilson, A. Pohorille, *J. Am. Chem. Soc.* **1996**, *118*, 6580.
14. H. L. Tepper, G. A. Voth, *J. Phys. Chem. B* **2006**, *110*, 21327.
15. S. Amemiya, A. J. Bard, *Anal. Chem.* **2000**, *72*, 4940.
16. (a) P. Sun, F. O. Laforge, M. V. Mirkin, *J. Am. Chem. Soc.* **2005**, *127*, 8596. (b) F. O. Laforge, P. Sun, M. V. Mirkin, *J. Am. Chem. Soc.* **2006**, **128**, 15019.

17. "Neat" DCE was obtained by distilling HPLC grade DCE (Sigma-Aldrich) three times. The nanopipette preparation was described previously. [16] Briefly, a Model P-2000 laser puller (Sutter Instrument Co.) was used to prepare the pipettes from quartz capillaries. The aqueous solution was filled from the back using a 10-μL syringe, and then a 0.125-mm-radius Ag/AgCl wire was inserted in the pipette. A 0.25-mm-radius Ag wire was used as a quasi reference electrode in DCE. Voltammograms were obtained with a BAS-100B potentiostat. To prepare water-saturated DCE, a portion of thrice distillated DCE was equilibrated with an equal amount of pure water in a closed Erlenmeyer flask for 48h, while the flask was shaken periodically. Water-saturated DCE was diluted by neat DCE to obtain the desired concentration of water. Conductivity measurements were made using a home-built trans-impedance amplifier and a SR-850 lock-in amplifier. For experimental details and data analysis see ref. 16b.

18. W. L. Masterton, M. C. Gendrano, *J. Phys. Chem.* **1966**, *70*, 2895.

19. A significant hysteresis and a current peak after the potential sweep reversal were often observed when the applied voltage exceeded ~1 V (e.g., blue curve in Fig. 4.1A). Videomicroscopic observations showed that these distortions are caused by the motion of DCE in and out of the pipette and not related to IT (see ref. 20 for details). For better clarity, only forward portions of some voltammograms are shown in Figs. 4.1 and 4.3.

20. F. O. Laforge, J. Carpino, S. A Rotenberg, M. V. Mirkin, *Proc. Nat. Acad. Sci. U.S.A.* **2007**, *104*, 11895.

21. (a) G. Moakes, L. T. Gelbaum , J. Leisen, J. Janata, V. Marecek *J. Electroanal. Chem.* **2006**, *593*, 111. (b) G. Moakes, L. L. Daemen, L. T. Gelbaum, J. Leisen, V. Marecek J. Janata, *J. Phys. Chem. B* **2007**, *111*, 7312.

Chapter V References

1 H. Matsuoka, T. Komazaki, Y. Mukai, M. Shibusawa, H. Akane, A. Chaki, N. Uetake, M. Saito, *J. Biotech.* **2005**, *116*, 185 and references cited therein.

2 P. L. Felgner, T. R. Gadek, M. Holm, R. Roman, H. W. Chan, M. Wenz, J. P. Northrop, G. M. Ringold, M. Danielsen, *Proc. Natl. Acad. Sci. USA* **1987**, *84*, 7413.

3 E. Neuman, A. E. Sowers, C. A. Jordan (eds) (1989) *Electroporation and Electrofusion in Cell Biology* (Plenum Press, New York).

4 M. Knoblauch, A. J. E. van Bel, *Plant Cell.* **1998**, *10*, 35.

5 I. Laffafian, M. B. Hallett, *Biophys. J.* **1998**, *75*, 2558.

6 M. Knoblauch, J. Hibberd, J. C. Gray, A. J. E. van Bel, *Nature Biotech.* **1999**, *17*, 906.

7 C. K. Byun, X. Wang, Q. Pu, S. Liu, *Anal. Chem.* **2007**, *79*, 3862.

8 X. Chen, A. Kis, A. Zettl, C. R. Bertozzi, *Proc. Natl. Acad. Sci. USA* **2007**, *104*, 8218.

9 K. T. Rodolfa, A. Bruckbauer, D. Zhou, A. I. Schevchuk, Y. E. Korchev, D. Klenerman, *Nano Lett.* **2006**, *6*, 252.

10 H. H. Girault, D. J. Schiffrin, (1989) in *Electroanalytical Chemistry*, ed A. J. Bard (Marcel Dekker, New York), Vol. 15, pp. 1-141.

11 Y. Shao, M. V. Mirkin, *J. Am. Chem. Soc.* **1997**, *119*, 8103.

12 C. Wei, A. J. Bard, S. Feldberg, *Anal. Chem.* **1997**, *69*, 4627.

13 A. J. Bard, M. V. Mirkin, eds (2001) *Scanning Electrochemical Microscopy*. (Marcel Dekker, New York).

14 B. Liu, S. A. Rotenberg, M. V. Mirkin, *Proc. Natl. Acad. Sci. USA* **2000**, *97*, 9855.

15 B. Gabriel, J. Teissié, *Bioelectrochem. Bioenerg.* **1998**, *47*, 113.

16 J. M. Cunliffe, R. K. Sunahara, R. T. Kennedy, *Anal. Chem.* 2006, *78*, 1731.

17 Y. E. Korchev, C. L. Bashford, M. Milovanovic, I. Vodyanoy, M. J. Lab *Biophys. J.* **1997**, *73*, 653.

18 Y. Shao, M. V. Mirkin, *J. Phys. Chem. B.* **1998**, *102*, 9915.

19 F. Mugele, J. C. Baret, *J. Phys.: Condens. Matter* **2005**, *17*, 705.

20 G. Wang, B. Zhang, J. R. Wayment, J. M. Harris, H. S. White, *J. Am. Chem. Soc.* **2006**, *128*, 7679.

21 E. Gouaux, R. MacKinnon, *Science* **2005**, *310*, 1461.

22 M. Lavallée, G. Szabo, (1969) in *Glass Microelectrodes*, eds M. Lavallée, O. F. Schanne, N. C. Hébert (Wiley, New York) Chapter 6.

23 H. J. Keh, H. C. Ma, *Langmuir* **2007**, *23*, 2879.

24 D. S. Reichmuth, T. J. Shepodd, B. Kirby, *Anal. Chem.* **2004**, *76*, 5063.

25 A. Bruckbauer, D. Zhou, L. Ying, Y. E. Korchev, C. Abell, D. Klenerman, *J. Am. Chem. Soc.* **2003**, *125*, 9834.

26 S. Neugebauer, S. R. Evans, Z. P. Aguilar, M. Mosbach, I. Fritsch, W. Schuhmann, *Anal. Chem.* **2004**, *76*, 458.

Chapter VI References

1. T. Finkel, *Curr. Opin. Cell. Biol.* **2003**, *15*, 247.
2. N. Houstis, E. D. Rosen, E. S. Lander, *Nature* **2006**, *440*, 944.
3. V. Adler, Z. Yin, K. D. Tew, Z. Ronai, *Oncogene* **1999**, *18*, 6104.
4. R. M. Wightman, *Science* **2006**, *311*, 1570.
5. C. Amatore, S. Arbault, D. Bruce, P. de Oliveira, M. Erard, M. Vuillaume, *Faraday Discuss.* **2000**, *116*, 319.
6. B. R. Horrocks, G. Wittstock, (2001) in *Scanning Electrochemical Microscopy*, eds A. J. Bard, M. V. Mirkin, (Marcel Dekker, New York), pp 445-519.
7. A. J. Bard, X. Li, W. Zhan, *Biosens. Bioelectron.* **2006**, *22*, 461.
8. S. Amemiya, J. Guo, H. Xiong, D. A. Gross, *Anal. Bioanal. Chem.* **2006**, *386*, 458.
9. A. Devadoss, J. D. Burgess, *J. Am. Chem. Soc.* **2004**, *126*, 10214.
10. J. Mauzeroll, A. J. Bard, *Proc. Natl. Acad. Sci. USA* **2004**, *101*, 7862.
11. J. Mauzeroll, A. J. Bard, O. Owhadian, T. J. Monks, *Proc. Natl. Acad. Sci. USA* **2004**, *101*, 17582.
12. C. Amatore, S. Arbault, C. Bouton, K. Coffi, J.-C. Drapier, H. Ghandour, Y. Tong, *ChemBioChem* **2006**, *7*, 653.
13. H. Lu, M. Gratzl, *Anal. Chem.* **1999**, *71*, 2821.
14. R. T. Kurulugama, D. O. Wipf, S. A. Takacs, S. Pongmayteegul, P. A. Garris, J. E. Baur, *Anal. Chem.* **2005**, *77*, 1111.
15. T. Yasukawa, T. Kaya, T. Matsue, *Electroanalysis* **2000**, *12*, 653.

16. G. Wittstock, M. Burchardt, S. E. Pust, Y. Shen, C. Zhao, *Angew. Chem. Int. Ed.* **2007**, *46*, 1584.

17. B. Liu, S. A. Rotenberg, M. V. Mirkin, *Proc. Natl. Acad. Sci. USA* **2000**, *97*, 9855.

18. B. Liu, S. A. Rotenberg, M. V. Mirkin, *Anal. Chem.* **2002**, *74*, 6340.

19. A.-S. Cans, N. Wittenberg, R. Karlsson, L. Sombers, M. Karlsson, O. Orwar, A. G. Ewing, *Proc. Natl. Acad. Sci. USA* **2003**, *100*, 400.

20. W. Zhan, A. J. Bard, *Anal. Chem.* **2006**, *78*, 726.

21. A. G. Ewing, T. G. Strein, Y. Y. Lau, *Acc. Chem. Res.* **1992**, *25*, 440.

22. S. Arbault, P. Pantano, J. A. Jankowski, M. Vuillaume, C. Amatore, *Anal. Chem.* **1995**, *67*, 3382.

23. R. J. Fasching, S.-J. Bai, T. Fabian, F. B. Prinz, *Microelectron. Eng.* **2006**, *83***,** 1638.

24. J. J. Watkins, J. Chen, H. S. White, H. D. Abruña, E. Maisonhaute, C. Amatore, *Anal. Chem.* **2003**, *75*, 3962.

25. M. L. Kraft, P. K. Weber, M. L. Longo, I. D. Hutcheon, S. G. Boxer, *Science* **2006**, *313*, 1948.

26. Y. E. Korchev, C. L. Bashford, M. Milovanovic, I. Vodyanoy, M. J. Lab, *Biophys. J.* **1997**, *73*, 653.

27. E. Betzig, G. H. Patterson, R. Sougrat, O. W. Lindwasser, S. Olenych, J. S. Bonifacino, M. W. Davidson, J. Lippincott-Schwartz, H. F. Hess, *Science* **2006**, *313*, 1642.

28. J. Kwak, A. J. Bard, *Anal. Chem.* **1989**, *61*, 1221.

29. R. Swaminathan, C. P. Hoang, A. S. Verkman, *Biophys. J.* **1997**, *72*, 1900.

30. W. F. Wonderlin, K. A. Woodfork, J. S. Strobl, *J. Cell. Physiol.* **1995**, *165*, 177.

31. A. J. Bard, M. V. Mirkin, eds (2001) *Scanning Electrochemical Microscopy*. (Marcel Dekker, New York).

32. H. Miedema, S. M. Assmann, *J. Membr. Biol.* **1998**, *166*, 101.

33. W.-R. Schlue, W. Kilb, D. Gunzel, *Electrochim. Acta* **1997**, *42*, 3197.

34. A. S. Klymchenko, H. Stoeckel, K. Takeda, Y. Mély, *J. Phys. Chem. B* **2006**, *110*, 13624.

35. S. Amemiya, A. J. Bard, *Anal. Chem.* **2000**, *7*, 4940.

36. J. Wegener, C. R. Keese, I. Giaever, *Exp. Cell. Res.* **2000**, *259*, 158.

37. F. –R. F. Fan, A. J. Bard, *Proc. Natl. Acad. Sci. USA* **1999**, *96*, 14222.

38. L. P. Bauermann, W. Schuhmann, A. Schulte, *Phys. Chem. Chem. Phys.* **2004**, *6*, 4003.

39. W. J. Feng, S. A. Rotenberg, M. V. Mirkin, *Anal. Chem.* **2003**, *75*, 4148.

40. P. Sun, M. V. Mirkin, *Anal. Chem.* **2006**, *78*, 6526.